Electron Quantum Interference and Transport

In Ultrasmall Metal Structures

A Dissertation

Presented to the Faculty of the Graduate School

of

Yale University

in Candidacy for the Degree of

Doctor of Philosophy

by

Samuel Jonas Wind

December 1987

ABSTRACT

Electron Quantum Interference and Transport in Ultrasmall Metal Structures

Samuel Jonas Wind
Yale University
1987

Advances in microfabrication technology have made possible the production of structures with ever decreasing dimensions. As the size of these structures approaches certain characteristic lengths, quantum mechanical effects become evident. Electron interference phenomena may be observed in systems whose size is on the order of the electron phase coherence length, ℓ_ϕ. ℓ_ϕ can be 1 μm or more at 1 K. For a wire of width less than ℓ_ϕ, the constructive interference of electron partial waves which are elastically scattered by impurities leads to one-dimensional localization. This effect manifests itself in the form of a small correction to the low temperature residual resistance, as first predicted by D. J. Thouless in 1977. For a ring structure of diameter ~ ℓ_ϕ, electron quantum interference leads to oscillations in the magnetoresistance of the ring with periods h/e and h/2e. These oscillations are the solid state analog of the Aharonov-Bohm effect in vacuum. Narrow wires and rings of Al and Ag have been fabricated using x-ray and electron-beam lithography, with linewidths as narrow as 350 Å. Magnetoresistance measurements on the rings reveal oscillations with fundamental periods h/e and h/2e. Measurements on the wires show one-dimensional localization effects with spin-orbit scattering and one-dimensional superconducting fluctuations. These effects are used to probe electron energy and phase relaxation mechanisms in narrow wires. It is found that at low temperatures, the primary mechanisms are electron-phonon scattering and electron-electron scattering. As the wire width becomes less than the electron

thermal diffusion length, $\ell_T \sim 1000$ Å, a new type of electron-electron scattering mechanism becomes evident: one-dimensional scattering with small energy transfers. For such narrow wires, this is the dominant mode of electron phase relaxation at low temperatures.

Acknowledgements

"Who is wise? He who learns from all other men." - Ethics of the Fathers

During my years at Yale, I have had the privilege of interacting with many individuals who have contributed directly and indirectly both to the work I have pursued and to the enhancement of the environment in which I have worked. It is with deep gratitude that I acknowledge the help and encouragement of those persons.

I am especially grateful to Professor Daniel Prober. As my thesis advisor, his guidance and support were essential in helping me face the challenges of a complex and difficult undertaking. His concern for my professional and career development were instrumental in training me for life after graduate school. His understanding of the demands of life outside the laboratory have enabled me to enjoy all aspects of my stay at Yale. He has also been a good friend.

Special thanks go to my colleagues Santhanam and Venkat Chandrasekhar, both of whom I have worked with closely on various aspects of the experiments reported in this thesis. Santhanam introduced me to the physics of localization and to my first low temperature experiments. He also performed much of the theoretical work which was used to interpret our data on narrow wires. Chandrasekhar built the temperature control circuit and wrote the control program for the low temperature experiments. He also participated in the measurement and analysis of the experiments on the narrower wires and allowed me to get involved in the Aharonov-Bohm experiments on rings just as the field began to heat up with excitement. I also wish to acknowledge the contribution of Michael Rooks in converting the

scanning electron microscope to an electron-beam writing machine, which allowed me to fabricate the narrowest wires in this work. He also performed the deep-UV exposures of the contact pads for those samples. In addition, Mike taught me all kinds of ways to use and abuse computers, and he planted in my heart the initial seeds of hatred for FORTRAN. Thanks go to Paul McEuen as well for continuing the work on the PMMA bilayer resist so that it could be used routinely and reliably. Dean Face set up and characterized the Reactive Ion Etching system, which was an important tool in fabricating samples. Dean, although not directly involved in the field of quantum transport, was always eager to discuss the various puzzles we encountered in trying to understand how electrons navigate through solids. His expertise in WordPerfect also helped me in the writing of the manuscript for this thesis.

Mr. Clifford Sneider provided enormous help in the construction and repair of all kinds of laboratory apparatus. Dr. Alan Pooley first taught me the science and art of scanning electron microscopy, without which much of the work in this thesis would have been impossible. Dr. Philippe Male took SEM pictures of the smallest samples in this work. Ms. June Yarosh was helpful in "all things secretarial," from large to small. Ms. Sara Batter helped me deal with administrative issues of the Physics Department and the Graduate School. Dr. Stanley Mroczkowski gave me guidance and encouragement and was always willing to discuss issues of all kinds, ranging from the future of superconducting technology to Guillermo Vilas' topspin backhand. Ms. Jayne Miller and Ms. Linda Schwartz served as advisors on a wide variety of pseudoscientific topics. They also provided an island of normal life on the fourth floor of Becton Center.

Professor Robert Wheeler, while not my thesis advisor, always expressed a keen interest in my work and pointed out certain subtle questions for me to ponder. Professor Yosef Imry of the Weizmann Institute also made his theoretical insights available whenever they were needed. In addition, I thank Professors D. E. Prober, R. G. Wheeler, A. D. Stone, R. Shankar and D. Meschede for serving on my thesis committee, as well as Dr. W. J. Skocpol for serving as the "outside reader" of my thesis.

I also wish to thank my parents and parents-in-law for their support and confidence throughout my graduate work. Their patience is well appreciated.

Financial support for this work was provided in part by National Science Foundation Grant Nos. DMR-8207443, DMR-8505539 and ECS-7927165. Support of the microlithographic facilities at Yale University was provided by National Science Foundation Grant No. DMR-8213080, IBM Corp. and Shipley, Inc.

Finally, I would like to dedicate this thesis to my wife, Elizabeth, whose love and confidence have served as a constant source of inspiration and encouragement.

Table of Contents

	Page
Acknowledgements	ii
List of Symbols and Abbreviations	ix
List of Figures	xiii
List of Tables	xvi
I. Introduction	
I.A. Quantum Interference Phenomena	1
I.B. Electron Scattering Mechanisms	5
I.C. The Aharonov-Bohm Effect in Metals	6
I.D. Microfabrication	7
I.E. Outline of this Thesis	8
II. Theory	
II.A. Quantum Interference Phenomena - Qualitative Features	10
II.A.1. Weak Localization	11
II.A.2. Aharonov-Bohm Oscillations in Rings	17
II.A.3. Spin-Orbit Scattering	17
II.A.4. Scattering by Magnetic Impurities	19
II.B. Length Scales and Dimensionality	19
II.C. Quantum Interference Phenomena - Quantitative Predictions	24
II.C.1. Weak Localization	24
II.C.1a. Spin-orbit scattering	31

II.C.1b. Magnetic scattering 32
II.C.2. Aharonov-Bohm Oscillations in Rings 33
II.C.3. Superconducting Fluctuations 35
II.C.3a. Aslamazov-Larkin fluctuations 35
II.C.3b. Maki-Thompson fluctuations 37
II.D. Electron Scattering Mechanisms 39
II.D.1. Electron-Electron Scattering 40
II.D.1a. Clean limit 40
II.D.1b. Dirty limit 42
II.D.2. Electron-Phonon Scattering 48
II.D.2a. Clean limit 49
II.D.2b. Dirty limit 51
II.D.3. Electron-Fluctuation Scattering 53
II.D.4. Two-Level Scattering 54

III. Fabrication of Ultrasmall Structures for Quantum Transport Studies
III.A. Preliminary Considerations 55
III.A.1. Materials 55
III.A.2. Fabrication Requirements 57
III.A.3. Available Fabrication Techniques 61
III.B. X-Ray Lithography 66
III.B.1. The X-Ray Source 69
III.B.2. Fabrication of X-Ray Masks 75
III.B.3. The X-Ray Resist 92
III.B.4. X-Ray Exposure and Development 95
III.B.5. Metallization and Liftoff 96

III.C. Electron-Beam Lithography 100

III.C.1. Deep Ultraviolet Exposure 102

III.C.2. Electron-Beam Exposure 102

IV. Measurement Technique

IV.A. Sample Preparation 108

IV.B. Low Temperature Apparatus 109

IV.C. Resistance Measurement 110

V. Experimental Results

V.A. Sample Properties 114

V.B. Magnetoresistance of Narrow Wires 121

V.C. Magnetoresistance of Rings 133

V.D. Electron Scattering Rates 137

V.D.1. The Phase Breaking Rate 137

V.D.2. The Spin-Orbit Scattering Rate 147

VI. Comparison to Other Work

VI.A. One-Dimensional Localization 149

VI.B. Electron Scattering Rates 154

VII. Summary and Conclusions

VII.A. Quantum Interference Phenomena 157

VII.B. Microlithography 160

VII.C. Reflections on Future Work 161

Appendix A. Preparation of X-Ray Masks 163

Appendix B. Estimate of the One-Dimensional Aslamazov-Larkin Contribution to the Resistance in a Magnetic Field 169

References 173

List of Symbols and Abbreviations

$\vec{A}$	Magnetic vector potential
A_1	Coefficient for linear term in Eq. (V-4)
$A_{2/3}$	Coefficient for $T^{2/3}$ term in Eq. (V-5)
A_3	Coefficient for T^3 term in Eqs. (V-4) and (V-5)
AL	Aslamazov-Larkin
B	Magnetic flux density
c	Speed of light
D	Electron thermal diffusivity
d	Sample width
DUV	Deep ultraviolet
E	Energy
E_c	Characteristic line radiation energy of x-ray photons
E_F	Fermi energy
E_i	Energy of incident electrons on x-ray target
e	Magnitude of electronic charge
H	Magnetic field strength
H_{c2}	Superconducting upper critical field
H_ϕ	Phase breaking field
H_2	Phase breaking field for the triplet term in Eq. (II-27)
h	Planck's constant
$\hbar$	$h/2\pi$
$\vec{k}$	Wavevector
k_B	Boltzmann constant
k_F	Fermi wavevector

L	Sample length
ℓ	Elastic mean free path
ℓ_H	Magnetic field length
ℓ_s	Magnetic scattering length
ℓ_{so}	Spin-orbit scattering length
ℓ_T	Electron thermal diffusion length
ℓ_ϕ	Phase coherence length
ℓ_1	Characteristic length for singlet term in localization magnetoresistance
ℓ_2	Characteristic length for triplet term in localization magnetoresistance
m^*	Electron effective mass
MT	Maki-Thompson
n(E)	Electron density of states
PMMA	Polymethylmethacrylate
$\vec{q}$	Wavevector
q_p	Characteristic phonon wavevector
R	Resistance
$R_\square$	Resistance per square (sheet resistance)
RIE	Reactive ion etching
SEM	Scanning electron microscope
STEM	Scanning transmission electron microscope
T	Temperature
T_c	Superconducting transition temperature
t	Time
V	Voltage
v_F	Fermi velocity
v_s	Velocity of sound

W	Sample width
α	Fine structure constant
$\alpha^2F(\omega)$	Eliashberg function
β	Larkin superconducting fluctuation strength parameter
γ	Phase factor for h/e oscillations in rings
ΔE	Change in electron energy
ΔR	Change in resistance at fixed temperature and magnetic field
δR	Magnetoresistance
λ	Wavelength
λ_p	Characteristic phonon wavelength
ξ	Superconducting coherence length
ρ	Resistivity
ρ_o	Residual resistivity
σ	Conductivity
τ	Elastic scattering time
τ_{coll}	Time between electron-electron collisions
τ_E^{-1}	Energy relaxation rate
τ_{ee}^{-1}	Electron-electron scattering rate
τ_{ef}^{-1}	Electron-fluctuation scattering rate
τ_{ep}^{-1}	Electron-phonon scattering rate
τ_N^{-1}	Electron-electron small energy transfer scattering rate
τ_s^{-1}	Magnetic scattering rate
τ_{so}^{-1}	spin-orbit scattering rate
τ_ϕ^{-1}	Electron phase breaking rate
Φ	Magnetic flux
Φ_o	Magnetic flux quantum, h/e

ϕ	Phase of the electronic wavefunction
Ψ	Digamma function
ψ	Electronic wavefunction
$<\psi>$	Superconducting order parameter

List of Figures

Figure		Page
I-1	Resistance as a function of temperature: the localization correction to the low temperature resistance	3
II-1	Time-reversed and non-time-reversed electron trajectories in a wire	12
II-2	Time-reversed and non-time-reversed electron interference paths in a ring	16
II-3	Diagrammatic representation of a typical term in the series for the Cooperon	25
II-4	Orientation of a narrow wire in a magnetic field for measurement of 1D localization effects	27
III-1	Basic lithographic fabrication sequence	63
III-2	Edge-defined patterning techniques	64
III-3	X-ray lithography process	68
III-4	Range of secondary photoelectrons in PMMA as a function of x-ray photon energy	72
III-5	Schematic diagram of the x-ray exposure system	74
III-6	Absorption coefficient as a function of x-ray photon wavelength for several x-ray mask materials	77
III-7	X-ray mask fabrication process	78
III-8	SEM micrograph of a portion of an x-ray mask pattern	84
III-9	Removal of glass substrate from x-ray mask membrane and bonding of membrane to Vespel ring	85
III-10	Effects of penumbral blurring and geometric distortion	87
III-11	Maintenance of intimate contact between x-ray mask and substrate via electrostatic holddown	88
III-12	SEM micrograph of an x-ray mask pattern for ultranarrow wires	90

III-13	SEM micrograph of an x-ray mask showing tearing of the mask membrane	91
III-14	TEM micrograph of a PMMA/PMMA bilayer resist profile	94
III-15	SEM micrograph of an x-ray fabricated wire	99
III-16	Electrical contact pad pattern formed by DUV lithography	103
III-17	Electron-beam lithography system	104
III-18	Narrow wire defined by electron-beam lithography	106
III-19	Electron-beam fabricated rings used for Aharonov-Bohm experiments	107
IV-1	Schematic diagram of the three-terminal resistance measuring apparatus	111
IV-2	Four-terminal resistance measuring apparatus	112
V-1	Magnetoresistance for sample Al4 at three representative temperatures	122
V-2	Magnetoresistance for sample Al2a at three representative temperatures	124
V-3	Magnetoresistance for sample Al2b at 2 K showing deviation of data from 1D theory	125
V-4	Magnetoresistance for sample Ag1 at three representative temperatures	126
V-5	Magnetoresistance for sample Al2a at 3 K showing separate contributions from singlet, triplet and Maki-Thompson terms	128
V-6	Magnetoresistance for sample Al2a at 8 K showing separate contributions from singlet, triplet and Maki-Thompson terms	129
V-7	Magnetoresistance for sample Al2a at 15 K showing separate contributions from singlet, triplet and Maki-Thompson terms	130
V-8	Magnetoresistance for sample Al7 at three representative temperatures	132
V-9	Magnetoresistance of ring R1 at 1.7 K showing h/2e oscillations	134
V-10	Magnetoresistance of ring R4 at 1.3 K showing h/e and h/2e oscillations	135

V-11	Phase breaking rate vs. temperature for wires of width $< \ell_T$	140
V-12	Electron-electron contribution to the phase breaking rate vs. wire width	143
V-13	Phase coherence length vs. temperature for sample Al4	145
V-14	Spin-orbit scattering time as a function of elastic scattering time	148

List of Tables

Table		Page
V-1	Sample parameters for narrow wires	119
V-2	Sample parameters for rings	120
V-3	Fitting parameters to Eq. (V-5) for wires of width $< \ell_T$	141
V-4	Fitting parameters to Eq. (V-4) for wires of width $> \ell_T$	146

I. Introduction

The physics of small structures has become the focus of much attention among solid state scientists in recent years. One reason for this interest is the fact that there exist certain phenomena which occur only at these small size scales. In addition, an understanding of the processes and interactions that occur on the microscopic size scale may help to shed light on those which take place in macroscopic systems, which are themselves composed of "blocks" of smaller structures. New tools are also becoming available for creating and for probing microstructures. One such example is the scanning tunneling microscope [Binnig and Rhorer, 1982], which has atomic resolution. Much can also be learned from structures that are larger - a few hundred or a few thousand times the atomic scale. This work deals with quantum mechanical effects in electron transport in such structures.

I.A. Quantum Interference Phenomena

The classical Drude theory has been very successful in providing a basis for understanding the electronic conduction in metals. Where the Drude theory has failed, incorporation of some rudimentary quantum mechanical notions has ably made up for these failures. Anderson [1958] was the first to treat an important quantum mechanical deviation from the classical Drude conductivity in a disordered metal. The deviation considered by Anderson is caused by the introduction of randomness to a perfectly periodic potential in a crystalline solid, which may lead to the spatial localization of electron wavefunctions at impurity sites (impurities are taken here to refer to any departure from ideal crystal structure). The Drude theory predicts that

at low temperatures the resistance of a metal will reach a constant value determined by the concentration of static impurities or defects. Anderson pointed out that this will be the case only for systems in which the electron wavefunctions are extended throughout the metal. In the presence of disorder, the electron wavefunctions can become localized due to the presence of impurities. Due to the localization of the wavefunctions, conduction is impossible at zero temperature in one- and two-dimensional systems, and the resistance is infinite. Thus, the disordered metal becomes an insulator at zero temperature.

In recent years, Thouless [1977] and Abrahams et al. [1979], using a scaling theory, established the conditions under which weak localization effects can be observed in real samples consisting of either narrow wires or thin films. (Weak localization occurs in metals that are not too highly disordered. The criterion for this regime is $k_F \ell >> 1$, where k_F is the Fermi wavevector and ℓ is the elastic mean free path, determined by the scattering of electrons from impurities.) Thouless and Abrahams et al. predicted that at low temperatures, the resistance of a sample will increase above the residual resistance value, and would continue to increase as the temperature is decreased. This behavior is pictured schematically in Fig. I-1. The temperature dependence of this effect is a result of the scattering of electrons out of their localized states. This scattering is governed by some inelastic (or more correctly, as we shall see later, phase breaking) mechanisms, which are temperature dependent and which affect the phase of the wavefunction of the localized electrons.

The theoretical prediction by Thouless was very striking. He argued that a real metal of finite dimensions would behave as if it were one-dimensional (1D) with respect to localization effects if certain conditions were met. The most important

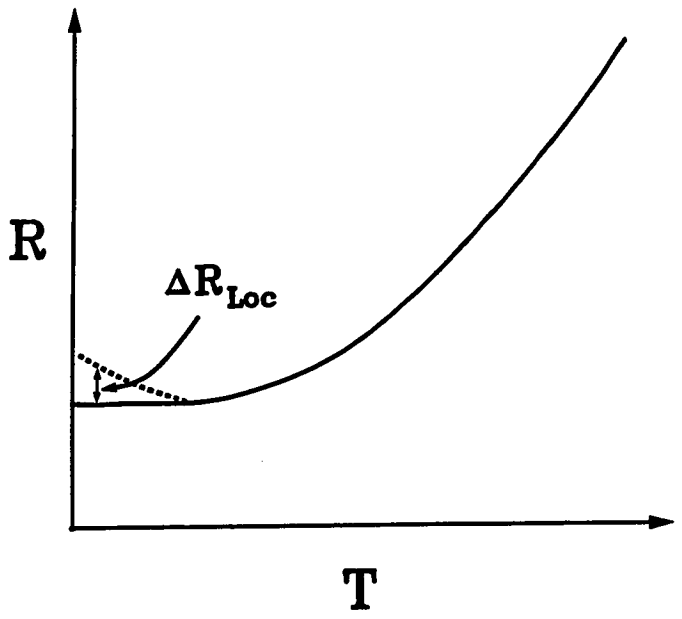

Fig. I-1. Resistance as a function of temperature: the localization correction to the Drude resistance of an impure metal, according to Thouless.

condition is that the sample's lateral dimensions (width and thickness) be less than the inelastic scattering length. This length may be relatively long at low temperatures - on the order of 1 μm. Early experiments on narrow wires only a few hundred Angstroms wide which attempted to test Thouless' theory [Giordano et al., 1979; Chaudhari and Habermeier, 1980] appeared to verify his predictions. However, the electron phase breaking rates inferred from their results were not consistent with any known electron scattering mechanism.

These results as well as results on two-dimensional (2D) metal films and MOSFETS (Metal-Oxide-Semiconductor-Field-Effect-Transistors) spurred on a great deal of theoretical and experimental activity. Another effect, due to electron-electron interactions [Altshuler et al., 1980], was suggested as an alternative explanation for the results of early localization experiments. This effect is based on the inclusion of the screened Coulomb interaction between electrons in the presence of random disorder. This leads to changes in the electronic density of states near the Fermi energy. The manifestation of this effect comes in the form of a rise in the low temperature resistance with decreasing temperature, closely resembling the resistance rise due to localization. The existence of electron-electron interaction effects raised questions as to the real cause of the results observed in the early localization experiments.

In the wake of the early experiments, a better understanding of localization effects was being pursued. A microscopic theory of localization [Altshuler et al., 1981b and 1982a] confirmed the predictions of the scaling theory and was also able to include the effects of a magnetic field, as well as the effects of spin-orbit and magnetic spin-flip scattering. This new theoretical framework found a way to

distinguish between weak localization effects and electron-electron interactions by the application of a weak magnetic field. It seems that the quantum interference that causes localization is very sensitive to small magnetic perturbations, while the Coulomb interactions are affected only by much larger magnetic fields. It was also seen that spin-orbit scattering can actually reverse the sign of localization effect. In addition, similar effects due to superconducting fluctuations above the transition temperature (for superconducting materials) were dealt with in a quantitative fashion by Larkin [1980].

I.B. Electron Scattering Mechanisms

One of the puzzles that resulted from the early localization experiments had to do with the inelastic scattering rates inferred from the experimental data. The scattering rates inferred in early experiments were not consistent with any of the established mechanisms of electron scattering: electron-phonon scattering and electron-electron scattering. One of the important topics addressed by the microscopic theory was the scattering of electrons by other electrons. New predictions were forthcoming on a qualitatively different type of electron-electron scattering. This involved the effects of scattering events with small energy transfers (quasielastic scattering), or the scattering of electrons by electromagnetic fluctuations. The existence of this new mechanism, together with the already established scattering mechanisms, could be tested by careful analysis of results of localization experiments.

Soon after the predictions of the microscopic theory became available, several experiments on 2D films confirmed many aspects of the theory. Extensions of the

microscopic theory to include spin-orbit scattering and superconducting fluctuations in one-dimensional systems [Santhanam et al., 1984a] set the stage for experiments which could more rigorously test the predictions of localization theory in narrow metallic wires. As will be seen in Chapter II, such experiments could also be used to discern the quasielastic electron-electron scattering mechanism. These experiments form the major part of this thesis.

I.C. The Aharonov-Bohm Effect in Metals

An interesting prediction of the microscopic theory of quantum transport occurs in multiply-connected samples. If, for example, a narrow wire is closed upon itself to form a ring, then in the presence of a magnetic field, the conductivity will oscillate as a function of magnetic field. The oscillations are periodic in the magnetic flux, with a period of h/2e, where h is Planck's constant and e is the electronic charge [Altshuler et al. 1981c]. This is analogous to the Aharonov-Bohm effect [Aharonov and Bohm, 1959] in vacuum, which demonstrates explicitly the wave nature of the electron. An alternate theory, based on the Landauer formula for adding series resistances [Landauer, 1970; Anderson et al., 1980], predicted oscillations with a flux period of h/e [Gefen et al., 1984; Buttiker et al., 1985]. Experiments on arrays of rings and cylinders (see, e.g., [Chandrasekhar et al., 1985] for a review of previous experiments) confirmed the theory of Altshuler et al. Early experiments on individual rings [Skocpol et al., 1984; Blonder, 1984; Umbach et al., 1984] failed to observe the predicted oscillations. The first clear observation was by Webb et al. [1985], who found h/e oscillations in a single gold ring. Part of the work in this thesis involved an effort to observe both types of oscillations in a single ring and to understand the conditions under which these oscillations can be

observed.

I.D. Microfabrication

The effects studied in this work appear only in ultrasmall structures. Micron-size rings and wires with widths much less than 1 μm are necessary for the observation of these effects. This would be impossible without the use of microfabrication techniques which go beyond the current state-of-the-art in the microelectronics industry. A significant portion of the work presented here involved ultrahigh resolution microlithographic patterning using electron-beam and x-ray lithography. These techniques have been available to a varying extent for the fabrication of small structures for several years, although they are not commonly used to reach the dimensions achieved in this work. In fact, while we have not set any absolute records in terms of smallness of features, we have fabricated structures which are among the smallest in the world using relatively modest equipment. This was made possible through the implementation of some novel "tricks" and clever techniques, some of which are not standard in most microfabrication schemes. Of course, this can be done in a university laboratory, where the demands of the fabrication process are different from those in a manufacturing environment. Some of the techniques we have taken advantage of include the use of a thin bilayer electron-beam resist, which is helpful in achieving small feature size with good processing characteristics and the employment of step edge lithography for the patterning of x-ray masks when no other high resolution patterning method was available. Some of these methods involved the combination of different technologies, resulting in powerful fabrication techniques.

I.E. Outline of this Thesis

This thesis is organized in the following fashion: Chapter II contains a theoretical overview of the quantum interference phenomena studied in this work and the electron scattering mechanisms which are relevant to those phenomena. Included is a discussion of the length scales which play critical roles in determining the magnitudes of the various effects as well as determining the dimensionality of a sample with respect to each effect or mechanism. Precise theoretical predictions are given for those quantities that were studied in this work. In addition, an effort is made to provide a feeling for how these predictions were derived. In Chapter III, a description of the fabrication techniques employed in this work is offered. This includes a detailed account of the electron-beam and x-ray lithography systems used in this work and the technique used for fabricating x-ray masks. In Chapter IV, the experimental arrangement for low temperature electrical measurements is described. Chapter V contains a review of the experimental results of the low temperature measurements on narrow wires and rings along with an analysis of these results in terms of the theoretical predictions presented in Chapter II. In Chapter VI, we compare these results with work done by other investigators. Chapter VII contains a summary of the results in this work and their implications for future work.

Some of the work described in this thesis has already been published in various journal articles. An extension of the theory of weak localization to include spin-orbit scattering and superconducting fluctuations in one-dimensional systems is given in [Santhanam et al., 1984a]. Results of experiments studying these one-dimensional effects can be found in [Santhanam et al., 1984b], [Santhanam et al., 1985] and [Santhanam et al., 1987]. Results of experiments probing a one-dimensional electron-

electron scattering rate are contained in [Wind et al., 1986]. The implementation of a thin bilayer electron-beam resist in our fabrication work is described in [Rooks et al., 1987].

II. Theory

II.A. Quantum Interference Phenomena - Qualitative Features

The classical theory of metals has proved remarkably successful in describing most of the features of electronic conduction. It is well accepted that the low temperature conductivity, σ, is dominated by the scattering of electrons by impurities and is given by the Drude formula [Ashcroft and Mermin, 1976]:

$$\sigma = \frac{ne^2\tau}{m} . \qquad \text{(II-1)}$$

τ is the elastic scattering time, related to the elastic mean free path, ℓ, by $\tau = \ell/v_F$, with v_F the Fermi velocity. For a given sample, as the temperature nears absolute zero, the resistivity, $\rho = 1/\sigma$, approaches a constant value, the residual resistivity, determined only by the average impurity concentration in the sample. There exist a number of quantum effects which lead to deviations from this constant residual resistivity. These include localization, electron-electron interactions, Maki-Thompson superconducting fluctuations and Aslamazov-Larkin superconducting fluctuations. Also present at low temperatures are the "classical" contributions to the resistivity from electron-phonon scattering as the temperature is increased, and classical magnetoresistance [Ashcroft and Mermin, 1976]. In general, the total resistance at low temperatures will be the residual resistance plus the sum of these corrections. For the samples studied in this work, the important contributions are due to localization and Maki-Thompson fluctuations.

II.A.1. Weak Localization

Electron quantum interference effects involve the interference of electron waves as they traverse a disordered solid. Each possible electron trajectory has associated with it a probability amplitude, ψ, whose modulus squared, $<|\psi(\vec{r})|>^2$ gives the probability of finding the electron at the point $\vec{r}$. Different electron trajectories emanating from the same starting point can interfere constructively some distance later as long as they are in phase. To the extent that free electrons in metals can be described by plane waves, such that $\psi = \psi_o e^{(i\vec{k}\cdot\vec{r}-iEt/\hbar)}$, the phase, ϕ, would be given by $\phi = \vec{k}\cdot\vec{r} - Et/\hbar$. It is surprising that these quantum interference effects can occur despite the presence of impurities which elastically scatter electrons along the way. However, the scattering of an electron by an impurity does not actually destroy phase coherence, as will be discussed below.

There are two classes of interference paths which contribute quantum corrections to the low temperature resistance: time-reversed paths, where the electron trajectories are identical except that they are traversed in the precise time-reversed order, as shown schematically in Fig. II-1a, and non-time-reversed paths, where the electron trajectories follow different routes, as in Fig. II-1b. Clearly, the interference for the time-reversed paths must occur at the point of origin. The interference due to time-reversed paths leads to the weak localization effect, while the interference due to non-time-reversed paths leads to universal conductance fluctuations [Stone, 1985; Lee and Stone, 1985].

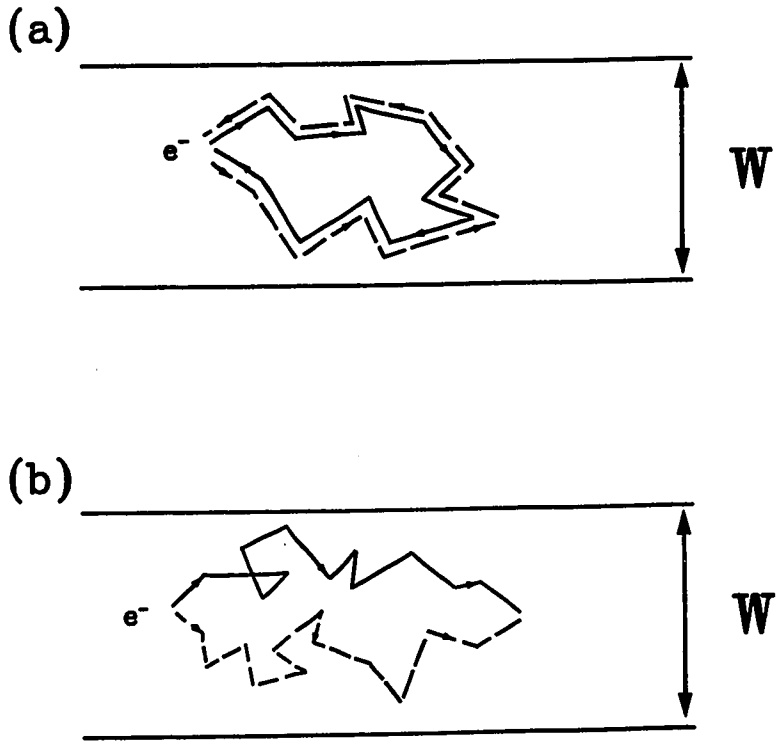

Fig. II-1. (a) Schematic representation of electron partial waves following time-reversed trajectories being elastically scattered by impurities and interfering at the point of origin. (b) Interference of non-time-reversed trajectories.

Two appealing physical pictures have been put forth to describe the weak localization effect. The first one, suggested by Bergmann [1983 and 1984a], follows the evolution of the electron wavefunction in momentum space as an electron undergoes a series of elastic scattering events. The second description, first offered by Khmelnitskii [1984], gives a real space picture of possible interference paths. We will use Khmelnitskii's description.

The total probability, $P(\vec{r})$, for finding an electron at any point $\vec{r}$ in a sample is given by the square of the sum of the probability amplitudes associated with all the possible paths the electron can traverse. Thus,

$$P(\vec{r}) = |\Sigma_i \psi_i|^2 \ . \qquad \text{(II-2)}$$

Quantum mechanically, this is equal to the classical probability to find the electron at the point $\vec{r}$ plus an interference term:

$$P(\vec{r}) = \sum_i |\psi_i|^2 + \sum_{i \neq j} \psi_i \psi_j^* \ , \qquad \text{(II-3)}$$

with ψ_j^* denoting the complex conjugate of ψ_j. For the two paths in Fig. II-1b, the interference term can be quite small, depending on the individual impurity-determined scattering sequence for each path, as each path is comprised of its own set of impurities. For many such paths, the fractional contribution of the interference term will be negligible compared to the classical contribution.

Looking now at the time-reversed paths in Fig. II-1a, we have

$$
\begin{aligned}
P(O) &= |\psi_1|^2 + |\psi_2|^2 + \psi_1\psi_2^* + \psi_1^*\psi_2 \\
&= |\psi_1|^2 + |\psi_2|^2 + 2\mathrm{Re}(\psi_1^*\psi_2) \\
&= 4|\psi_1|^2
\end{aligned}
\qquad \text{(II-4)}
$$

since paths 1 and 2 are exact time-reversed pairs. Thus, for time-reversed paths, the probability of finding an electron at point O is actually twice the classical probability. Because of this increased probability, the electron is said to be "weakly localized" at point O. The result is measured as an increase in the resistance over the classical Drude resistance.

The interference between electron waves traversing different paths is possible only as long as the electrons are phase coherent. That is, as long as there is a specific spatial and temporal relationship between their phases. This phase coherence persists despite the elastic scattering from impurities along each path. However, the phase coherence can be disturbed by certain events, called "phase breaking events", which cause the electrons to lose phase memory. Examples of such phase breaking events are the scattering of an electron by a phonon or by other electrons. These scattering events are non-energy-conserving, and they alter the energy-time portion of the electron phase. They will be discussed in detail later in this chapter. The important thing to note is that the frequency with which these phase breaking events occur is temperature-dependent. The phase breaking events become more frequent as the temperature is increased. As the temperature is raised, more and more events occur which can destroy the phase coherence between the interfering time-reversed paths, until only the shortest such paths can interfere. This in turn gives a temperature dependence to the weak localization effect, which was embodied in Thouless' original prediction [1977] and is shown schematically in Fig. I-1. As the

temperature rises, the extra resistance due to localization is decreased.

If a magnetic field, $\vec{H}$, is turned on such that it threads the electron paths (i.e., perpendicular to the plane of the paper in Fig. II-1), then the phases of the electron wavefunctions acquire an additional factor due to the presence of the magnetic vector potential, $\vec{A}$:

$$\phi = i\vec{k}\cdot\vec{r} - iEt/\hbar \rightarrow i\vec{k}\cdot\vec{r} - iEt/\hbar + \frac{ie}{\hbar c}\oint \vec{A}\cdot d\vec{l} \ . \qquad \text{(II-5a)}$$

Thus,
$$\psi_1 \rightarrow \psi_1 e^{i2\pi\Phi/\Phi_o} \qquad \text{(II-5b)}$$

and
$$\psi_2 \rightarrow \psi_2 e^{-i2\pi\Phi/\Phi_o} \ , \qquad \text{(II-5c)}$$

where $\Phi = \oint \vec{A}\cdot d\vec{l}$ is the magnetic flux enclosed by the electron trajectories, and $\Phi_o = hc/e$ is the magnetic fluxoid or flux quantum. The difference in sign arises from the fact that the two electron paths enclose the magnetic flux in opposite senses. As the magnetic field is increased, the interference term diminishes. The result is a negative magnetoresistance. It should be noted that this effect manifests itself in magnetic fields where the classical magnetoresistance is essentially zero ($\omega_c\tau << 1$, where ω_c is the cyclotron frequency).

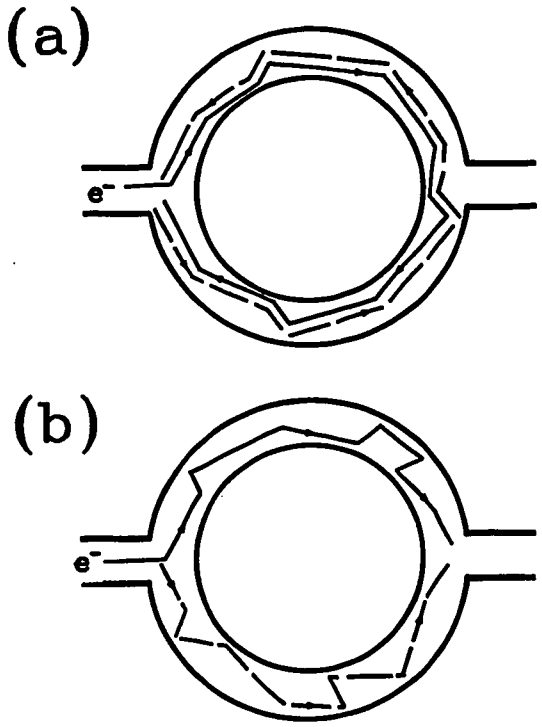

Fig. II-2. (a) Time-reversed interference paths constrained to the geometry of a ring. A magnetic flux normal to the page modulates the phase of the wavefuctions so that the ring resistance oscillates with a magnetic flux period of hc/2e. (b) Non-time-reversed interference paths leading to magnetoresistance oscillations of period hc/e.

II.A.2. Aharonov-Bohm Oscillations in Rings

Consider now the case where the electron trajectories coincide with the geometry of the sample, as in Figs. II-2a and II-2b, where the sample is in the form of a ring. In the absence of any scattering events which will cause loss of phase memory, electron partial waves emanating from the ring entrance can interfere at the exit of the ring, as in Fig. II-2b, or at the entrance of the ring after traveling all the way around, as in Fig. II-2a. One must keep in mind that the electron motion within the arms of the ring is diffusive. Thus, the trajectories pictured in Figs. II-2a and II-2b are exactly analogous to those in Figs. II-1a and II-1b, except that now these trajectories coincide with sample geometry. The trajectories pictured in Fig. II-2a are time-reversed paths. In an applied magnetic field, the phase difference between paths 1 and 2 will be $2\pi\Phi/\Phi_o$, where Φ is the flux enclosed within the ring. Therefore, the probability of finding an electron at the entrance of the ring will oscillate with a period of $\Phi_o/2 = hc/2e$.

For the paths shown in Fig. II-2b, the electron trajectories which interfere at the ring exit enclose only half as much flux as those of Fig. II-2a. Thus, for Fig. II-2b, the oscillations will have a period of $\Phi_o = hc/e$. This hc/e oscillation effect is related to the universal conductance fluctuations effect, while the hc/2e oscillations are related to the weak localization effect.

II.A.3. Spin-Orbit Scattering

Throughout the preceding discussion, the electron spin has been ignored. It turns out that in most normal metals spin-orbit scattering has a profound effect on

the observation of weak localization. Hikami et al. [1980] were the first to point out that spin-orbit scattering would reverse the sign of the localization contribution to the temperature dependence of the resistance as well as the magnetoresistance. The physical origin of this [Bergmann, 1984a] lies in the fact that for particles of spin 1/2, a rotation by 2π reverses the sign of the spin state. A rotation of 4π is needed to rotate the state into itself [Shankar, 1980]. In the case of electron quantum interference, if the interfering waves have had their spins rotated by 2π, then instead of constructive interference of the backscattered waves, destructive interference will result.

When the spins are taken into account, the interference term in Eq. (II-4) can be written as [Altshuler et al., 1985]

$$\frac{1}{2}\begin{bmatrix} \psi_{\alpha}^{(1)} & \psi_{\beta}^{(2)} & \psi_{\beta}^{(1)*} & \psi_{\alpha}^{(2)*} \end{bmatrix}, \tag{II-6}$$

with α and β the spin indices for particles (1) and (2). In the total spin representation, we would have

$$\Psi_{1,\pm 1} = \psi_{\pm}^{(1)}\psi_{\pm}^{(2)} \tag{II-7a}$$

$$\Psi_{1,0} = \frac{\sqrt{2}}{2}\left[\psi_{+}^{(1)}\psi_{-}^{(2)} + \psi_{-}^{(1)}\psi_{+}^{(2)}\right] \tag{II-7b}$$

$$\Psi_{0,0} = \frac{\sqrt{2}}{2}\left[\psi_{+}^{(1)}\psi_{-}^{(2)} - \psi_{-}^{(1)}\psi_{+}^{(2)}\right] \tag{II-7c}$$

so that the intererence term becomes

$$\frac{1}{2}\sum_{m=-1}^{1} |\psi_{1,m}|^2 - \frac{1}{2}|\psi_{0,0}|^2 . \tag{II-8}$$

The first term is the triplet term, containing information on the electron spin, while the second term is the singlet term, which is spin independent, as in the case of the He atom [Bethe and Salpeter, 1957]. The triplet term is reduced by spin-orbit scattering as well as by other phase-breaking events, while the singlet term is affected only by the latter. The overall effect of spin-orbit scattering is not to destroy the interference that leads to weak localization, but rather to modify it by splitting the wavefunction as prescribed above [Altshuler and Aronov, 1985].

II.A.4. Scattering by Magnetic Impurities

When magnetic impurities are present in the sample, the spin of the electron may interact with the magnetic moment of the impurity. While the precise mechanism by which magnetic scattering operates is not yet clear and is currently the subject of investigation [Bergmann, 1986; Vranken et al., 1986], the effect on weak localization has been experimentally confirmed. Magnetic scattering tends to suppress quantum interference, with the magnetic impurities either acting as sources of magnetic flux, which adds to the phases of the time-reversed trajectories so as to diminish the interference, or as centers of spin-flip scattering, which rotates the electron spins and destroys phase coherence.

II.B. Length Scales and Dimensionality

In many physical systems, certain phenomena may be rendered more easy to understand by considering one- and two-dimensional models of the system. Examples of such phenomena include lattice dynamics and spin interactions [Ashcroft and

Mermin, 1976]. This is true for electron quantum interference effects as well. There is, however, an additional reason for interest in lower dimensionalities in the case of quantum interference phenomena. This is that these systems are not merely theoretical abstractions, but they can be physically attained under certain conditions. This was first realized by Thouless [1977], who predicted that localization effects could be observed in a wire of finite dimensions. In addition, for many of these phenomena, reduction of the system dimensionality results in a relative increase in the magnitude of the effect. This is not necessarily obvious, since lowering the dimensionality of a system reduces the degrees of freedom. However, it is precisely for this reason that quantum interference effects grow larger in smaller systems. In the case of weak localization, for example, this is due to the fact that in one- and two-dimensions, a diffusing electron will, in a sufficiently large interval of time, pass as near its point of origin as desired [Altshuler et al., 1982a]. Thus, the coherent backscattering of time-reversed paths contributes a larger fraction of all possible trajectories in a smaller system. As another example, consider the scattering of electrons by electromagnetic fluctuations (Nyquist noise) [Altshuler et al., 1981a]. As will be discussed in Sec. II.D.1, in order for these fluctuating fields to contribute to the loss of electron phase coherence, they must be uniform over distances on the order of ℓ_ϕ (the phase coherence length). These fields are stronger in small samples since they are confined by the sample's lateral dimensions [Altshuler et al., 1981a], so that this scattering becomes stronger as the sample dimensions are decreased.

The fact is that no sample is strictly one- or two-dimensional unless it is a linear chain of atoms or a single layer of atoms. In the case of transport phenomena, such lower dimensional systems might also include samples whose lateral dimensions are less than the deBroglie wavelength of an electron (~ 4 Å for

aluminum). The only real samples which come close to this are 2D electron gas systems found in MOS (Metal-Oxide-Semiconductor) inversion layers (see, e.g., [Wheeler et al., 1982]), which are only ~ 30 Å thick. However, for the effects considered here, strict one- or two-dimensionality is not necessary. A sample will behave as if it were 1D or 2D (i.e., quasi-1D or quasi-2D) if its lateral dimensions are less than the characteristic length scale for that effect. In essence, the small size of the sample acts as a cutoff for processes that ordinarily extend over longer distances in larger samples. In this section, we will examine the characteristic lengths which play important roles in quantum interference phenomena.

ℓ - the elastic mean free path. This is the average distance between impurity scattering events in a disordered solid. $\ell = v_F \tau$, with v_F the Fermi velocity and τ the impurity scattering time. Since the quantum transport phenomena considered in this work involve the interference of electron waves backscattered by impurities, ℓ is the shortest distance over which this interference can occur. For the moderately disordered samples of Al and Ag studied in this work, ℓ ~ 50 - 100 Å.

ℓ_ϕ - the phase coherence length. As an electron diffuses through a solid, the evolution of the temporal and spatial components of its phase are determined by the energy state of the electron and the momentum changes caused by impurity scattering. At some point, an event may occur which alters this phase evolution. This is a phase breaking event and is usually caused by the interaction of the electron with another electron or with a phonon. (These scattering mechanisms will be discussed in Sec. II.D.) ℓ_ϕ is the distance over which electrons retain phase memory. It is related to the phase breaking time, τ_ϕ, through the diffusion constant, D: $\ell_\phi = \sqrt{D\tau_\phi}$. ℓ_ϕ is the characteristic length scale for weak localization

effects, so that when any of the lateral dimensions of a sample are less than ℓ_ϕ, the localization contribution to the low temperature resistance is of a different dimensionality (see Sec. II.C). At low temperatures, ℓ_ϕ is relatively long, $\gtrsim$ 1 μm at 1 K for the samples in this work.

ℓ_{so} - the spin-orbit scattering length. When the spin-1 state of the correlated electrons is rotated by 2π relative to one another, the interference between their backscattered waves becomes destructive [Bergmann, 1984a]. The average distance over which this destructive interference occurs is the spin-orbit scattering length. $\ell_{so} = \sqrt{D\tau_{so}}$, with τ_{so} the spin-orbit scattering time. ℓ_{so} is found to be longest in light elemental metals ($\ell_{so} \sim 1$ μm) and shortest in heavy metals and alloys ($\ell_{so} \lesssim$ 100 Å).

ℓ_2 - the triplet scattering length. This is the distance over which the triplet state, discussed in Sections II.A.3 and II.C.1 decays in the presence of spin-orbit scattering. ℓ_2 is a combination of the spin-orbit scattering length and the phase coherence length: $\ell_2^{-2} = \ell_\phi^{-2} + (4/3)\ell_{so}^{-2}$ When ℓ_ϕ and ℓ_{so} are very different, ℓ_2 is approximately equal to the shorter of the two lengths.

ℓ_s - the magnetic scattering length. This is the average distance over which destruction of phase coherence occurs due to the scattering by magnetic impurities. In systems where magnetic scattering is present, ℓ_ϕ and ℓ_2 are modified, so that $\ell_\phi^{-2} \rightarrow \ell_\phi^{-2} + 2\ell_s^{-2}$, and $\ell_2^{-2} \rightarrow \ell_2^{-2} + (2/3)\ell_s^{-2}$. The range of ℓ_s depends on the concentration of magnetic impurities in a given system and on the strength of their localized moments in the host metal (for example, common magnetic impurities, with the possible exception of Mn, do not display localized moments when diluted in Al

[Ashcroft and Mermin, 1976]).

ℓ_T - the thermal diffusion length (also referred to as the interaction length and the electron-electron correlation length). This is the typical distance over which interelectronic processes take place in a diffusive medium. $\ell_T = (\hbar D/k_B T)^{-1/2}$. This is determined from the following considerations [Altshuler et al., 1982a]: In electron-electron interactions, the interaction time, t, is determined either by the inverse tranferred energy, ΔE, or by the diffusion time, $1/(Dq^2)$, where q is the electron momentum. Thus, $q^2 \sim \Delta E/D$. The range of these interactions is $\sqrt{Dt} = q^{-1} = (\hbar D/\Delta E)^{-1/2}$. ΔE is $\sim k_B T$, so that $\ell_T = (\hbar D/k_B T)^{1/2}$. ℓ_T is the characteristic length scale for electron-electron scattering. ℓ_T is typically $\sim$ 100 Å - 1000 Å at 1 K for moderately disordered metals, and several thousand Å for some semiconductor systems.

λ_p - the thermal phonon wavelength. $\lambda_p = \pi\hbar v_s/2k_B T$, where v_s is the velocity of sound. λ_p is the characteristic length scale for determining dimensionality for electron-phonon scattering. (For dirty systems, ℓ may be the dimensional length scale - see Sec. II.D.) λ_p is $\sim$ 100 Å at low temperatures for the samples studied in this work.

$\xi(T)$ - the superconducting coherence length. This is the characteristic length scale for variations of the superconducting state. It determines the dimensionality of Aslamazov-Larkin superconducting fluctuations (Sec. II.C.3) and is temperature dependent.

It is important to note that a given sample may be of one dimensionality with

respect to one mechanism and of a different dimensionality with respect to another mechanism. In fact, this is most common. We shall see that some of the narrow wires studied in this work manifest 1D localization, while they are 2D with respect to electron-electron scattering and 3D with respect to electron-phonon scattering.

II.C. Quantum Interference Phenomena - Quantitative Predictions

II.C.1. Weak Localization

The interference between electron waves traveling along time-reversed paths is described by a function called the Cooperon [Altshuler, 1982a] (the particle-particle diffusion propagator), $C(\vec{r},\vec{r}')$, which gives the probability of finding an electron at the point $\vec{r}'$ due to quantum interference. The diagrammatic representation for the Cooperon is shown in Fig. II-3. The basic quantum correction to the conductivity of noninteracting electrons is [Gor'kov et al., 1979]

$$\Delta\sigma = -\frac{2e^2 D}{\pi} C(\vec{r},\vec{r}), \qquad \text{(II-9)}$$

with D, the electronic diffusion constant, determined by elastic scattering ($D = v_F \ell/3$; v_F being the Fermi velocity). The Cooperon is determined by the equation

$$\hbar \left[D \left(-i\vec{\nabla} - \frac{2e}{\hbar c}\vec{A}\right)^2 + \frac{1}{\tau_\phi} \right] C(\vec{r},\vec{r}') = \delta(\vec{r} - \vec{r}'). \qquad \text{(II-10)}$$

(Note that this is the Schroedinger equation for a particle of charge 2e and mass

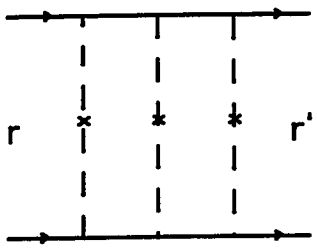

Fig. II-3. Diagrammatic representation of a typical term in the series for the Cooperon, or particle-particle diffusion propagator. In this example, three impurities participate in the scattering. (See [Altshuler and Aronov, 1985] for a detailed discussion of the calculation of the Cooperon.)

$\hbar/2D$ in a magnetic field.) Here $\vec{A}$ is the magnetic vector potential and c is the speed of light. The conditions at the sample boundaries require that the particle flux normal to the sample surface be zero, i.e.,

$$\left[-i\vec{\nabla}_n - \frac{2e}{\hbar c}\vec{A}_n \right] C(\vec{r},\vec{r}') = 0 , \qquad \text{(II-11)}$$

where the subscript n denotes the component normal to the surface of the sample.

The solution to Eq. (II-9) in the absence of a magnetic field is

$$C(\vec{r},\vec{r}') = \sum_q \left[Dq^2 + \frac{1}{\tau_\phi} \right]^{-1}, \qquad \text{(II-12)}$$

with q the electron momentum.

For a rectangular sample of finite dimensions, in the absence of a magnetic field, $C(\vec{r},\vec{r}')$ can be expanded [Altshuler et al., 1982a] in a series of eigenfunctions of the type $\cos(Q_x x)\cos(Q_y y)\cos(Q_z z)$, where

$$Q_x = \frac{\pi l}{L_x} , \quad Q_y = \frac{\pi m}{L_y} , \quad Q_z = \frac{\pi n}{L_z} ,$$

with l,m,n positive integers or zero and L_x, L_y and L_z the sample dimensions. Then Eq. (II-9) yields

$$\frac{\Delta\sigma}{\sigma} = -\frac{2}{\pi n(E)\hbar}\frac{1}{L_x L_y L_z}\sum_{Q_x Q_y Q_z}\left[D(Q_x^2 + Q_y^2 + Q_z^2) + \frac{1}{\tau_\phi} \right]^{-1} . \qquad \text{(II-13)}$$

with n(E) the electron density of states. If the sample is a long narrow wire such that L_y, $L_z \ll L_x$, we can write this as

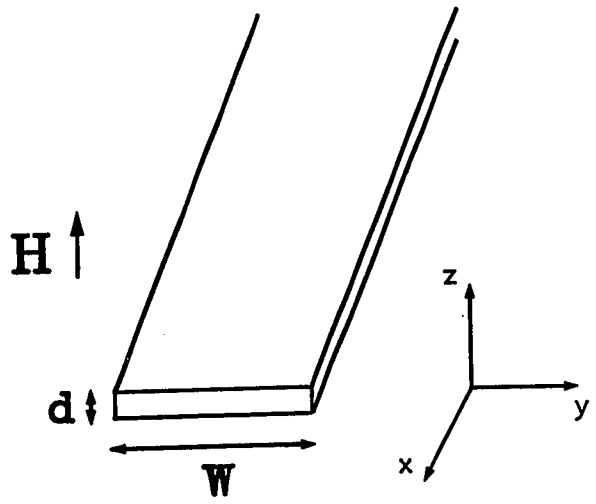

Fig. II-4. Orientation of a narrow wire in a magnetic field for measurement of 1D localization effects.

$$\frac{\Delta\sigma}{\sigma} = -\frac{2}{\pi n(E)\hbar}\frac{1}{L_x L_y L_z}\left\{\sum_{Q_x}\left[DQ_x^2 + \frac{1}{\tau_\phi}\right]^{-1} + \sum_{Q_x;Q_yQ_z\neq 0}\left[D(Q_x^2 + Q_y^2 + Q_z^2) + \frac{1}{\tau_\phi}\right]^{-1}\right\} \qquad \text{(II-14)}$$

The first term in the curly brackets is independent of either Q_y or Q_z, and so it is one-dimensional. If L_y, $L_z << \ell_\phi = (D\tau_\phi)^{1/2}$, then this term is much larger than the second term and thus gives the one-dimensional correction to the conductivity.

Altshuler and Aronov [1981a] treated the specific case of a narrow wire in a perpendicular magnetic field. The wire runs along the x-axis, with its width, W, along the y-axis and thickness, d, along the z-axis. The magnetic field is oriented along the z-axis, as depicted in Fig. II-4. In this case, the Cooperon is given by

$$C(y,y') = \sum_q C_{qx}\psi_{qx}(y)\psi_{qx}(y') \ , \qquad \text{(II-15)}$$

where

$$C_{qx} = \frac{1}{\hbar\,(Dq_x^2 + D/\ell_H^2 + 1/\tau_\phi)} \ . \qquad \text{(II-16)}$$

with $\ell_H = \sqrt{3}\hbar c/eHW$. Therefore,

$$C(y,y') = \int \frac{dq_x}{2\pi\hbar}\frac{\psi_{qx}(y)\psi_{qx}(y')}{E_{qx} + 1/\tau_\phi} \qquad \text{(II-17)}$$

where ψ_{qx} and E_{qx} are the eigenfunctions and eigenvalues, respectively, of the equation

$$\hbar \left[D \left(-i\vec{\nabla} - \frac{2e}{\hbar c} \vec{A} \right)^2 + 1/\tau_\phi \right] \psi_{qx}(y) = E_{qx} \psi_{qx}(y) \qquad \text{(II-18a)}$$

with the boundary condition

$$\left. \frac{\partial \psi_{qx}}{\partial y} \right|_{y=\pm W/2} = 0 \; . \qquad \text{(II-18b)}$$

Perturbation theory for small magnetic fields gives for the ground state energy

$$E_{qx} = D \left[q_x^2 + \frac{1}{\ell_H^2} \right] . \qquad \text{(II-19)}$$

Thus,

$$C(y,y') = \frac{1}{2\pi\hbar D} \int dq_x \left[q_x^2 + \frac{1}{\ell_H^2} + \frac{1}{D\tau_\phi} \right]^{-1} . \qquad \text{(II-20)}$$

The upper limit of integration is chosen to be the maximum value of q_x, which corresponds to the shortest distance over which the Cooperon interference can take place: the elastic mean free path, ℓ. This yields

$$C(\vec{r},\vec{r}') = \frac{1}{2\hbar} \left[\ell_\phi^2 + \ell_H^2 \right]^{-1/2} \qquad \text{(II-21)}$$

Upon substituting this in the expression for the localization correction to the one-dimensional conductivity, Eq. (II-9), we have

$$\Delta\sigma_{1D} = -\frac{e^2}{\pi\hbar}\left[\ \ell_{\tilde{\phi}}^{-2} + \ell_{\tilde{H}}^{-2}\ \right]^{-1/2}. \qquad \text{(II-22)}$$

The total fractional change in resistance for a sample of length, L, and width, W, is then

$$\frac{\Delta R^{Loc}(T,H)}{R} = -\frac{R}{L}\Delta\sigma_{1D} \qquad \text{(II-23a)}$$

$$= -\frac{R_{\square}}{\pi\hbar/e^2\ W}\left[\ \ell_{\tilde{\phi}}^{-2} + \ell_{\tilde{H}}^{-2}\ \right]^{-1/2}. \qquad \text{(II-23b)}$$

$$\equiv f_{1D}(H,\ell_{\phi}). \qquad \text{(II-23c)}$$

The perturbation calculation used by Altshuler and Aronov [1981a] to obtain this result is valid for magnetic fields which are small compared to the characteristic field $H_W = \hbar c/4eW^2$. More precisely, the condition for the validity of Eq.(II-23) is $H < 12.5H_W$, i.e., fields which are small enough so that the width of the sample remains less than the Landau orbit size, $(\hbar c/2eH)^{1/2}$. For most samples which are one-dimensional with respect to localization ($W < \ell_{\phi}$), this restriction still leaves a sufficiently wide field range over which the theory is valid (for the samples in this study, $H_W \sim$ 1KG). For larger magnetic fields, additional terms in Eq. (II-15) must be taken into account.

When the sample width exceeds ℓ_{ϕ}, the sample becomes two-dimensional with respect to localization. In this case, the fractional change in resistance in a perpendicular magnetic field due to localization is [Hikami et al., 1980]

$$\frac{\Delta R}{R} = \frac{R_\square}{2\pi^2\hbar/e^2}\left[\Psi(1/2 + H_\phi/H) + \ln(H_o/H)\right] \qquad \text{(II-24a)}$$

$$\equiv f_{2D}(H, \ell_\phi). \qquad \text{(II-24b)}$$

Here, $H_\phi = \hbar c/4e\ell_\phi^2$, $H_o = \hbar c/4e\ell^2$, and $\Psi(x)$ is the digamma function.

II.C.1a. Spin-Orbit Scattering

As discussed in the previous section, the role of spin-orbit scattering in weak localization is to split the Cooperon into two terms which depend on the electron spin state [Altshuler and Aronov, 1985]. Eq. (II-17) then becomes

$$C(y,y') = \frac{3}{2}\int \frac{dq_x}{2\pi\hbar} \frac{\psi_{qx}(y)\ \psi_{qx}(y')}{E_{qx} + 1/\tau_2} - \frac{1}{2}\int \frac{dq_x}{2\pi\hbar} \frac{\psi_{qx}(y)\ \psi_{qx}(y')}{E_{qx} + 1/\tau_\phi}, \qquad \text{(II-25)}$$

where $1/\tau_2 = 1/\tau_\phi + (4/3)\tau_{so}$, with $1/\tau_{so}$ the spin-orbit scattering rate. The first term is the triplet term, while the second term is the singlet. If the sample width is less than ℓ_ϕ and ℓ_2, then the expressions for the fractional resistance change for each term will have the one-dimensional form [Eq.(II-23)] with ℓ_2 substituted for ℓ_ϕ in the triplet term. Thus,

$$\frac{\Delta R}{R} = \frac{R_\square}{\pi\hbar/e^2}\left[\frac{3}{2}\left(\ell_2^{-2} + \ell_H^{-2}\right)^{-1/2} - \frac{1}{2}\left(\ell_\phi^{-2} + \ell_H^{-2}\right)^{-1/2}\right] \qquad \text{(II-26a)}$$

$$= \frac{3}{2} f_{1D}(H, \ell_2) - \frac{1}{2} f_{1D}(H, \ell_\phi). \qquad \text{(II-26b)}$$

Similarly, when the sample is wider than both ℓ_ϕ and ℓ_2, the triplet and singlet terms have the two-dimensional form, again with ℓ_2 substituted for ℓ_ϕ in the triplet:

$$\frac{\Delta R}{R} = \frac{R_\square}{2\pi^2\hbar/e^2}\left\{\frac{3}{2}\left[\Psi(1/2 + H_2/H) + \ln(H_o/H)\right] - \frac{1}{2}\left[\Psi(1/2 + H_\phi/H)\right]\right\} \qquad \text{(II-27a)}$$

$$= \frac{3}{2} f_{2D}(H,\ell_2) - \frac{1}{2} f_{2D}(H,\ell_\phi). \qquad \text{(II-27b)}$$

There can occur a case where the spin-orbit scattering length is shorter than the phase coherence length, so that at certain temperatures a narrow wire may be narrower than ℓ_ϕ but wider than $\ell_2 \sim \ell_{so}$. The sample is said to be in the regime of "mixed dimensionality" [Santhanam et al., 1984a]. In this case, the singlet term will have the one-dimensional form, Eq. (II-23), while the triplet term will have the two-dimensional form, Eq. (II-24). Thus,

$$\frac{\Delta R}{R} = \frac{3}{2} f_{2D}(H,\ell_2) - \frac{1}{2} f_{1D}(H,\ell_\phi). \qquad \text{(II-28)}$$

II.C.1b. Magnetic Scattering

In the presence of magnetic scattering, the total phase breaking rates for the singlet and triplet terms are modified to reflect the reduction of the interference due to the interaction of the spin of the electron with the magnetic moment of the magnetic impurity [Altshuler et al., 1982a]. τ_ϕ^{-1} is replaced by

$$\tau_\phi^{-1} + 2\tau_s^{-1}. \qquad \text{(II-29a)}$$

τ_2^{-1} is replaced by

$$\tau_2^{-1} + (2/3)\tau_s^{-1} = \tau_\phi^{-1} + (4/3)\tau_{so}^{-1} + (2/3)\tau_s^{-1}. \qquad \text{(II-29b)}$$

II.C.2. Aharonov-Bohm Oscillations in Rings

For the case of a ring geometry, there are two predictions for the oscillatory behavior of the magnetoresistance, each based on a different theoretical framework. The first prediction is due to Altshuler et al. [1981c] and is the result of solving for the Cooperon with the boundary conditions imposed by the ring geometry. As in the case of weak localization, the contributing electron trajectories here are time-reversed paths only. The fractional change in resistance as a function of magnetic field is[1].

$$\frac{\Delta R}{R} = -\frac{\tilde{\ell}_\phi R_\square}{2W(h/2e^2)}\left\{1 + \cos\left[\frac{2\pi\Phi}{h/2e}\right] e^{-2\pi r/\tilde{\ell}_\phi}\right\} + \frac{3\tilde{\ell}_2 R_\square}{2W(h/2e^2)}\left\{1 + \cos\left[\frac{2\pi\Phi}{h/2e}\right] e^{-2\pi r/\tilde{\ell}_2}\right\}. \qquad \text{(II-30)}$$

---

[1]In this section, we retain the notation commonly used in the literature for Aharonov-Bohm oscillations, where the results are expressed in MKS units, and the magnetic flux density, B, is used instead of the magnetic field strength, H. This way, the period of oscillation is given in terms of h/e or h/2e.

Here, r is the radius of the ring, Φ is the flux enclosed by the ring, $\tilde{\ell}_\phi$ is the magnetic field dependent phase breaking length for the singlet term,

$$\tilde{\ell}_\phi^{-2} = \ell_\phi^{-2} + (WeB/3\hbar)^2 + 2\ell_s^{-2} \qquad \text{(II-31a)}$$

with ℓ_ϕ the usual phase breaking length and B the magnetic flux density. $\tilde{\ell}_2$ is the analogous expression for the triplet term, so that

$$\tilde{\ell}_2^{-2} = \ell_2^{-2} + (WeB/3\hbar)^2 + (4/3)\ell_{so}^{-2} + (2/3)\ell_s^{-2} \ . \qquad \text{(II-31b)}$$

For a superconductor above T_c there is an additional term which is equal to the singlet term multiplied by the superconducting fluctuation strength parameter, as will be described in Sec. II.C.3.

As mentioned earlier in Sec. II.A, a second theoretical framework exists, based on the Landauer formula for adding resistances [Landauer, 1970]. This theory calculates the contribution from non-time-reversed trajectories and predicts oscillations with a period of h/e. Currently, a formal prediction is available only for the case where T = 0 and $\ell_\phi > \pi r$ (the "size" of the ring) [Stone and Imry, 1986]:

$$\frac{\Delta R}{R} \sim \frac{0.4R_\square}{h/e^2} \cos\left[\frac{2\pi\Phi}{h/e} + \gamma_o\right] , \qquad \text{(II-32)}$$

with γ_o a phase factor which depends on the specific microscopic impurity configuration of the ring. γ_o varies from sample to sample. At finite temperatures,

thermal averaging over interference paths should reduce the amplitude of the oscillations by a factor of order $\ell_T/\pi r$ [Stone and Imry, 1986]. In addition, when $\ell_\phi \lesssim \pi r$, it is expected that the entire expression would be damped by a factor $\sim \exp(-\pi r/\ell_\phi)$, as in the case for the h/2e oscillations, Eq. (II-30).

II.C.3. Superconducting Fluctuations

Of all quantum effects which appear in metals at low temperatures superconductivity is certainly the most prominent. Below the critical temperature, T_c, the resistance vanishes completely. At temperatures as high as a few degrees above T_c, superconducting fluctuations contribute small corrections to the conductivity which diverge as T_c is approached. These corrections are of two types: direct (Aslamazov-Larkin) fluctuations [Aslamazov and Larkin, 1968] and indirect (Maki-Thompson) fluctuations [Maki, 1968; Thompson, 1970].

II.C.3a. Aslamzov-Larkin (AL) Fluctuations

In a superconductor above T_c, the Ginzburg Landau free energy is minimum when the average superconducting order parameter, $|\psi|$, is zero [Tinkham, 1975], however, thermal fluctuations raising the free energy by $\sim k_BT$ are relatively common. These fluctuations are largest in small volumes, since the total energy increase can only be $\sim k_BT$. This leads to a state of excess Cooper pairs above T_c. The conductivity is increased due to the acceleration of these fluctuation-paired electrons in an applied electric field. This increase can be estimated to be [Tinkham, 1975]

$$\Delta\sigma \sim \frac{(2e)^2}{m^*} \sum_k \frac{<\psi_k>^2 \tau_k}{2} , \qquad \text{(II-33)}$$

where τ_k is the decay time of the superconducting modes. The superconducting charge and mass, 2e and m^* (= 2m), respectively, are used. This expression is analogous to the Drude expression for the normal state conductivity. The temperature dependence of this correction is obtained by carrying out the sum over k-values (or integrating over k-space) in the proper limits. The result is

$$\Delta\sigma \sim \frac{e^2}{\hbar} (T - T_c)^{-(4-d)/2} , \qquad \text{(II-34)}$$

where d is the sample dimensionality with respect to spatial variations of ψ. This correction is actually very small except at temperatures very close to T_c. In fact, for $T \gtrsim 1.3T_c$, the Aslamazov-Larkin contribution is at least an order of magnitude smaller than the weak localization contribution for most of the aluminum samples studied in this work [Santhanam et al., 1987]. However, as mentioned earlier in this section, these fluctuations effects are stronger in samples of smaller volume, and it is possible that AL fluctuations may not be negligible for the narrowest wires studied. The magnetoresistance due to the AL term has been derived in two dimensions by Bergmann [1969] and by Usadel [1969]. An estimate of the one-dimensional contribution can be obtained from a perturbation calculation [Santhanam, private communication], the details of which may be found in Appendix B. The results of this calculation yield

$$\frac{\Delta R}{R} = -\frac{\pi R_{\square}}{16W(\hbar/e^2)} \frac{1}{\xi^2(0)} \left\{ \frac{1}{\xi^2} + \left[\frac{2eH}{\hbar c} \right]^2 \frac{W^2}{2} \right\}^{-3/2} . \qquad \text{(II-35)}$$

ξ is given by $\xi(T) = \xi(0)/[\ln(T/T_c)]^{1/2}$, with $\xi(0)$ the zero temperature coherence length. This expression should be valid only for small magnetic fields, $H << (ck_BT/4De)\ln(T/T_c)$.

II.C.3b. Maki-Thompson (MT) Fluctuations

There exists an additional correction to the conductivity due to an indirect contribution from superconducting fluctuations. This results from the decay of a superconducting fluctuation pair above T_c which leaves two quasiparticles in a state of nearly equal and opposite momentum and spin. Because of time reversal symmetry, these quasiparticles remain correlated as they are elastically scattered by impurities, and they contribute to the conductivity as if they were a Cooper pair. The correlation between the quasiparticles is remarkably similar to the Cooperon which describes the coherent backscattering that causes weak localization. In fact, the form of the Maki-Thompson contribution to the resistance at low temperatures is the same as the weak localization contribution, with the following differences: the MT term is modified by a parameter, β, which characterizes the strength of the correlation beween the quasiparticles [Larkin, 1980], and the MT term is independent of spin-orbit scattering. This is because the electrons are the result of the decay of a superconducting Cooper pair, so that they are already in a state of zero total spin - a singlet state. As in the case of localization, the correlation between the quasiparticles can be broken by the same types of scattering events which limit the lifetime of the Cooperon. In addition, at temperature close to T_c, the quasiparticles

may be scattered by superconducting fluctuations [Patton, 1971], as will be discussed in Sec. II.D.3.

The fractional change in resistance due to Maki-Thompson fluctuations in one-dimension is [Santhanam et al., 1984a]

$$\frac{\Delta R}{R} = - \frac{R_\square}{\pi(\hbar/e^2)W} \beta(T/T_c) \left[\ell_\phi^{-2} + \ell_H^{-2} \right]^{-1/2} \qquad \text{(II-36a)}$$

$$= - \beta(T/T_c)\, f_{1D}(H, \ell_\phi), \qquad \text{(II-36b)}$$

where $\ell_H = 3\hbar c/eHW$, as before, and f_{1D} is defined in Eq. (II-23). This result is valid for small magnetic fields, such that $H << (ck_BT/4De)\ln(T/T_c)$, and for temperatures where $\tau_\phi^{-1} << \hbar k_B T \ln(T/T_c)$.

When the sample width is greater than ℓ_ϕ, then the Maki-Thompson contribution is two-dimensional. Then the fractional change in resistance has the form [Larkin, 1980]

$$\frac{\Delta R}{R} = - \frac{\beta(T/T_c)R_\square}{2\pi^2\hbar/e^2} \Psi \left(1/2 + H_\phi/H \right) \qquad \text{(II-37a)}$$

$$= - \beta(T/T_c)\, f_{2D}(H, H_\phi), \qquad \text{(II-37b)}$$

where f_{2D} is defined in Eq. (II-24). The same restrictions on magnetic field and temperature mentioned above for the 1D case apply to the 2D expression. Recently, expressions have been obtained which extend the limits of the theory for both the

1D case [Gordon and Bindslev-Hansen, 1985] and the 2D case [Lopes dos Santos and Abrahams; Brenig et al., 1985]. For the purpose of this work, Eqs. (II-36) and (II-37) will suffice.

II.D. Electron Scattering Mechanisms

One of the most prominent features of electron quantum interference phenomena is the fact that these effects are all limited by the time (or distance) over which phase coherence is maintained. It is for this reason that these phenomena are observable only at low temperatures, where the phase coherence time is relatively long. Already in the early development of the weak localization theory [Thouless, 1977] it was recognized that the main contribution to the destruction of phase coherence would likely be due to the inelastic scattering of electrons. (The term "inelastic" is used here to describe any type of scattering which does not strictly conserve energy. Distinctions will be made later in this discussion between different types of inelastic scattering.)

There are two mechanisms which are chiefly known to lead to the destruction of phase coherence: electron-electron scattering and electron-phonon scattering. From the results of the earliest localization experiments [Giordano et al., 1979; Chaudhari and Habermeier, 1980] it appeared that neither of these mechanisms could satisfactorily account for the measured phase breaking rates. Other possible mechanisms, such as two-level scattering [Black et al., 1979], were explored. As later investigations showed, those early experiments did not clearly isolate localization effects from electron interaction effects [Altshuler et al., 1980] and also did not account for spin-orbit scattering, and so the phase breaking rates measured

in those experiments were not reliable. Nearly all weak localization experiments on narrow wires, thin films and bulk samples which have been properly analyzed in terms of the appropriate theory have found either electron-phonon scattering or electron-electron scattering or a combination of these two mechanisms to be responsible for the measured phase breaking rates. Thus, in general, the total phase breaking rate, τ_ϕ^{-1}, is given by

$$\tau_\phi^{-1} = \tau_{ee}^{-1} + \tau_{ep}^{-1}, \qquad \text{(II-38)}$$

where τ_{ee}^{-1} is the phase breaking rate due to electron-electron scattering and τ_{ep}^{-1} is the electron-phonon scattering rate. Other mechanisms may contribute to τ_ϕ^{-1} as well, as will be discussed later in this section. In what follows, we will examine these scattering mechanisms in terms of their importance to the destruction of phase coherence and their role in quantum interference phenomena.

II.D.1. Electron-Electron Scattering

II.D.1a. Clean Limit (pure metals)

The issue of electron-electron scattering in simple metals has been the subject of some puzzlement for many years. While a consensus of theoretical predictions has existed regarding the nature of this scattering (and its temperature dependence and approximate magnitude as well) for many years, no experiment had succesfully verified these predictions for the pure metal until only recently. (In fact, while some of the basic features of the theory have been confirmed, certain anomalies still exist. See [Kaveh and Wiser, 1984] for a comprehensive discussion).

Simple considerations [Ziman, 1960; Ashcroft and Mermin, 1976] lead to a scattering rate that is proportional to T^2. This arises from the following phase space argument: at thermal equilibrium, the exclusion principle requires that only those electrons which lie within a thin shell of width $\sim k_B T$ of the Fermi energy can participate in a scattering event. Likewise, the only states which an electron can scatter <u>into</u> must also lie within a shell of width $\sim k_B T$ of E_F. Thus, $\tau_{ee}^{-1} \propto (k_B T)^2$. This does not depend on the specific details of the interaction between electrons. It is due to the fact that the scattering of electrons by one another is accompanied by a substantial momentum transfer which is independent of energy. Thus, the interaction is determined only by the phase volume [Altshuler and Aronov, 1979].

Quantitative predictions for this rate have been carried out by a number of workers. These calculations generally rely on solving the Boltzmann equation for the case of interacting electrons (see [Ziman, 1960]). Estimates based on works by Schmid [1973] and Ziman [1960] (see [Gasparov and Hartunian, 1976]) predict τ_{ee}^{-1} to be

$$\tau_{ee}^{-1} = \frac{\pi}{2} \frac{(k_B T)^2}{\hbar E_F} \ln (E_F/k_B T). \qquad \text{(II-39)}$$

For most metals, this gives a rate that is on the order of $10^5 - 10^6\ T^2\ \text{sec}^{-1}$. Lawrence and Wilkins [1973] calcuated τ_{ee}^{-1} for the specific case of aluminum using a solution to the Boltzmann equation [Jensen et al., 1969] adapted to an anisotropic Fermi surface. They found $\tau_{ee}^{-1} \simeq 2.4 \times 10^5\ T^2\ \text{sec}^{-1}$.

Experimental investigations of the electron-electron scattering rate have included measurements of the low temperature resistivity (see [Wiser, 1984] for a review) and radio frequency size effects [Gasparov and Hartunian, 1976; Wegehaupt and Doezema, 1978]. None of these experiments on simple metals has been successful in verifying all features of the theoretical predictions. (In the case of alkali metals, for example, a T^2 behavior has been observed, however, there exist unexplained sample to sample variations [Kaveh and Wiser, 1984; Wiser, 1984].) It may be considered somewhat ironic that the electron-electron scattering rate is more readily observed in disordered metals, where the rate is larger and effects such as weak localization may be used as probes, while the case of the pure metal remains problematic.

II.D.1b. Dirty Limit (disordered metals)

Although the role of disorder in the interactions between electrons is an indirect one, it has an essential effect which results in a change in the nature of these interactions [Altshuler and Aronov, 1979]. In the absence of impurities, momentum conservation requires that the momentum transferred in a collision between electrons be large, i.e., on the order of k_F. In a moderately disordered system, where an electron typically undergoes many elastic collisions with impurities before interacting with another electron, this requirement is relaxed. Now collisions occur not between free electrons (quasiparticles), but rather between electrons diffusing through a field of (neutral) impurities. In this case, interactions involving small momentum transfers ($q \sim [E/\hbar D]^{1/2}$, where q is the electron momentum and E is the quasiparticle energy relative to the Fermi level) may contribute strongly to

the scattering rate in addition to interactions with large momentum transfers ($q \sim 1/\ell$) [Altshuler and Aronov, 1979]. (This, incidentally, also leads to density of states anomalies [Altshuler and Aronov, 1985].) The additional contribution from small momentum transfer interactions causes an increase in the scattering rate relative to the case of the pure metal as well as a weaker dependence of the rate on temperature. These effects are expected to occur when the degree of disorder is such that $\hbar/\tau >> k_B T$.

The energy relaxation rate due to electron-electron collisions has been derived by several workers. Schmid [1974] and Altshuler and Aronov [1978 and 1979] solved a modified Boltzmann equation for electron-electron interactions which includes scattering by impurities. Abrahams et al. [1981] and Altshuler and Aronov [1981b] calculated the transition probability for one-electron states using perturbation theory with a subsequent averaging over the impurity distribution. Results of these calculations yield a scattering rate which is proportional to $T^{d/2}$, where d is the sample dimensionality. This rate increases with increasing disorder and is also considerably larger than the clean limit rate, as was to be expected. In addition, a divergence appears in the self energy calculation of Abrahams et al. which leads to a logarithmic factor in τ_E^{-1} in two-dimensional systems. Their calculation, including a correction introduced by Lopes dos Santos [1983] yields

$$\tau_E^{-1} = \frac{1}{4\pi} \frac{R_\square}{\hbar/e^2} \frac{k_B T}{\hbar} \ln(4T_1/T). \qquad \text{(II-40)}$$

$T_1 = 9 \times 10^5 (k_F \ell)^3$ for aluminum. Calculations using the kinetic equation approach [Altshuler and Aronov, 1981] do not result in the logarithmic divergence. The

prediction [Altshuler et al., 1982a] for 2D systems is

$$\tau_E^{-1} = \frac{1}{4\pi} \frac{R_\square}{\hbar/e^2} \frac{k_B T}{\hbar} , \qquad \text{(II-41)}$$

and for 1D systems,

$$\tau_E^{-1} = \frac{1}{\sqrt{2}\pi^3} \frac{R_\square}{\hbar/e^2} \frac{D}{W} \left[\frac{k_B T}{\hbar D} \right]^{1/2} . \qquad \text{(II-42)}$$

In the early development of the theory of weak localization it had been assumed that the rate of decay of the quantum interference, τ_ϕ^{-1} coincides with the energy relaxation rate, τ_E^{-1}, which is determined predominantly by inelastic collisions with energy transfers on the order of the electron excitation energy relative to the Fermi energy ($E \sim k_B T$). Altshuler, Aronov and Khmelnitskii [1981a and 1982b] pointed out that electron-electron collisions with small energy transfers ($E << k_B T$) may make an important contribution to the phase relaxation rate. It is possible, they noted, that such processes may cause loss of phase memory in a time shorter than τ_E.

This point is illustrated by Altshuler et al. [1981a] for the case of quasielastic scattering of electrons by phonons, which may take place in metals at temperatures well above the Debye temperature and in degenerate semiconductors at low carrier concentrations. The change in an electron's energy, ΔE, in the time τ_ϕ is

$$\Delta E \simeq \left[\frac{(\delta E)^2 \tau_\phi}{\tau_{coll}} \right]^{1/2}, \qquad \text{(II-43)}$$

where δE is the characteristic energy transferred during each collision and τ_{coll}^{-1} is the frequency of collisions. Phase coherence is destroyed when $\Delta\phi \sim 2\pi$, i.e., when $\Delta E \tau_\phi/\hbar \sim 1$. Therefore,

$$\tau_\phi \simeq \left[\frac{\hbar^2 \tau_{coll}}{(\delta E)^2} \right]^{1/3}. \qquad \text{(II-44)}$$

Similarly, the energy change during the energy relaxation time, τ_E, is given by

$$\Delta E \simeq \left[\frac{(\delta E)^2 \tau_E}{\tau_{coll}} \right]^{1/2}. \qquad \text{(II-45)}$$

τ_E is determined by the condition $\Delta E \sim E$, so that

$$\tau_E \simeq \frac{E^2 \tau_{coll}}{(\delta E)^2}. \qquad \text{(II-46)}$$

If $\delta E << E$, (i.e., small energy collisions) then by comparing Eqs. (II-44) and (II-46) we see that $\tau_E >> \tau_\phi$. Eq. (II-46) is valid as long as $\tau_{coll} << \hbar/E$. When $\delta E \sim \hbar/\tau_{coll}$, then $\tau_\phi \sim \tau_{coll}$, and if $\delta E \sim E$, then τ_ϕ, τ_E and τ_{coll} are all approximately equal. Thus, we see that collisions with small energy transfers can be effective in destroying electron phase coherence.

Electron-electron scattering with small energy transfers is equivalent to the interaction of an electron with the fluctuating electromagnetic fields produced by all the other electrons (Nyquist noise) [Altshuler et al., 1982b]. These fluctuating fields

are present in any sample at finite temperatures. Altshuler et al. [1981a and 1982b] calculated the effect of an external electromagnetic field on the conductivity due to weak localization. They found that even weak fields, such as those due to Nyquist noise, can strongly influence the phase coherence, and in most cases, are likely to provide the dominant contribution to measured phase breaking rates. Although this notion is the result of complex calculations [Altshuler et al., 1981a and 1982b], the general conclusion can be obtained from qualitative considerations [Altshuler et al., 1981a; Chandrasekhar, private communication]. In the presence of an alternating electric field, $\vec{E}$, the change in phase of an electron between the times t=0 and $t=\tau_N$ is given by

$$\Delta\phi = \int_0^{\tau_N} [\delta\epsilon(t) - \delta\epsilon(0)]dt \qquad \text{(II-47)}$$

$$= e\int_0^{\tau_N} dt \int_0^t dt' \; \vec{E}(t')\cdot\vec{v}(t'), \qquad \text{(II-48)}$$

where $\delta\epsilon$ is the work performed by the field on the electron path, and $\vec{v}(t)$ is the electron velocity at the time t. The phase difference is random due to impurity scattering. However, we can estimate the average phase change,

$$\langle(\Delta\phi)^2\rangle = e^2\int_0^{\tau_N} dt \int_0^t dt_1 \int_0^{t_1} dt' \int_0^{t'} dt_1' \langle\vec{E}(t')\vec{E}(t_1')\vec{v}(t')\vec{v}(t_1')\rangle. \qquad \text{(II-49)}$$

If the average is independent of t' and t_1', we obtain

$$\langle(\Delta\phi)^2\rangle = \frac{e^2\langle\vec{E}^2\rangle\,\langle\vec{v}^2\rangle\tau_N^4}{\hbar^2} \quad . \qquad \text{(II-50)}$$

Now, $\langle\vec{v}^2\rangle = \langle\vec{r}^2\rangle/\tau_N^2 \simeq D/\tau_N$. Also, $\langle\vec{E}^2\rangle = \langle V^2\rangle/L^2$, where V is the voltage due to the electromagnetic field, and $L(\tau_N) = (D\tau_N)^{1/2}$ is the distance over which

coherence is maintained (the fluctuating fields must be uniform over this distance). Nyquist's theorem [Reif, 1965] requires that for a given sample resistance, R, and temperature, T,

$$\langle V^2 \rangle = \frac{2}{\pi} k_B T R \tau_N^{-1} \quad , \tag{II-51}$$

so that

$$\langle E^2 \rangle = \frac{2k_B T R}{\pi L^2 \tau_N} \tag{II-52a}$$

$$\propto \frac{k_B T \rho}{L^d \tau_N} = \frac{k_B T \rho}{(D\tau)^{d/2} \tau_N}, \tag{II-52b}$$

with ρ the resistivity and d the sample dimensionality (since $R = \rho/L^{d-2}$). Thus,

$$\langle (\Delta\phi)^2 \rangle = \frac{e^2 \rho k_B T \tau_N^{2-d/2}}{\hbar^2 D^{d/2-1}} \quad . \tag{II-53}$$

Phase coherence is lost when $\langle (\Delta\phi)^2 \rangle \sim 1$. Therefore, from Eq. (II-53), the rate at which phase breaking occurs due to Nyquist noise is

$$\tau_N^{-1} \sim \left[\frac{e^2 k_B T \rho D^{1-d/2}}{\hbar^2} \right]^{2/(4-d)} \quad . \tag{II-54}$$

The precise quantitative prediction for this rate is [Altshuler et al., 1982b]

$$\tau_N^{-1} = \frac{1}{2\pi} \frac{R_\square}{\hbar/e^2} \frac{k_B T}{\hbar} \ln \left[\frac{\pi\hbar/e^2}{R_\square} \right] \tag{II-55}$$

for 2D systems, and

$$\tau_N^{-1} = \left[\frac{R_\square}{\hbar/e^2} \frac{k_B}{\hbar} (D/2)^{1/2} \right]^{2/3} \left[\frac{T}{W} \right]^{2/3} \qquad \text{(II-56)}$$

for 1D systems.

When considering the phase breaking rate for a given sample, contributions from all relevant mechanisms must be taken into account (see Sec. II.D). However, if the relative magnitudes of the rates are widely different, then, of course, the largest rate will be dominant. Altshuler et al. [1982b] demonstrated that with respect to electron-electron scattering, the relative contributions of the energy relaxation mechanism (strongly inelastic processes), τ_E^{-1}, and the Nyquist mechanism (quasielastic processes), τ_N^{-1}, will depend on the sample dimensionality. In three dimensions, the inelastic rate dominates the Nyquist rate. In 2D, τ_E^{-1} and τ_N^{-1} have the same temperature dependence and similar magnitudes, as seen from Eqs. (II-40), (II-41) and (II-55), and are therefore difficult to distinguish. In 1D systems, the quasielastic rate is predicted to be greater than the energy relaxation rate, so that $\tau_{ee}^{-1} \sim \tau_N^{-1}$. It is precisely this prediction which we test in the experiments described in Chap. V.

II.D.2. Electron-Phonon Scattering

While electron-electron scattering is usually the dominant phase breaking mechanism at the lowest temperatures ($T \lesssim 5K$), for most experimental systems it is electron-phonon scattering which determines the upper limit on the temperature at which quantum interference effects can be observed. As we shall see, the electron-

phonon scattering rate increases rapidly with increasing temperature. This shortens the range over which phase coherence is maintained and reduces the overall magnitude of the interference effects.

As is the case in electron-electron scattering, the degree of disorder in a sample can affect the scattering of electrons by lattice vibrations. Thus, we must consider two regimes of behavior: the clean limit, where impurities play no essential role, and the dirty limit, where the disorder can alter the nature of electron-phonon scattering. The demarcation between these two limits lies at $q_p \ell \sim 1$, where q_p is the characteristic phonon wavevector, $q_p = 4k_BT/(v_s\hbar)$, with v_s the velocity of sound [Bergmann, 1982]. For most of the samples studied in this work, $q_p^{-1} \sim 50$ Å at 5 K, while $\ell \sim 100$ Å, so they are marginally in the clean regime.

Clean Limit ($q_p \ell >> 1$)

The basic result for the electron-phonon scattering rate in pure metals can be obtained from simple considerations [Ashcroft and Mermin, 1976]. At temperatures far below the Debye temperature, only phonons with energy $\hbar\omega \lesssim k_BT$ can interact with an electron. This is due to the availability of electron states around the Fermi surface. In this regime, ω is of order of v_sq, where v_s is the velocity of sound and q is the phonon wavevector, which must then be on the order of $k_BT/\hbar v_s$ or less. Thus, the number of phonons that can participate in interactions with electrons at low temperatures goes as T^2. In addition, the square of the electron-phonon coupling constant is proportional to q, which, as mentioned above, is of order $k_BT/\hbar v_s$. This, combined with the T^2 dependence of the number of phonons available for scattering, yields a T^3 dependence for the scattering rate at $T << \theta_D$.

In order to facilitate the precise calculation of the electron-phonon scattering rate, Keck and Schmid [1976] found a useful connection between τ_{ep}^{-1} and the Eliashberg (spectral) function $\alpha^2F(\omega)$, which gives the transition probability of an electron from one energy state to another accompanied by the emission or absorption of a phonon with energy ω. They found

$$\tau_{ep}^{-1} = 4\pi \int d\omega \frac{\alpha^2F(\omega)}{\sinh(\hbar\omega/k_BT)} . \qquad \text{(II-57)}$$

It is important to note that this relationship holds for both pure and disordered metals, so that τ_{ep}^{-1} is determined essentially by the behavior of the Eliashberg function. Simple models for the Eliashberg function have $\alpha^2f(\omega)$ proportional to ω^2 at low frequencies [Lawrence and Meador, 1978; Kaplan et al., 1976]. Using this model, Kaplan et al. [1976] found $\tau_{ep}^{-1} \simeq 1.6 \times 10^7\ T^3\ sec^{-1}$ for aluminum. The T^3 dependence is a result of the ω^2 behavior of $\alpha^2F(\omega)$. More detailed calculations at specific Fermi surface sites of aluminum [Lawrence and Meador, 1978] yield an average value of

$$\tau_{ep}^{-1} = 0.91 \times 10^7\ T^3\ sec^{-1}. \qquad \text{(II-58)}$$

Experiments on single crystal samples [Doezema and Wegehaupt, 1975; Wegehaupt and Doezema; Doezema and Koch, 1975] confirm the $\tau_{ep}^{-1}(\vec{k})$ behavior predicted by Lawrence and Meador. In light of this, we will use Eq.(II-58) for comparison to the rates measured in the polycrystalline samples in this work.

II.D.2b. Dirty Limit ($q_p \ell << 1$)

In the presence of disorder, the electron-phonon interaction is modified. Restrictions due to momentum conservation are relaxed, as an electron undergoes many collisions with impurities between electron-phonon scattering events. Recall from Sec. II.D.2a that it is electron momentum conservation which restricts the allowed q values for phonons emitted or absorbed by an electron [Ashcroft and Mermin, 1976]. The result is a shift of the phonon spectrum to lower energies as the lattice is loosened by the presence of impurities and an increase in the electron-phonon interaction strength [Schmid, 1973]. In addition, there is a reduction of the coupling of electrons to longitudinal phonons and an increased coupling to transverse phonons as more non-Umklapp scattering processes are allowed (collision drag) [Keck and Schmid, 1976]. The ultimate effect on the electron-phonon scattering rate is a matter of controversy. Keck and Schmid [1976] claim that in the presence of impurities, the Eliashberg function takes the form $\alpha^2F(\omega) \propto \omega^3\ell$. This leads to a scattering rate $\tau_{ep}^{-1} \sim R_\square T^4$. In a pair of different calculations, Bergmann [1971] and Takayama [1973] found $\alpha^2F(\omega) \propto \omega/\ell$, so that $\tau_{ep}^{-1} \sim R_\square T^2$.

It should be noted that these dirty limit results may not be applicable to aluminum, no matter how dirty. Lawrence and Meador [1978] found that even in the case of clean aluminum, scattering by longitudinal phonons accounts for only about 18% of the total rate. Thus, the aforementioned increased coupling of electrons to the transverse modes in dirty samples may have very little effect in changing τ_{ep}^{-1} in aluminum. Certainly, it is clear that the above predictions for nearly-free-electron Fermi surfaces may not be relevant for Al.

The characteristic length scale associated with electron-phonon scattering is the most probable phonon wavelength, $\lambda_p = 2\pi/q_p$ [Bergmann, 1982]. If the sample dimensions are less than λ_p, then the electron-phonon scattering is of reduced dimensionality. The result is a reduction in the scattering rate by a factor of $\omega \simeq k_BT$ for each dimension less than λ_p [Thouless, 1977]. This yields

$$\tau_{ep}^{-1} \propto T^d , \qquad \text{(II-59)}$$

where d is the sample dimensionality. This result should hold in both the clean and dirty limits, however in the dirty limit, it is possible that the dimensional length scale is ℓ instead of λ_p, as phonons with wavelengths longer than ℓ contribute only a very small amount to the scattering of electrons [Ziman, 1960]. Above ~ 5 K, where electron-phonon scattering is the dominant mechanism for the samples studied in this work, the electron-phonon interaction is three-dimensional, since $\lambda_p \simeq \frac{365}{T}$Å is less than any of the sample dimensions. In fact, it would be difficult to observe one- and two-dimensional electron-phonon scattering in the types of samples studied here because of the shortness of λ_p and the fact that there is good thermal matching between the sample and the substrate [Kaplan, 1979], which allows for the participation of phonons with wavelengths greater than the sample thickness.

The preceding discussion has concentrated on quasiparticle energy relaxation rate due to the (large energy) inelastic scattering of electrons by phonons. As we have seen in the case of electron-electron scattering, quasielastic interactions may play an important role in the destruction of phase coherence. The question of quasielastic electron-phonon scattering was investigated by Schmid [1985] and Rammer and Schmid [1986]. They found that the quasielastic scattering by phonons

is negligible, and so the electron-phonon component of the phase breaking rate is determined only by strongly inelastic scattering.

Electron-Fluctuation Scattering

There exists an additional scattering mechanism in superconducting samples which can lead to destruction of phase coherence. At temperatures just slightly above T_c, quasiparticles of nearly equal but opposite momentum and spin may condense into a superconducting state [Patton, 1971; Keller and Korenman, 1972]. This mechanism clearly limits the quasiparticle lifetime and so destroys the phase coherence necessary for quantum interference.

Estimates of the phase breaking rate due to electron-fluctuation scattering, τ_{ef}^{-1}, have been made for 2D films [Brenig et al., 1985]. τ_{ef}^{-1} depends in a complex way on the applied magnetic field, so its extraction from magnetoresistance data is nontrivial. However, it does fall off rapidly as the temperature is raised above the superconducting transition temperature: $\tau_{ef}^{-1} \propto 1/\ln(T/T_c)$, so that this mechanism is important only very close to T_c (i.e., where $\ln(T/T_c) << 1$). As most of the experimental results reported in this work are not within this temperature range, this mechanism does not appear to play an important role for the interpretion of the data. As we shall see, only in the narrowest Al wires is there some indication of electron-fluctuation scattering. Brenig et al. [1985] derived an expression for τ_{ef}^{-1} for two-dimensional systems. Unfortunately, no theoretical prediction is available for 1D systems ($W < \xi$), which would be appropriate for those wires.

II.D.4. Two-Level Scattering

Results of the earliest 1D localization experiments [Giordano et al., 1979; Chaudhari and Habermeier, 1980] seemed to indicate that $\tau_\phi^{-1} \propto T$. No known scattering mechanism at that time could account for the measured rates other than the inelastic rate proposed for two-level systems in amorphous materials [Black et al., 1979]. It was felt that perhaps the highly disordered metal samples of those early studies could form two-level systems. Scattering in two-level systems could provide a plausible explanation for the temperature dependence of the rates measured in those studies, but not for the magnitude of the rates and their dependence on sample resistivity [Stone, 1983]. As we will discuss in Chap. VI, the rates measured in those early experiments are not reliable, so that it is not necessary to invoke two-level scattering as an explanation for the scattering rates. In any case, the samples in the present work are only moderately disordered, and it is highly unlikely that this mechanism is relevant to these systems.

III. Fabrication of Ultrasmall Structures for Quantum Transport Studies

III.A. Preliminary Considerations

III.A.1. Materials

The samples studied in this work were composed of either Al or Ag. Before discussing the techniques used to fabricate samples, it is worthwhile to devote some attention to the considerations which influenced the choice of these materials. It should be noted that at the time these experiments were embarked upon, earlier experiments intended to test the 1D localization theory yielded apparently ambiguous results (see Sec. VI.A). The materials studied in those early experiments were Au-Pd [Giordano et al., 1979], W-Re [Chaudhari and Habermeier, 1980] and Cu and Ni [White et al., 1982]. It was felt that perhaps these materials were somehow not ideally suited for the clear observation of localization effects and electron scattering mechanisms (which were also not well-understood at that time).

There are several factors which make Al, which was used for the bulk of the experiments in this work, an attractive material for quantum interference studies. Al is a well-behaved and well-understood thin film material which has been the subject of numerous experimental studies over several decades. Results of non-quantum interference experiments (mainly nonequilibrium superconductivity measurements) on moderately clean Al films ($R_\square \lesssim 1\ \Omega$) seemed to indicate that relatively long inelastic scattering lengths could be obtained. This meant that the magnitude of the quantum interference effects would be large [see Eq. (II-23)]. In addition, with the longer inelastic scattering lengths in Al the criterion for one-dimensionality with

respect to localization ($W < \ell_\phi$) could be met without pushing fabrication techniques to their limits. The nonequilibrium superconductivity experiments also provided data against which the results of our work could be compared. Furthermore, while the role played by spin-orbit scattering was not well-understood when these experiments were first undertaken, it was known that it did have some effect on quantum interference behavior. Al was believed to have a relatively long spin-orbit scattering length.

The fact that Al is a superconductor does place a lower limit on the temperature range over which normal metal effects can be observed, and superconducting fluctuations do become quite large even a few degrees above T_c. However, as explained in Sec. II.C.3, the Maki-Thompson fluctuations actually mimic the weak localization effect, so they can be thought of as an amplification of quantum coherence. As we shall see in the following section, the superconducting properties of Al can also be used to determine some of the important material characteristics of the samples. Finally, from a strictly practical point of view, Al can be deposited by thermal evaporation with reproducible properties which can be easily controlled by the deposition conditions. This is important for a clear comparison of different samples.

The measurements on Ag samples supplemented in a way the results obtained in Al. However, the choice of Ag was motivated by somewhat different concerns than those mentioned in the previous paragraphs. It was decided to study Ag samples only after preliminary results on Al rings had already been obtained. Those Al rings showed clear oscillations with a period of h/2e, but no sign of h/e oscillations. It was felt that the magnitude of the superconducting fluctuations in Al might make it

difficult to observe the h/e oscillations. Thus, a normal metal was chosen for study. Results of experiments on a Au ring by Webb et al. [1985] showed h/e oscillations but no h/2e oscillations. We sought to find both types of oscillations in the same ring. Brief measurements on 2D films of Cu and Mg indicated that these materials were not well-suited for the studies we had chosen. The Cu films showed a high degree of magnetic scattering, while the Mg samples indicated that it would be difficult to pattern small samples using room temperature deposited films. Ag, on the other hand, did show signs that it would be an appropriate material. Our experimental results ultimately bore this out.

III.A.2. Fabrication Requirements

As part of the rapid growth that has taken place in the field of integrated circuit manufacture in the past two decades, microfabrication technology has continued to develop new techniques to define structures at increasingly smaller dimensions. Many of these techniques have found their way into the manufacturing process (in fact, at the present time, new devices are being manufactured with minimum feature sizes below 1μm, and current trends are to shrink to even smaller dimensions in the near future). Other techniques are appropriate only for small scale laboratory applications. Nevertheless, for the purposes of preparing samples for studies of quantum transport phenomena, some techniques show advantages over others or may be better suited to the task at hand. Since a significant capital expense may be called for, and certainly a large investment of time and effort are involved in sample fabrication, it is critical that the particular requirements of the experiment be examined. As we shall see, the conditions for one-dimensionality with respect to the characteristic length scales involved in electron interference

phenomena are quite stringent. It should be noted that when this work was first undertaken, not all these length scales were known or clearly understood, so that in some cases certain suppositions had to be made which could be tested only as the experimental results became available.

The length scale which determines the sample dimensionality with respect to the weak localization effect is the electron phase coherence length, ℓ_ϕ. In order for a sample to be one-dimensional with respect to localization, its cross-sectional dimensions (i.e., its width and thickness for a sample of rectangular cross-section) must be less than ℓ_ϕ. As noted previously, for the materials (Al and Ag) and sample resistances ($R_\square \simeq 1\ \Omega$) studied in this work, ℓ_ϕ is $\simeq 1\ \mu$m or longer at 1 K. (Our current He^4 experimental apparatus sets a lower limit of 1.2 K on the temperature range over which measurements can extend.) However, ℓ_ϕ is temperature dependent, and it becomes significantly shorter as the temperature is increased. At 20 K, ℓ_ϕ is already $\simeq 0.1\ \mu$m, so that if a sample is to be one-dimensional with respect to localization over a reasonable range of temperatures, the sample width cannot be more than a few tenths of a micron.

In order to observe Aharonov-Bohm oscillations in metal ring structures, the diameter of the ring cannot be much more than ℓ_ϕ, otherwise the oscillations would be severely damped (see Sec. II.C.2). This means ring diameters of order 1 μm. In addition, the width of the wires comprising the arms of the ring must be significantly less than the ring diameter. This is to separate the field scales for observing A-B oscillations and universal conduction fluctuations. If the area enclosed by the ring (i.e., the hole inside the ring) and the area of the ring annulus are similar, then conductance fluctuations will make the clear observation of the

oscillations difficult [Stone, 1985; Webb et al., 1985]. This requirement imposes very strict demands on the fabrication process.

In the case of a real normal metal, spin-orbit effects can be significant, as already discussed in Chapter II. (In MOS systems, spin-orbit scattering appears to be minimal [Wheeler et al., 1982].) Spin-orbit scattering causes the localization magnetoresistance to split into two portions, one of which is sensitive to spin-orbit scattering ("triplet" term) and the other of which is sensitive only to the usual phase breaking mechanisms ("singlet" term), as described in Secs. II.A.3 and II.C.1. The dimensional length scale for the singlet term is ℓ_ϕ, as discussed above. The length scale for the triplet term is ℓ_2, which is a combination of the phase coherence length and the spin-orbit scattering length, as in Eq. (II-26). When ℓ_ϕ and ℓ_{so} are very different, ℓ_2 will correspond to the shorter of the two lengths. Thus, at the lowest temperatures $\ell_2 \propto \ell_{so}$. In Al and Ag, ℓ_{so} has been found to be $\approx$0.5 μm, so that if the triplet term is to have the one-dimensional form, the sample width must also be less than $\ell_2 \propto \ell_{so}$. Otherwise, the localization magnetoresistance may be of "mixed dimensionality" [Eq. (II-28)], where the singlet and triplet terms have different forms. It should be pointed out that ℓ_{so} is relatively long in Al and Ag ($\approx$0.5 μm) as compared to other materials, where ℓ_{so} has been found to be as short as a few hundred Angstroms or less. Thus, it should be possible to observe the fully one-dimensional localization behavior without stretching the limits of our microfabrication technology.

The length scale which determines sample dimensionality with respect to electron-electron interactions is the electron thermal diffusion length, $\ell_T = (\hbar D/k_B T)^{1/2}$. For relatively clean Al and Ag samples ($R_\square \propto 1\ \Omega$), $\ell_T \propto 0.1$ - $0.2\ \mu$m

at low temperatures. A sample a few tenth microns wide, which is one-dimensional with respect to localization, would show a two-dimensional electron-electron scattering rate. If one wishes to observe a one-dimensional electron-electron process, extremely narrow wires are required: $W < 0.1\ \mu m$. Although ℓ_T is not a rapidly varying function of temperature, for samples which are not much narrower than 0.1 μm one cannot hope to observe the distinctive temperature dependence of the scattering rate, Eq. (II-56), over a reasonable range of temperatures. It should also be noted that the one-dimensional interaction effect [Altshuler et al., 1980] can be observed only when $W < \ell_T$.

The considerations in the previous discussion indicate that in order to observe quantum interference effects in narrow metallic wires, one must employ a fabrication technique with a resolution of $\sim 0.1\ \mu m$ or better. In addition to this need for high resolution, there are a number of other requirements which the fabrication technique must meet. These include reproducibility and controllability, so that samples of nearly the same properties can be obtained, and compatibility with "liftoff" processing (see below). This is because in the study of one-dimensional effects in narrow wires, it is desirable to have on hand a two-dimensional sample which has nearly the same macroscopic material and electrical characteristics. This is helpful in determining some of the sample parameters of the 1D samples (see in Sec. V.A) as well as setting a benchmark against which one may distinguish the 1D effects. Liftoff processing is also important because the sample and the electrical contact pads can be deposited in the same metallization step, which eliminates possible complications due to contact resistances. In addition, it may be desirable to study samples of similar geometry but which are composed of different materials. Certain materials may highlight (or suppress) some aspects of the quantum interference

effects by virtue of the particular properties of that material (superconductivity in the case of aluminum, or strong spin-orbit scattering in the case of Au-Pd, for example). Therefore, it is preferable to employ a fabrication technique which may readily be adapted to different materials.

III.A.3. Available Fabrication Techniques

A variety of methods are available which meet most of the requirements mentioned above. Here we will present a brief survey of those which offer the best applicability to quantum interference experiments. A detailed review of nanometer-scale lithographic techniques can be found in an article by Howard and Prober [1982].

Lithographic techniques which are capable of submicron resolution include conventional photolithography, electron-beam writing, x-ray printing, ion-beam lithography (both direct-write and masked shadow printing) and edge-defined lithography. The first four techniques, with the exception of direct-write ion beam lithography, involve the use of a resist. This is a thin layer of radiation-sensitive material, usually an organic polymer, whose chemical or structural properties are altered by the exposing radiation (electron, ion or photon beams). The resist coats an appropriate substrate and is exposed to the radiation according to the desired pattern. The resist is then developed in a solution which preferentially removes either the exposed regions of the resist (positive resist) or the unexposed regions (negative resist), leaving the substrate coated with a stencil of the desired pattern. Subsequent processing involves either etching the substrate in the open areas of the resist pattern or depositing a metal and "lifting-off" the metal which covers the

remaining resist by removing the resist in a solvent. These steps are shown schematically in Fig. III-1. Edge-defined lithography, on the other hand, utilizes some relief structure in the substrate itself to define the ultimate structure, whose lateral dimensions are determined by the out of plane features of the relief structure. Examples of this technique are shown in Fig. III-2.

Most of these techniques are suitable for the fabrication of ultrasmall structures for quantum transport experiments. However, each has limitations in terms of its usefulness for fabricating samples for quantum transport studies. In the case of optical lithography, a resolution of ~ 0.25 μm has been shown to be attainable by using projection lithography in a high grade optical microscope either by underdeveloping a rear-projected image [Feuer and Prober, 1981] or by controlled overetching an already deposited film [Wisnieff, 1987]. This resolution is sufficient for the observation of 1D localization effects, but it is not sufficient for studying electron scattering rates in metals or for observing Aharonov-Bohm oscillations. Reproducibility and linewidth control are also a problem at the smallest linewidths.

Although ion beam lithography is capable of the necessary resolution for all the desired structures, at the time this work began, ion beam mask technology was in the early stages of development, and a suitable method for mask fabrication was not available. This was not so in the case of x-ray lithography. X-ray lithography had been demonstrated to be viable on the laboratory scale already in the mid-1970's [Smith et al., 1973], and useful x-ray masks had been produced using a variety of materials [Shimkunas, 1984]. The major difficulty with x-ray lithography lies in the fact that it involves one-to-one printing of the mask pattern, so that if the resolution requirements are to be met, a suitable mask patterning technique must be

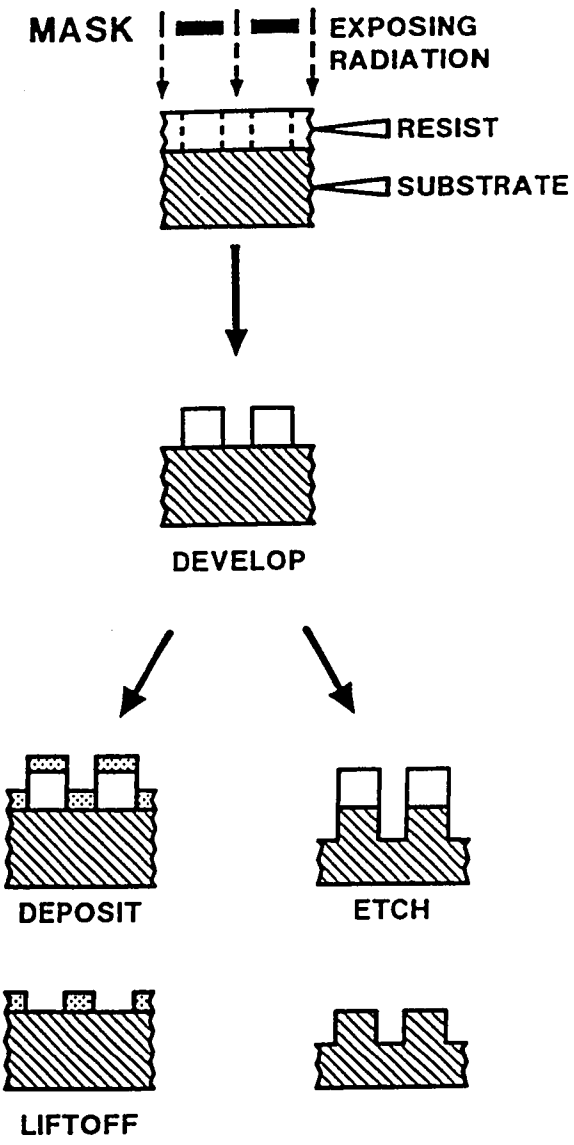

Fig. III-1. Basic lithographic fabrication sequence. Following development, the pattern is transferred either by liftoff or by etching the substrate. (From [Howard and Prober, 1982].)

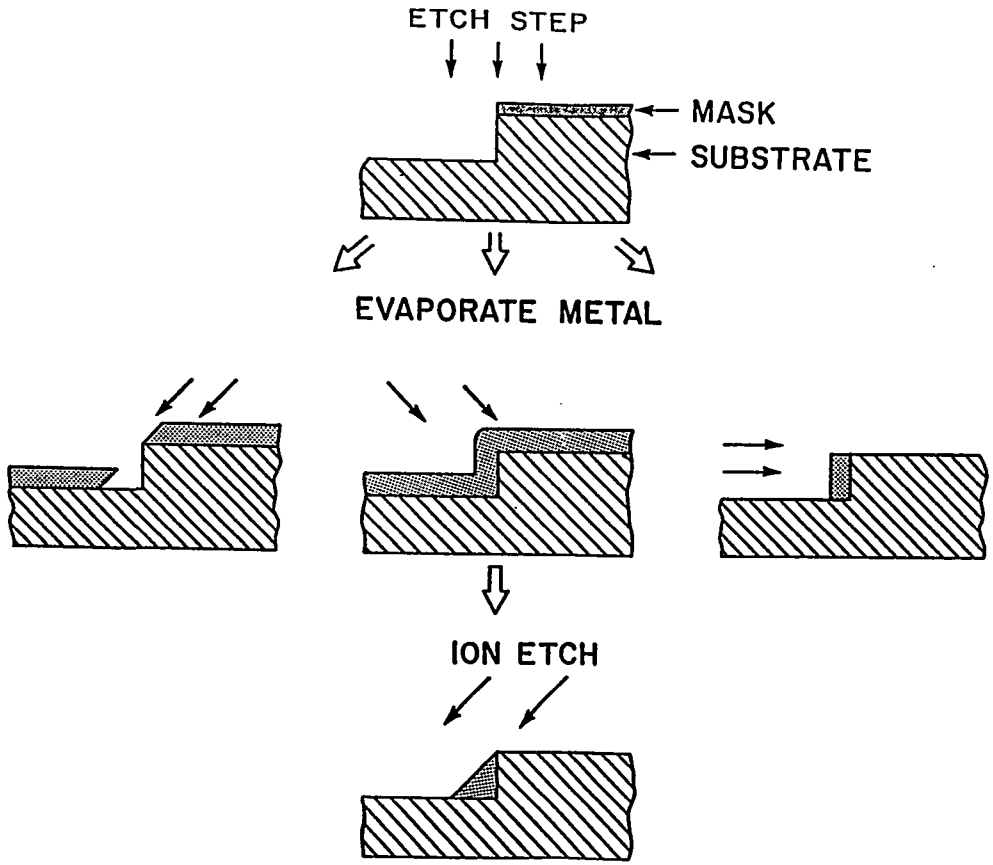

Fig. III-2. Edge-defined patterning techniques. A combination of directional etching and/or metallization is used to form a pattern near the edge of a step in the substrate. (From [Howard and Prober, 1982].)

employed. This is not an insurmountable problem and the issue of x-ray mask patterning will be addressed in Sec. III.B.2.

Electron-beam lithography is in principle extremely well-suited for sample fabrication for quantum interference experiments. There exist several types of electron-beam systems, some of which are custom built for the purpose of ultra-high resolution lithography and some with a resolution approaching 100 Å (see e.g., [Brodie and Muray, 1982; Rooks et al, 1987]. Perhaps the only limitation on a high resolution e-beam system, in terms of the requirements mentioned above, would be the small writing field usually necessary for achieving such high resolution. This limits the in-plane aspect ratio of the e-beam written sample (i.e., a 1D wire cannot be arbitrarily long) as well as the ability to produce in the same e-beam exposure samples with both small and large features, such as electrical contact pads. For as the present work, an electron-beam system was made operational as samples were already being produced by x-ray lithography. For certain samples, e-beam lithography presented some advantages over x-ray lithography, and in those cases, the samples were indeed produced by e-beam lithography, as will be discussed later in this chapter.

Samples for the earliest weak localization experiments [Giordano et al., 1979] were fabricated by a step-edge technique. This method, described in Fig. III-2, was shown to be capable of a resolution near 100 Å. Difficulties with this particular technique and others like it [Howard and Prober, 1982] lie in the fact that they may not be adaptable to a variety of sample materials and do not necessarily lend themselves to making low resistance contacts with all materials. (Contact pads cannot always be deposited in the same fabrication step as the sample itself.) In

addition, one cannot usually make 2D films with the same material properties as a sample fabricated by step-edge means (i.e., in the same metal deposition), particularly when etching is involved, as in Fig. III-2. Also, this technique is not readily adaptable to the fabrication of ring structures.

The fabrication techniques employed in the present study were x-ray lithography and electron-beam lithography. The following sections will be devoted to a description of the implementation of these techniques in this work.

III.B. X-Ray Lithography

X-ray lithography is similar in principle to conventional photolithography in that a material which is sensitive to x-ray radiation (x-ray resist) has its chemical properties altered upon exposure to x-ray radiation, so that it is either more or less soluble in a developer solution than it was prior to exposure. The major difference lies in the fact that the wavelength of the exposing x-ray radiation ($\lambda \sim 0.4 - 5$ nm) is considerably shorter than that used in conventional photolithography ($\lambda \sim 400$ nm). The pattern in the resist is formed by exposing it through an x-ray mask. The mask consists of an x-ray transparent material, the mask membrane, covered with a patterned x-ray absorbing material. Diffraction, which is the primary factor limiting the resolution of optical lithography to $\sim \lambda/2$, plays virtually no role in x-ray lithography because of the shortness of the wavelength of the exposing radiation. In addition, dust, which is a major cause of defects in optical lithography, is not a problem in x-ray lithography, as most common types of dust are transparent to x-rays.

The mechanism by which x-ray exposure is believed to operate [Spears and Smith, 1972] is as follows: x-ray photons are absorbed in the polymer resist, where they create photoelectrons. These secondary electrons alter the properties of the resist by either breaking molecular bonds or by crosslinking the polymer. The x-ray lithography process is pictured schematically in Fig. III-3.

X-ray lithography possesses several advantages over some of the other high resolution processes mentioned in Sec. III.A. Aside from being capable of producing structures with features as small as those produced by the highest resolution electron-beam systems [Flanders, 1981], x-ray lithography can achieve this resolution over relatively large areas - usually much larger than those achievable with most e-beam systems. In addition, one can expose simultaneously both ultrasmall and macroscopically large features in the same x-ray exposure. Replication of mask patterns is relatively simple once an x-ray mask already exists; all that must be done is expose and develop the pattern on the substrate. Alignment is not necessary for simple patterns. It is also possible to construct a workable, laboratory-grade x-ray lithography exposure system using relatively simple equipment that lacks the delicacy of electron and ion beam columns as well as their sensitivity to mechanical vibrations. Another possible advantage of x-ray lithography which has yet to be explored is one that could be important in MOS device work. It is known (see, e.g., [Ma, 1975]) that oxide damage is caused by exposure of devices to highly energetic electron beams. Because of the strong attenuation of soft x-rays in most materials, it is possible that higher mobilities may be attainable in these devices if they are patterned by x-ray lithography [Ma, private communication].

Of course, there are some difficulties which must be overcome in implementing

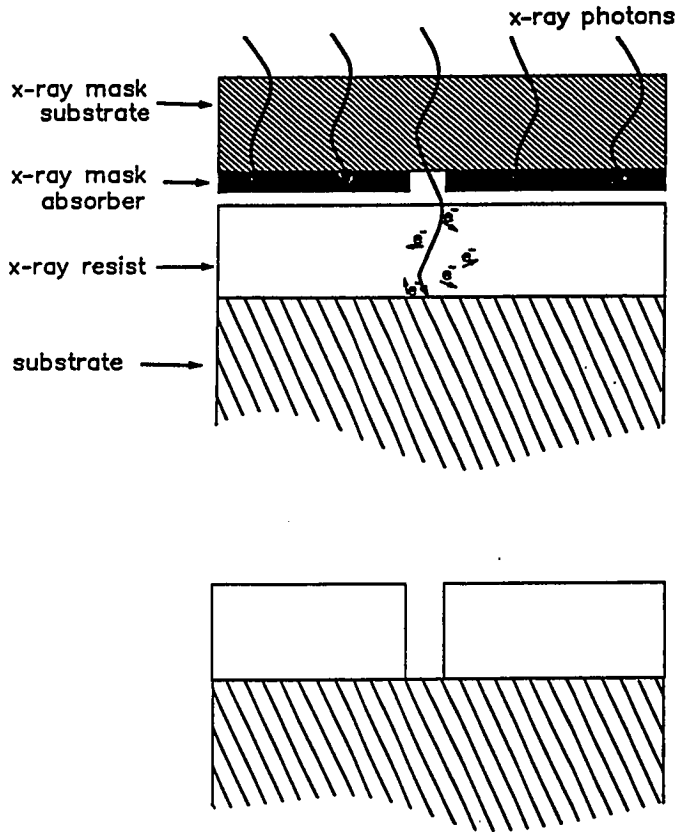

Fig. III-3. X-ray lithography process. X-ray photons are absorbed in the resist, where they emit secondary electrons. These electrons break polymer bonds in the resist, making it either more or less soluble in a developer solution. Following development, the resist is processed as in conventional lithographic processes (Fig. III-1).

an x-ray lithography system as well. Of relatively minor difficulty is the fact that the x-ray source, which will be discussed in Sec. III.B.1, usually requires a high vacuum environment for operation. More important is the fact that an x-ray mask is needed. In order for parts of the mask to be transparent to x-rays, the mask itself must be formed of a thin membrane, as almost all substances are strong absorbers of soft x-rays. This membrane must be both thin enough to transmit sufficient x-ray flux for a proper exposure, yet robust enough to withstand reasonable handling over the course of at least several exposures. Also, as x-ray lithography is a one-to-one printing process, some method is necessary for patterning the mask itself with features as small as are ultimately desired for the final samples. These issues will be addressed below in Section III.B.2, which is devoted to a discussion of x-ray masks.

The ultimate resolution of an x-ray lithography system depends on three factors: 1. Diffraction and geometrical distortion; 2. the pathlength of secondary photoelectrons in the resist; 3. the structural integrity of the resist. These factors are governed by the x-ray source, mask and resist, which will be described in the following discussion.

III.B.1. The X-Ray Source

There are several possible sources of soft x-rays for lithography applications. These include electron bombardment sources, both stationary and rotating anode types, where the soft x-rays are produced by the decay of atomic states excited by energetic electrons, laser generated plasmas [Nagel, 1975] and synchrotron radiation sources [Grobman, 1980; Wilson, 1986]. As plasma sources have yet to demonstrate

practical viability in terms of a microlithographic system, the only source which can be practically implemented in a laboratory environment is the electron bombardment source. The stationary anode source is less complex than the rotating anode, but it is capable of producing only a fraction of the total x-ray flux produced in the rotating anode system.

X-rays are produced when atoms in a metal decay from excited states which are generated by bombarding the target metal with energetic electrons. If the energy of the incident electrons, E_i, is greater than the excitation energy of the characteristic line radiation of the atoms in the target material, E_c, then the emitted radiation will consist of this line radiation plus some bremsstrahlung (continuum radiation). The power in the line radiation is proportional to $E_i - E_c$. It is possible to "tune" the radiation to a desired wavelength by choosing the energy for the incident electrons which is just below the excitation energy of the line directly above the desired line. Thus, for example, if E_c = 0.95 KeV for the L_{II} line of copper and E_c = 8.9 KeV for the K line, then one would use an electron accelerating voltage of < 8.9 KV.

The choice of the target material and wavelength depend on several factors. Diffraction and geometrical distortion effects, which may be caused by a finite gap between the mask and the resist (or by the finite thickness of the mask absorber itself) are smallest at short wavelengths. Short wavelengths are also desirable since transmission of the mask substrate is greatest (see Fig. III-6). However, the mask absorber is then less efficient. Longer wavelengths are also indicated by the fact that the pathlength of secondary electrons generated by the absorption of x-ray photons in the resist is <u>longer</u> for <u>shorter</u> wavelength radiation [Spears & Smith,

1972]. This, in fact, probably sets the lower limit on the ultimate achievable resolution of x-ray lithography for a given resist. Fig. III-4, from [Flanders, 1977] shows the range of photoelectrons in PMMA, the most commonly used x-ray resist. As can be seen from the figure, this range increases with increasing photon energy. In order to achieve resolution better than 0.1 μm, the copper L_γ line, with λ = 13.3 Å (range ~ 200 Å), and the carbon K_α line, with λ = 44.7 Å (range ~ 50 Å), are the most appropriate sources. The K_α line of aluminum, with λ = 8.3 Å (range ~ 400 Å), would be marginally acceptable.

Of great importance as well, is the ability of the target material to dissipate heat. The efficiency of electron bombardment sources in terms of emitted x-ray power versus electron beam power is extremely poor: ~ 10^{-4}. The vast majority of the energy absorbed by the target is converted into heat. Therefore, it is important that the target material have a high thermal conductivity. It is for this reason that a material such as silicon, which has a K_α line at λ = 7.1 Å, would not make a good target.

The x-ray source used in this work is shown schematically in Fig. III-5. The electron gun is a Vacuum Generators model EG-2 electron-beam evaporation unit[1] operated at sufficiently low power so as not to evaporate the target material. Electrons are thermally generated by a tungsten filament ring cathode kept at a high negative potential and are accelerated into a ~ 1 mm diameter spot at the center of the water cooled target (the anode), which is at ground potential. Focusing is done electrostatically by maintaining the shield and screen (see Fig. III-5) at the cathode

[1]Vacuum Generators Ltd., Sussex, England.

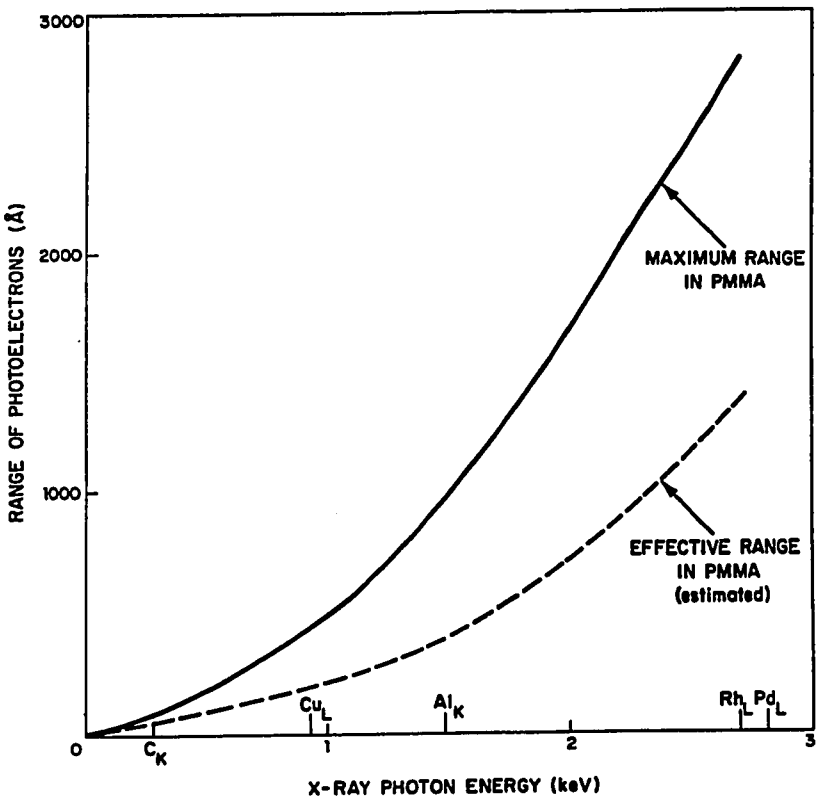

Fig. III-4. Range of secondary photoelectrons in PMMA as a function of x-ray photon energy. (From [Flanders, 1977].)

potential. The anode consists of a polished 1 mm thick disc of either OFHC copper or DFP-2 grade (high purity, high thermal conductivity) Poco graphite[1] squeezed down onto the copper hearth by a copper ring, with thermal contact aided by a thin layer (~ 200 μm) of indium. Alternatively, for exposures with the copper source, the bare copper hearth was used as the target. The maximum power into the target is set by the thermal conductivity of the entire target assembly. In practice, this was determined by increasing the power until the target began to evaporate. Typical operating power was ~ 350 W for the bare copper hearth and ~ 250 W for the carbon disc assembly. This was sufficiently below the maximum power so as to allow for transients in the electron gun power supply[2] and in the cooling water supply. Affixed to the top of the electron gun is an electron deflector. The purpose of the deflector is to ensure that electrons which may backscatter from the anode do not reach the x-ray resist, where they can cause spurious exposure [Flanders, 1977].

Soft x-rays are severely attenuated by virtually all substances, including air (the absorption length in air is ~ 1 mm), so that the entire exposure system must be enclosed in vacuum. The vacuum chamber is stainless steel pumped by a Varian VHS-4 4-inch diffusion pump[3] equipped with a 6-inch cold trap and a cold cap to reduce backstreaming of pump oil. The diffusion pump gate valve is electropneumatically controlled[4] and interlocked to a vacuum ionization gauge in the chamber. The electron gun power supply is similarly interlocked to the ionization

---

[1]Poco Graphite Inc., Decatur, Texas

[2]Balzers, Hudson, New Hampshire. The power supply was adapted to operate the Vacuum Generators electron gun.

[3]Varian Assoc., Palo Alto, California.

[4]Airco Temescal, Berkeley, California.

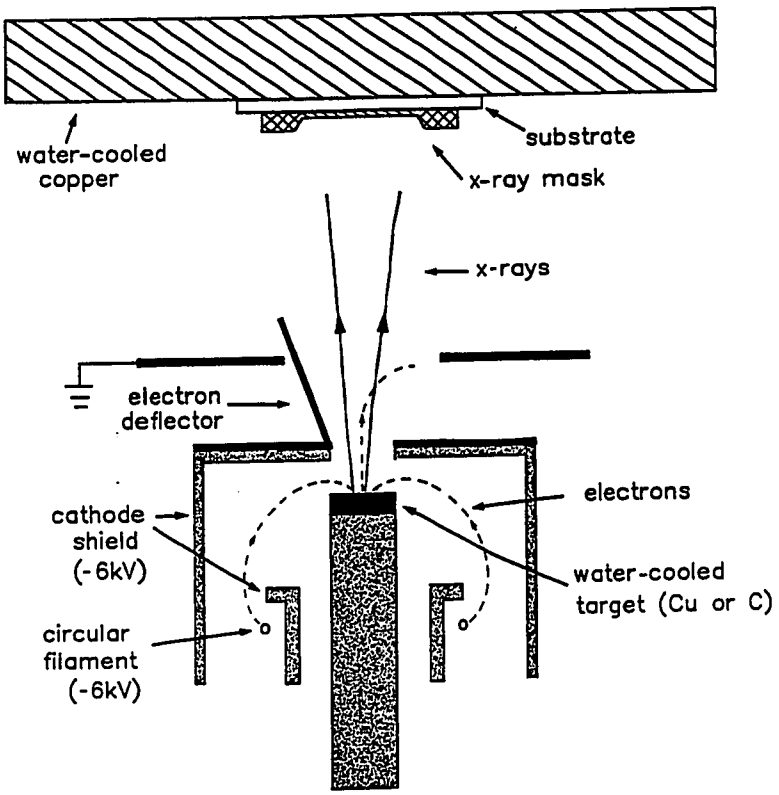

Fig. III-5. Schematic diagram of the x-ray exposure system.

gauge controller to prevent operation of the gun at pressures above ~ 1 x 10^{-6} torr, which could potentially "poison" the tungsten filament and suppress the electron emission [Morecroft, 1933]. Such "poisoning" can also be avoided by running the filament at high current for a short time prior to exposure. Typical base pressure for the system is ~ 5 x 10^{-8} torr after ~ 8 hours with a 1 hour bakeout. A bakeout could usually be done by simply operating the electron gun at high filament current and zero accelerating voltage. Typical operating pressure during an x-ray exposure is ~ 1 - 5 x 10^{-7} torr with the vacuum chamber walls air cooled.

III.B.2. Fabrication of X-Ray Masks

Mask fabrication has always been considered the most problematic aspect of x-ray lithography. Difficulties range from choosing the mask membrane material to avoiding damage to the mask during x-ray exposure. While many of these challenges have yet to be dealt with successfully in terms of an x-ray mask scheme that can be integrated into an industrial-grade system, sufficient progress has been made so that useful x-ray masks can be fabricated and replicated in a small-scale laboratory environment [Shimkunas, 1984]. It is reasonable to anticipate that this success will carry over to the manufacturing arena [Wilson, 1986].

The main components of the x-ray mask fabrication process are: (1) the mask membrane, (2) mask patterning and (3) implementation in the exposure system. These issues are actually interdependent. For example, the choice of the mask membrane material is determined by its ability to be readily patterned and by the fact that it must have a high contrast with the patterned x-ray absorber, which is usually a heavy element, such as gold or tungsten. Other requirements on the membrane

material include the ability to be applied in thin film form (~ 1 μm), structural and thermal stability to minimize distortion, freedom from defects containing heavy metal particles, and a smooth surface, for the case of contact printing.

Several different techniques have been developed for fabricating x-ray masks using a variety of membrane materials [Shimkunas, 1984], with the current best choices being hydrogen-rich boron nitride [Dana and Maldonado, 1986] and silicon nitride [Ono and Ozawa, 1984]. Most of these membrane materials, however, are not suitable for use with the Cu_L and C_K x-ray lines, which offer the highest resolution (see Sec. III.B.1, above), because of their high attenuation at these wavelengths. Fig. III-6 shows the absorption coefficient of several x-ray mask materials as a function of wavelength. It can be seen from the figure that at the carbon C_K line only organic materials, which have an absorption edge at 45.4 Å, transmit sufficiently well to provide good contrast with a gold absorber.

Flanders and Smith [1978] found polymide to be a nearly ideal material for use as an x-ray mask membrane. It can be readily prepared by spinning onto a substrate (which is subsequently removed) in smooth layers with thicknesses ranging from a few tenth-microns to several hundred microns. It has a low mass absorption coefficient [Bassous et al., 1976], can withstand high temperatures and shows low distortion [Flanders and Smith, 1978]. The mask membrane preparation scheme used in this work follows closely the original work of Flanders [1978] and Hawryluk [1981].

The process used in this work for fabricating x-ray masks is shown schematically in Fig. III-7. Complete details of the process are given in Appendix A.

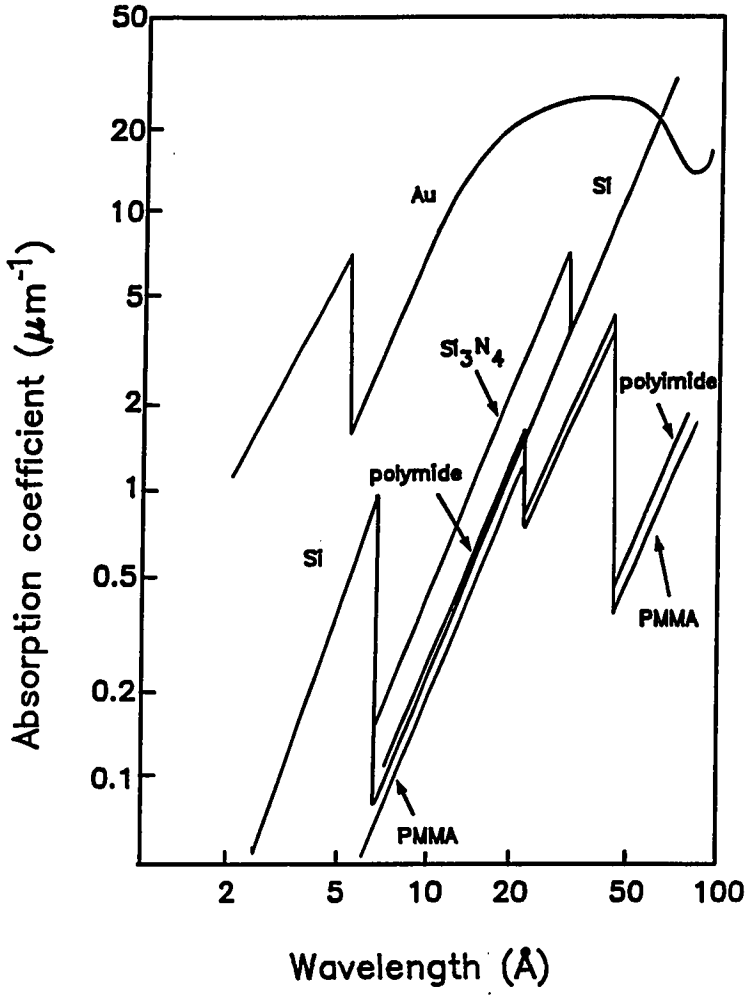

Fig. III-6. Absorption coefficient as a function of x-ray photon wavelength for several x-ray mask materials. (Data from [Spears and Smith, 1972].)

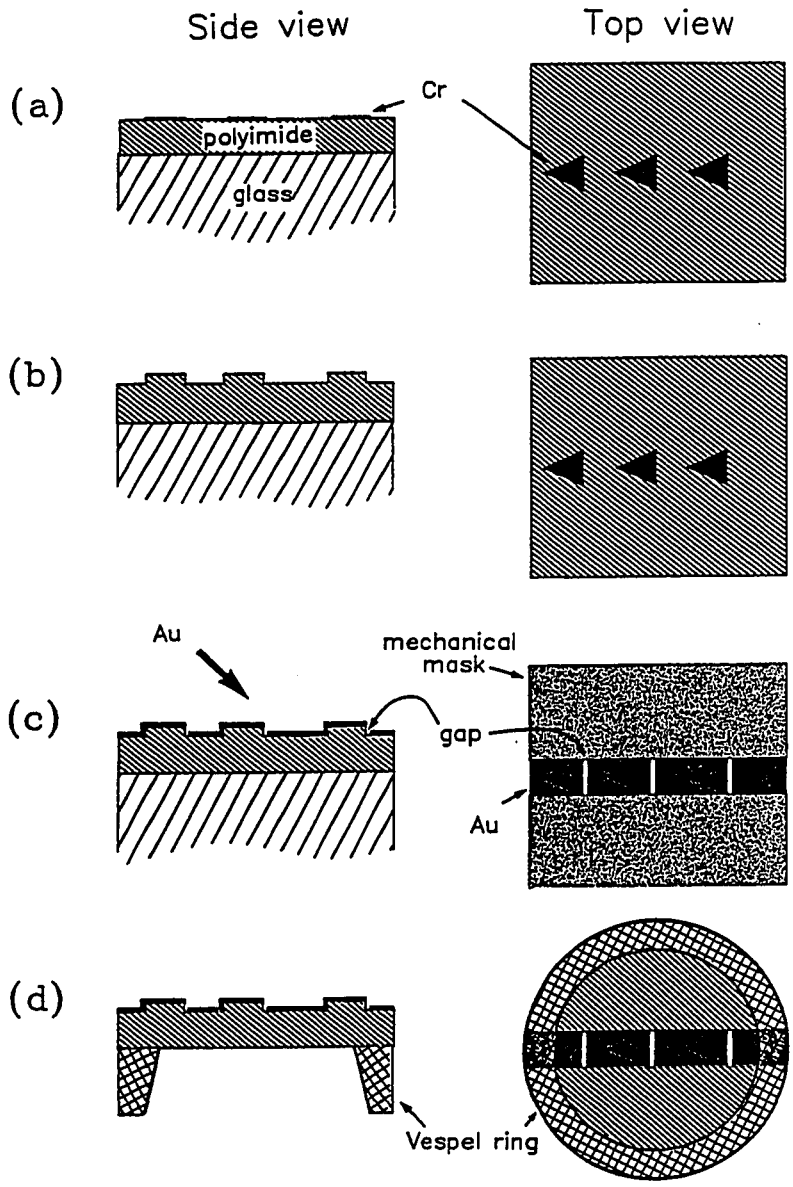

Fig. III-7. X-ray mask fabrication process. (a) Cr triangles are formed on the polyimide-coated substrate by conventional photolithography. (b) Reactive ion etching of the polyimide leaves steps ~ 2500 Å high beneath the Cr etch mask. (c) The gold x-ray absorber is deposited through a metal slot mask at an angle, leaving gaps at the bases of the triangles. (d) The glass substrate is removed from the polyimide film, which is then bonded to a Vespel ring.

First, an 18 mm x 18 mm glass cover slip[1] is thoroughly cleaned in acetone and isopropyl alcohol. The cover glass is then coated with a thin film of polyamic acid[2] using conventional spinning techniques. The polyamic acid is diluted in N-Methyl pyrollidone[3] prior to spinning. The film thickness is controlled by a combination of the ratio of polyamic acid to the diluent and the spin speed. Ratios of approximately 1:1 with spin speeds of ~ 3000 rpm for 120 seconds yield films about 1 μm thick (see Appendix A). After spinning, the polyamic acid film is converted to polyimide by baking it at 300 °C for 2 hours. The mask is then ready for patterning.

Since x-ray lithography is a one-to-one printing process, the x-ray mask must be patterned at the same size scale as ultimately desired for the final sample; there is no demagnification involved as is the case in optical projection lithography. The most straightforward method of patterning x-ray masks is by electron-beam lithography, which is commonly used in many x-ray mask facilities today for precisely this purpose. However, in the early stages of the present work, an e-beam writing facility was not available at Yale. Thus, a different method of mask patterning had to be devised.

The mask patterning scheme developed for this work was inspired in part by the step-edge fabrication technique of Prober et al. [1980] for making narrow wires. In the present case, the x-ray mask pattern for narrow wires is formed by depositing

---

[1]Corning Glass Works, Danville, Virginia.

[2]Product PI2550, E.I. DuPont deNemours Co., Wilmington, Delaware.

[3]KTI Chemicals, Sunnyvale, California.

the x-ray absorber at an oblique angle across the edge of a step which is formed in the polyimide mask membrane. The formation of the step involves optical photolithography and reactive ion etching and proceeds as follows: After the polyimide film is baked, a layer of AZ-1350B photoresist[1] (~ 5000 Å) is spun on and baked at 90 °C for 30 minutes. The photoresist is then exposed either by contact lithography or by projection lithography to form an image of a triangle in the resist. The contact exposures are done using a 100 Watt high pressure mercury vapor arc lamp. The contact mask is a chromium coated cover glass. The pattern in the chromium is a set of triangles ~ 500 μm on a side, originally formed by projecting the image of three razor blade edges in a Carl Zeiss photomicroscope.[2] The triangles are set in a row with the vertices opposite the triangle bases (which serve as the step edges) lying on a straight line (see Fig. III-7). This is helpful for alignment in a later stage of processing. Contact between the mask and the substrate is maintained by vacuum, and the exposure is done through a quartz window. Alternatively, the triangle images could be formed by projection lithography directly onto the polyimide-coated substrate. Again, the edges of the projection mask consist of three razor blade edges in a triangular configuration. Appendix A contains details of the procedures followed for both types of optical exposure. Ultimately, the projection method was preferred over contact lithography since the extra steps involved in the latter in transferring the pattern from the original razor blade mask resulted in slighty degraded final images. After the optical exposure, the resist is developed in AZ developer[3] using a standard developing procedure.

---

[1]Shipley Corp., Inc., Newton, Massachusetts.

[2]Carl Zeiss, Inc., New York, New York.

[3]Shipley Corp., Inc., Newton, Massachusetts.

Following the optical exposure, 200 Å of chromium are deposited by thermal evaporation in a Varian evaporation system[1] and lifted off by soaking in acetone with ultrasonic agitation. This leaves a pattern of chrome triangles which serve as a reactive ion etch (RIE) mask.

Reactive ion etching has become a very important tool for pattern transfer as part of the lithography process [Brodie and Muray, 1982]. In RIE, certain chemically active ionic species are formed in a plasma and are accelerated toward the substrate by an electric field. The substrate is etched by a combination of mechanical sputtering and chemical reaction, in which the bombarding ions react with the substrate material to form a highly volatile compound which is readily pumped away by the vacuum. This method generally offers several advantages over more conventional etching techniques such as wet chemical etching and sputter etching, particularly in the case of microstructures. These are the high degree of anisotropy which is a result of the field accelerating the ions perpendicular to the substrate, high material selectivity, as long as the etch gases are chosen wisely, and the fine control over the etch rate and degree of anisotropy that can be obtained by adjusting the chamber pressure, gas flow rate and accelerating potential to optimal conditions. The RIE system[2] used in this work was characterized by D. W. Face, and a detailed description of the system can be found in his Ph.D. thesis [Face, 1987].

For the present work, the material to be etched is the polyimide x-ray mask

---

[1]Model 3118, Vacuum Division, Varian Assoc., Inc., Palo Alto, California.

[2]Model CV-300, Cooke Vacuum Products, Norwalk, Connecticut.

membrane. This is most readily accomplished using O_2 as the etch gas, as is the case in the etching of most organic materials. Under optimal conditions, the etch rate of polyimide is ~ 1000 Å/min. The etching of the chromium film is undetectable. Thus, the polyimide under the chrome is unetched. The mask membrane is etched for 2.5 minutes, leaving pedestals ~ 2500 Å high beneath the chrome triangles. The sidewalls of the pedestals are smooth and vertical.

The next step in the mask fabrication sequence is the formation of the x-ray absorber pattern. In order to obtain a narrow wire using a positive resist and liftoff processing, as discussed above in Sec. III.A.3, the mask pattern must consist of narrow slots in the absorber, which correspond to the narrow wires. This way, the resist is exposed only where x-ray photons are transmitted through these slots. In addition, larger clear areas must be formed at the ends of the slots which correspond to contact pads for making electrical contact to the wires. This can all be accomplished in a single step, as shown in Fig. III-7. Before the absorber is deposited, a metal mask is placed over the polyimide film and held in contact with pressure applied by set screws. The metal mask has a 220 μm wide clear strip down the center, through which the absorber is deposited. The strip is aligned using the vertices of the triangles, so that it runs perpendicular to the triangle bases (Fig. III-7). The absorber is deposited through this strip, leaving broad clear areas on either side of the strip which form the contact pad pattern on the x-ray mask.

The absorber material used in this work is gold, which is commonly used in most x-ray work. It has a high mass absorption coefficient [Henke and Ebisu, 1974] and is easy to deposit from a point source by thermal evaporation. It can be seen from Fig. III-6 that in order to obtain sufficient contrast (~ 5 dB) between the

polyimide x-ray mask membrane and the gold asorber, approximately 1000 Å of gold are needed at the Cu_L line and 700 Å are needed at the Cκ line for a 1 μm thick polyimide membrane. Typically, 750 - 1000 Å of gold are used in this work. The gold is wound tightly around a tungsten filament,[1] which is aligned directly beneath the center of the x-ray mask parallel to the bases of the triangles. The 3 mm diameter tungsten filament serves as an effective point source to the x-ray mask, which is ~ 24 cm away. The mask is held at an angle with respect to the vertical, so that the gold is deposited across the steps at the bases of the triangles. This leaves a gap in the gold in the shadow of the steps (Fig. III-7). The width of the gap is determined by the height of the triangle pedestals and the angle of deposition. Since gold adheres poorly to polyimide, a thin layer (~ 100 Å) of chromium is deposited immediately prior to the gold evaporation (without breaking vacuum). This promotes adhesion between the gold and the polyimide membrane.

At this point, the x-ray mask patterning is complete. The pattern consists of a gold strip ~ 220 μm wide with narrow gaps in the gold which correspond to the narrow wires. The clear areas on either side of the strip correspond to the electrical contact pads in the final pattern, as mentioned above. Fig. III-8 shows a scanning electron microscope (SEM) photograph of such a mask pattern.

After the gold evaporation, the patterned polyimide film is still on the glass substrate on which it had originally been spun. The polyimide must be separated from the glass, and the mask must be placed on a support structure suitable for use in the x-ray exposure system. This procedure is shown schematically in Fig. III-9.

---

[1]R. D. Mathis Co., Long Beach, California.

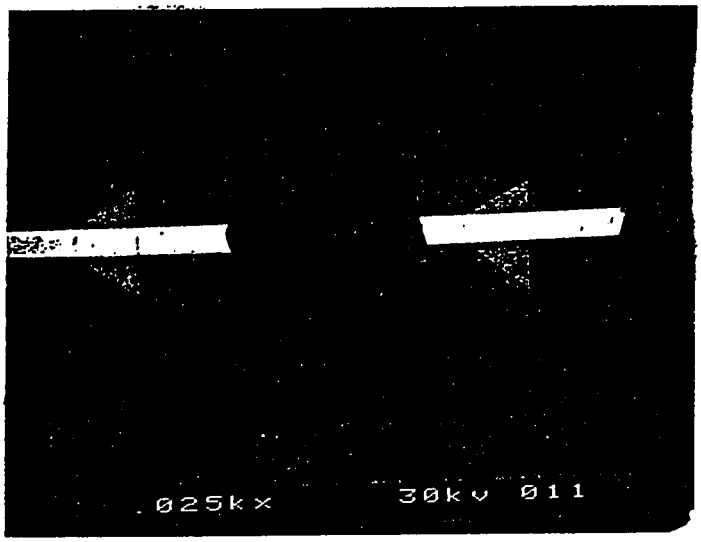

Fig. III-8. SEM micrograph of a portion of an x-ray mask pattern. Visible is the 220 μm wide gold absorber across the chromium triangles. Narrow slots (not visible at this magnification) are formed at the bases of the triangles. Gaps in the gold are for stress relief.

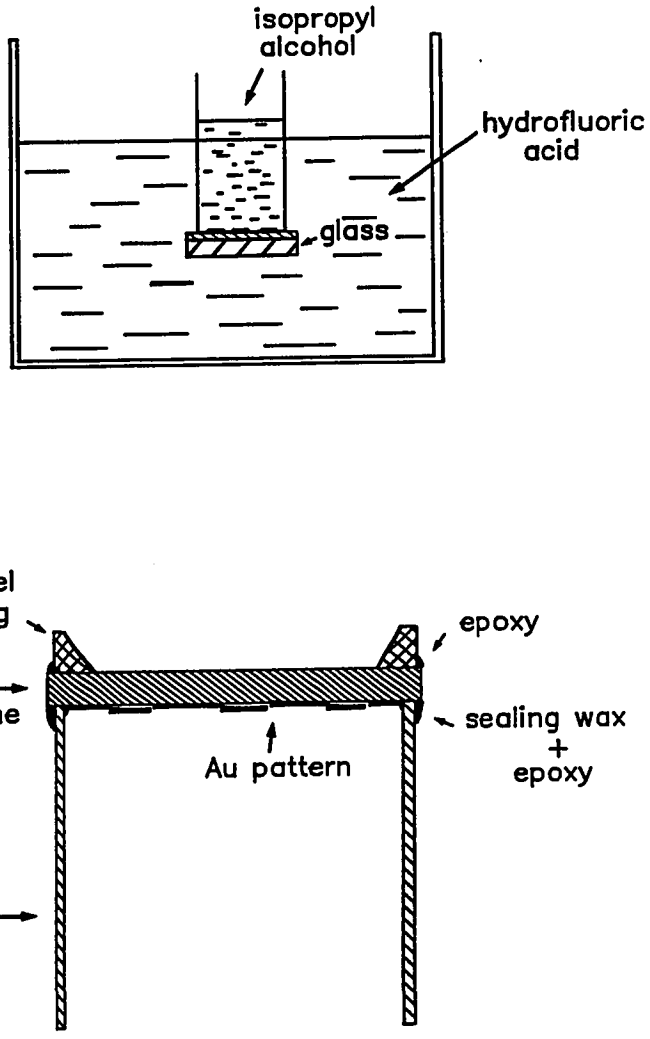

Fig. III-9. Removal of the glass substrate from the x-ray mask membrane and bonding of the membrane to the Vespel support ring.

The first step is the removal of the glass substrate by etching in hydrofluoric acid. The polyimide film is bonded to a copper or brass cylinder with 5-minute epoxy[1] to support the film during the etching. The epoxy is covered with black wax to ensure a good seal against the acid. The end of the cylinder bonded to the mask is then immersed in a solution of hydrofluoric acid and water (1:1) which etches an 8 mil thick glass cover slip in approximately 30 minutes. Prior to the etching, a small amount of isopropyl alcohol is poured into the cylinder to provide positive pressure against the polyimide surface and to dilute any etchant that may diffuse through pinholes in the polyimide. One can easily determine when all the glass has been removed by placing a few small drops of water on the film surface. Water does not wet polyimide, so if the etching has indeed been completed, the water will bead up on the polyimide. Afterwards, the surface of the polyimide film is gently blown dry with nitrogen gas.

Following the removal of the glass, a Vespel[2] support ring, 1 cm in diameter, is bonded to the rear side of the polyimide membrane using an epoxy.[3] The ring has 5° bevel to keep the polyimide membrane taut and to facilitate separation of mask and substrate after x-ray exposure, as will be described in Sec. III.B.4. The inner wall of the ring has a 45° slope to aid electrical contact for the electrostatic holddown.

Electrostatic holddown is a technique used to minimize the effects of two types

---

[1]Devcon Corp., Danvers, Massachusetts.

[2]E. I. DuPont deNemours and Co., Wilmington, Delaware.

[3]Tra-Con 2555 epoxy, Tra-Con, Medford, Massachusetts.

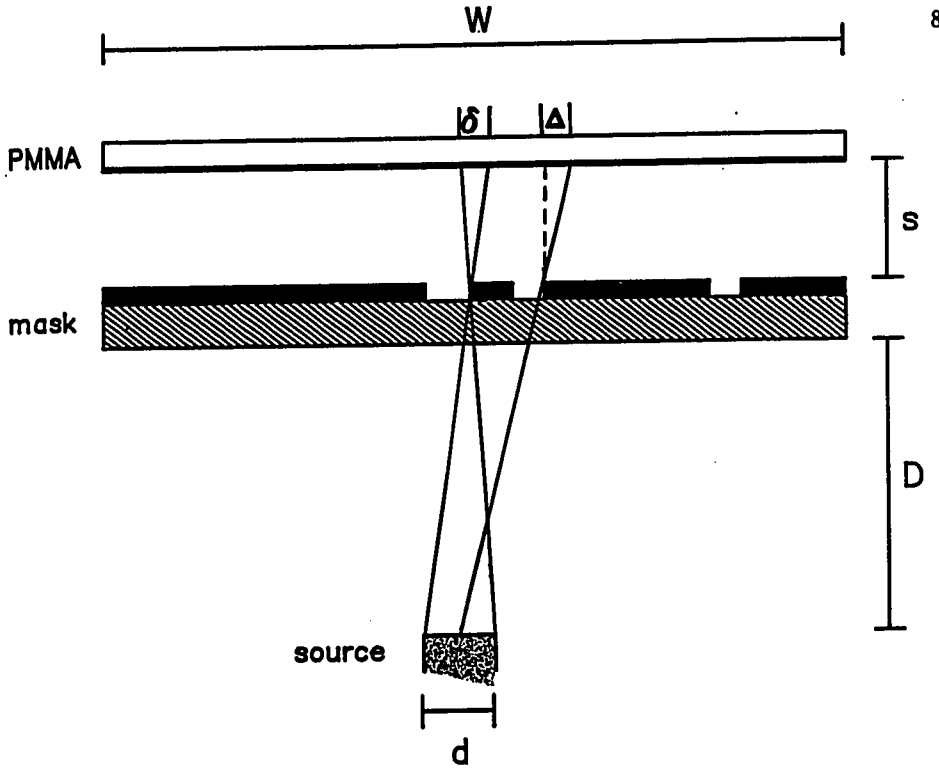

$$\delta = \frac{sd}{D} \qquad \Delta = \frac{sW}{2D}$$

Fig. III-10. Effects of penumbral blurring, δ, and geometric distortion, Δ, caused by the finite size of the x-ray source and the noncollimated nature of the exposing radiation.

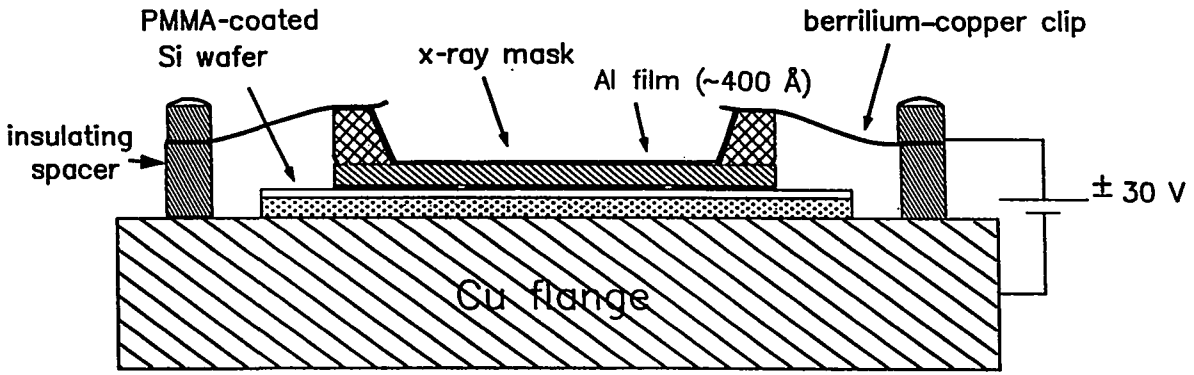

Fig. III-11. Maintenance of intimate contact between x-ray mask and substrate via electrostatic holddown.

of distortion that arise from the fact that the x-ray source has a finite size and is not collimated [Brodie and Muray, 1982]. These distortions, penumbral blurring and geometric distortion, shown schematically in Fig. III-10, can effectively be eliminated by maintaining the x-ray mask and substrate in intimate contact during exposure and thus reducing the mask-substrate spacing to zero. This is accomplished by coating the back of the mask with a thin layer of aluminum (~ 400 Å) and then applying a potential (30 V) across the mask-substrate assembly (the substrate is a silicon wafer), as pictured in Fig. III-11. This arrangement is essentially a parallel plate capacitor, with the polyimide and the resist serving as the dielectric, so that a force is exerted on the polyimide film, keeping it in contact with the resist-coated substrate. The mask-substrate spacing can be monitored by measuring the capacitance of the assembly. An added advantage of the aluminum coating on the mask is that it helps block infrared radiation from the x-ray source, which may tend to crosslink the resist. The x-ray attenuation of this Al layer is minimal [Henke and Ebisu, 1974].

Fig. III-12 is a SEM photograph of an x-ray mask in which some of the salient features of the mask can be seen (Fig. III-8 shows a broader view of the x-ray mask pattern). Here, part of the gold absorber has peeled away, revealing the RIE-formed step in the polyimide and the gap in the gold at the base of the step.

Masks with narrow gaps ranging from several microns down to ~ 400 Å have been produced in this work. The masks are fragile and must be handled with care; however, when handled properly, they are sufficiently robust to stand up to the

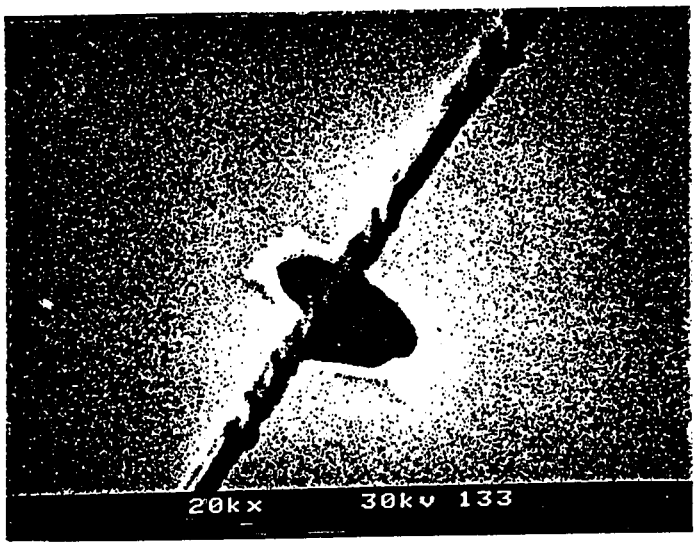

Fig. III-12. SEM micrograph of an x-ray mask pattern for ultranarrow wires. Visible are the narrow slot in the gold x-ray absorber as well as part of the RIE-formed polyimide step where some of the gold has peeled away.

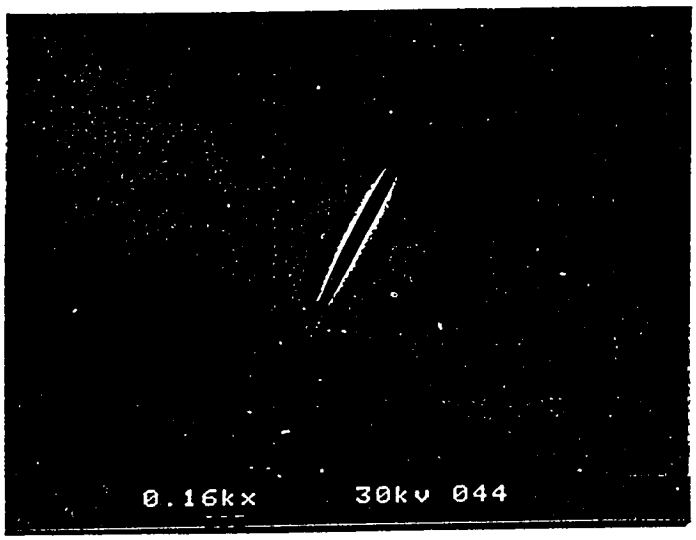

Fig. III-13. SEM micrograph of an x-ray mask showing tearing of the mask membrane after the glass substrate had been removed.

rigors of several exposures. The typical x-ray mask lifetime in this work ranged from 2 to 10 exposures. The most common symptoms of mask failure were stretching of the mask membrane and peeling away of the gold absorber. Both symptoms appeared to be the result of overuse or indelicate handling. Heating of the mask during x-ray exposure may also contribute to mask failure. No systematic study on this type of mask failure was carried out in this work.

There was another mode of mask failure which occurred during the fabrication procedure and not during subsequent processing. This was the tearing of the mask membrane at the base of the triangles (i.e., where the narrow gap is formed) after the glass substrate had been removed. Fig. III-13 shows an example of such tearing. This was apparently due to a mismatch in the film stress betweem the polyimide membrane and the chromium-gold absorber. We found that the the stress could be relieved by placing breaks in the gold strip at various intervals, so that the gold did not span the entire diameter of the x-ray mask. This also provided the additional feature of having built into the mask pattern an electrical short between the large area contact pads. In this way the narrow wire sample is protected from electrostatic discharge until it is placed into the measuring circuit (see Sec. IV.A for details).

III.B.3. The X-Ray Resist

The x-ray resist used in this work is poly-methyl-methacrylate (PMMA). PMMA is actually an electron-beam resist, however, as explained in Sec. III.B.1, upon exposure of PMMA to x-rays, low energy photoelectrons are emitted in the resist which break polymer bonds, thus altering the chemical properties of the exposed

areas. The resolution is determined by the range of these photoelectrons in the resist. An additional factor which is believed to determine the intrinsic resolution of the resist [Howard and Prober, 1982] is the physical integrity of the resist. Experiments exploring this limit [Flanders, 1981] have found that the PMMA (molecular weight 950,000) loses its adhesion properties at ~ 150 Å. This is only slightly larger than the smallest features developed in PMMA to date ~ 100 Å [Mackie and Beaumont, 1985; Mankiewich et al., 1986], for which a lower molecular weight PMMA was used. Thus, PMMA certainly offers the highest available resolution of all commonly used electron-beam resists to date, and its demonstrated resolution is certainly sufficient for the requirements of this work.

PMMA was used in this work in two forms. In the early stages, a single layer of 950,000 molecular weight PMMA[1] was spun onto a polished and oxidized silicon wafer (oxide thickness ~ 5000 Å) to a thickness of ~ 4000 Å from a 4% solution in chlorobenzene and baked at 180 °C for 1 hour. In the latter stages, a process was developed which utilized a bilayer of different molecular weights PMMA [Rooks et al., 1987; Mackie and Beaumont, 1985]. The bilayer consists of a lower layer of 185,000 molecular weight PMMA[2] followed by an upper layer of 450,000 molecular weight PMMA.[3] Each layer is spun to a thickness of ~ 500 Å from a solution of ~ 3% in xylene. Xylene is a poor solvent of PMMA, so that when the upper layer is applied, the bottom layer is not appreciably affected. The first layer is initially baked for 1 hour at 180 °C, and after the top layer is spun on, another 180 °C bake

[1]KTI Chemicals, Inc., Sunnyvale, California.

[2]BDH Chemicals, Ltd., Poole, England.

[3]Aldrich Chemical Co., Inc., Milwaukee, Wisconsin.

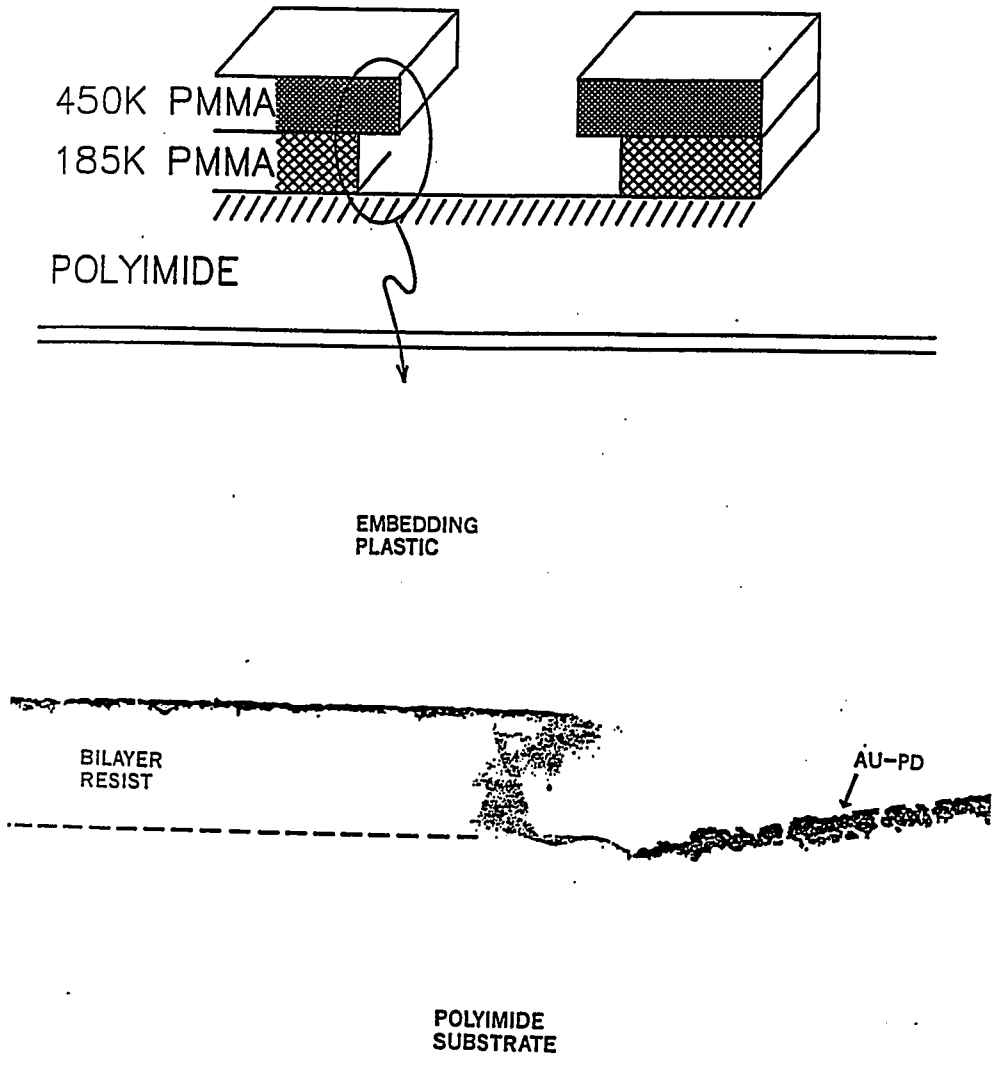

Fig. III-14. Transmission Electron Microscope (TEM) photograph of a PMMA/PMMA bilayer resist profile on a polyimide substrate. Following exposure and development, thin crosssectional slices are prepared by standard TEM techniques. (From [Rooks et al., 1987].)

follows for 2 hours. It has been found [Rooks et al., 1987] that the bilayer resist offers a somewhat wider processing latitude and better liftoff properties than the single layer. The advantage of the PMMA/PMMA bilayer is rooted in the fact that the bottom layer is slightly more sensitive to x-ray (or e-beam) exposure than the top layer [Mackie and Beaumont, 1985]. When developed, the bilayer has an undercut profile (Fig. III-14), which helps improve the liftoff properties. Complete details of the bilayer process can be found in [Rooks et al., 1987] and [Rooks, 1987]. Experiments using very thin single layers of the lower molecular weight PMMA yielded high resolution but poor liftoff properties.

III.B.4. X-Ray Exposure and Development

After a mask is fabricated and a substrate is coated with PMMA as described above, they are placed on a water-cooled copper vacuum flange (Fig. III-5) and are placed in the exposure system. No mask-to-wafer alignment is necessary, since the mask contains the entire pattern. (If desired, the narrow wire pattern may be lined up along the direction of one of the crystal planes of the <100> wafer to facilitate cleaving the wafer when the sample is being prepared for insertion into the cryostat, as will be described in Sec. IV.A.) After the system has been evacuated to a sufficiently low pressure ($< 1 \times 10^{-7}$ torr), exposure commences. Exposure times are determined by estimating the x-ray power absorbed in the unmasked areas of the PMMA based on the exposure configuration and the absorption characteristics of the polyimide membrane [Greeneich, 1975; Nelson and Ruoff, 1978]. A total energy density of $\sim$ 1 Joule/cm^2 is needed to develop the PMMA at a rate of 1000 Å/min [Hawryluk, 1981]. Typical exposure times used in this work were 1.5 - 2 hours for the Cu target with 320 Watts of electron beam power into the target, and 2.5 - 3

hours for the carbon target at 240 Watts.

Following exposure, the x-ray mask and substrate are removed from the exposure system and prepared for developing. As the mask and substrate have been kept in intimate contact throughout the exposure, they must be separated carefully; otherwise, the mask membrane may be damaged. The separation is done by soaking the mask and substrate in isopropyl alcohol until some of the alcohol seeps underneath the beveled edges of the mask and weakens the adhesion between the mask and substrate. Then the mask may easily be removed. The substrate is then placed in a 1:3 solution of methyl-isobutyl-ketone and isopropyl alcohol at 21 °C, which preferentially dissolves the exposed areas of the the PMMA (the unexposed areas are virtually unaffected [Rooks et al., 1987]. Development of the resist is monitored by observing the large area pad structures. When all the PMMA has been removed in these areas, the development is considered complete. The substrate is removed from the developer and rinsed in isopropyl alcohol. Typical development times for this work were ~ 2 minutes for the 4000 Å thick single layer PMMA and ~ 30 seconds for the PMMA/PMMA bilayer. The developed pattern is then examined in an optical microscope. (If there are indications that a portion of the pattern is not fully developed, the substrate is quickly dipped in the developer for an additional few seconds.) The sample is then ready for metallization.

III.B.5. Metallization and Liftoff

Following development, a thin metal film is deposited onto the patterned substrate by thermal evaporation. For the quantum interference studies, the metals were either Al or Ag. The choices of these metals is discussed in Sec. III.A.1. The

Al and the Ag are 99.999 % pure,[1] and are evaporated from a tungsten rod source or a boat,[2] respectively. For the purpose of observing microlithographically defined patterns in a scanning electron microscope, it is instead convenient to deposit Cr because of its high contrast with SiO_2 (the substrate) [Goldstein et al., 1981]. Also, Cr is quite brittle, and is therefore easy to lift off. The Cr is evaporated from an electroplated tungsten rod[2] to a thickness of a few hundred Angstroms. Film thickness is determined from a calibrated thickness monitor[2] in the evaporation system; it has been found to be accurate to within 5%.

If the PMMA is slightly underexposed, it tends to leave a very thin residual film on the substrate, no matter how long it has been developed [Beaumont et al., 1981]. This, as well as dirt particles which may settle on the exposed parts of the substrate will prevent the evaporated material from sticking properly to the substrate. This problem manifests itself in the form of discontinuous sections in the final sample. However, such discontinuities can be avoided. This was accomplished in this work by either subjecting the developed resist pattern to a very brief RIE just prior to metallization, or by cleaning the substrate with an oxygen glow discharge. The glow discharge is preferrable, because it is more gentle and can be done in situ in the evaporation system.

After the metal film has been deposited, the unwanted metal is lifted off by dissolving the unexposed PMMA in acetone. This is most readily accomplished by first soaking the sample in acetone for ~ 20 minutes. When the film is seen to

---

[1]Alfa Products, Danvers, Massachusetts.

[2]R. D. Mathis Co., Long Beach, California.

pucker, it can be removed by "shooting" acetone from a syringe. In the case of Al, this procedure may have to be repeated several times, since Al atoms tend to migrate and "creep" over the resist edges during film deposition, making liftoff difficult.

Fig. III-15 shows a typical wire fabricated by x-ray lithography. Its linewidth is 4000 Å, and it is fairly uniform throughout the length of the wire. The narrowest wire fabricated by x-ray lithography in this work was ~ 400 Å wide. However, the wire was discontinuous and its width was not very uniform. This is not surprising, since Flanders and Smith [1978] found distortions on the order of a few hundred Angstroms in the center of polyimide x-ray masks of approximately the same size as the ones used in this work. The narrowest continuous wire fabricated in this work had a linewidth of 800 Å.

For some of the quantum interference experiments in this work, fabrication by x-ray lithography is not well-suited. Certainly, the mask patterning scheme described in this chapter cannot be easily adapted to the fabrication of ring structures. Also, it is not convenient to use x-ray lithography for producing samples for the study of the one-dimensional electron-electron scattering rate. For such a study, one requires a set of wires of various widths (all less than ℓ_T ~ 1000 Å) but of the same material and electrical properties, so that theoretical predictions regarding the width dependence of the scattering can be tested. The shadowing technique for patterning the x-ray masks described in Sec. III.B.2 will not produce a mask for making wires of different widths. In addition, mask stretching and distortion make it difficult to control the linewidth when it approaches 500 Å. Fortunately, an alternative became available at the time these experiments were embarked upon. The Council of Engineering at Yale acquired a scanning electron

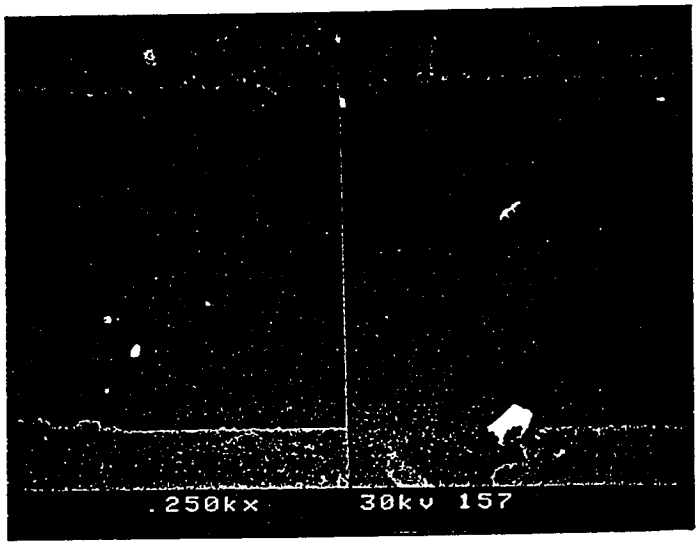

Fig. III-15. SEM micrograph of an x-ray fabricated wire. The wire width is 4000 Å.

microscope. Through the efforts of M. J. Rooks and others (see [Rooks, 1987]) the SEM was converted into a high resolution electron-beam writing tool. Samples for 1D electron-electron scattering studies as well as experiments on the Aharonov-Bohm effect in metal ring structures were fabricated using this facility.

III.C. Electron-Beam Lithography

Electron-beam lithography is currently the most widely used microlithographic techique for achieving resolutions ~ 0.5 μm or less. An electron beam is scanned across a resist-coated wafer according to a given pattern. The electrons are absorbed in the resist, where they emit secondary electrons which break molecular bonds, causing the resist to be either more or less soluble in a developer. Electron beams are attractive for lithography for a number of reasons: 1) Electrons can be imaged to form either a pattern or a small point ~ 100 Å or less, 2) they can be deflected or modulated by electrostatic or magnetic fields and 3) the electron beam energy and current can be precisely controlled so as to deliver a prescribed dose to the resist. Although sophisticated equipment and instrumentation is generally required for the implementation of an e-beam system, its operation is conceptually simple. An electron source (normally thermionic, although field emission sources are also used) supplies free electrons, which are accelerated by electrostatic fields and focused to a very small point onto the substrate by electromagnetic fields. The electron beam is deflected by electromagnetic fields so that it scans across the substrate according to a given pattern.

The resolution of an electron-beam system is generally determined by the size of the e-beam spot as it is focused on the resist (which is itself determined by the

electron optics) and by the scattering of electrons in the resist or from the substrate. Backscattered electrons from the substrate can cause spurious exposure of the resist several microns away from the area where the electron beam has been scanned. This is known as the "proximity effect" [Chang, 1975]. It can be controlled by exposing adjacent features with a proximity-corrected dose [Brodie and Muray, 1982], or it can be avoided by using a very thin substrate of low atomic number (see, e.g., [Molzen et al., 1979; Beaumont et al., 1981]). Alternatively, for cases where the close packing of features is not essential, such as the present work, the proximity effect can be avoided by separating the small features by large distances (larger features are somewhat more forgiving since they have a wider exposure latitude).

Another difficulty encountered in e-beam lithography is the size of the field over which uniform exposure can be obtained. This is due to the limitations of the electron optics. For most work involving the patterning of features $\lesssim$ 1000 Å, the field over which such features can extend does not exceed a few tens of microns, unless a very high grade system is used. For larger features, exposure fields can be stitched together, if necessary [Brodie and Muray, 1982]. For the electron-beam system used in this work, available e-beam current also limits the size of the field that can be exposed in a reasonable time. Features such as electrical contact pads (a few mm^2) can require several hours for a single e-beam exposure. For this reason it was decided that the contact pads be patterned separately using deep ultraviolet lithography.

III.C.1. Deep Ultraviolet (DUV) Exposure

DUV exposure can be made in the same resist as is used for e-beam exposure [Lin, 1975]. This was useful for the present work, since the contact pads and the small-feature sample could then be deposited in the same step. The resist used for most of the DUV/e-beam work is the PMMA/PMMA bilayer described in Sec. III.B.3. The light source used in this work was either a low pressure mercury lamp or a zinc lamp. The PMMA-coated substrate is held in contact with a chrome-on-quartz or aluminum-on-quartz mask. Details of the DUV exposure system can be found in [Rooks, 1987]. Following DUV exposure, the PMMA is developed in a solution of MIBK and isopropyl alcohol, as in Sec. III.B.4. The unexposed areas are virtually unaffected by this step. The DUV-exposed contact pad pattern is shown in Fig. III-16.

III.C.2. Electron-Beam Exposure

The e-beam exposure for this work was done in a ISI SS-60 scanning electron microscope.[1] Exposure is carried out in the following manner: The beam is swept across the substrate in an X-Y raster scan which is externally controlled by a Hewlett Packard Series-200 computer[2] via a custom built interface [Rooks, 1987]. The computer also controls an electrostatic beam blanking unit which deflects the beam away from the writing field. The e-beam lithography system is shown schematically in Fig. III-17. The pattern to be written is mapped onto a grid of

[1]International Scientific Instruments, Inc., Santa Clara, California.

[2]Hewlett Packard, Cupertino, California.

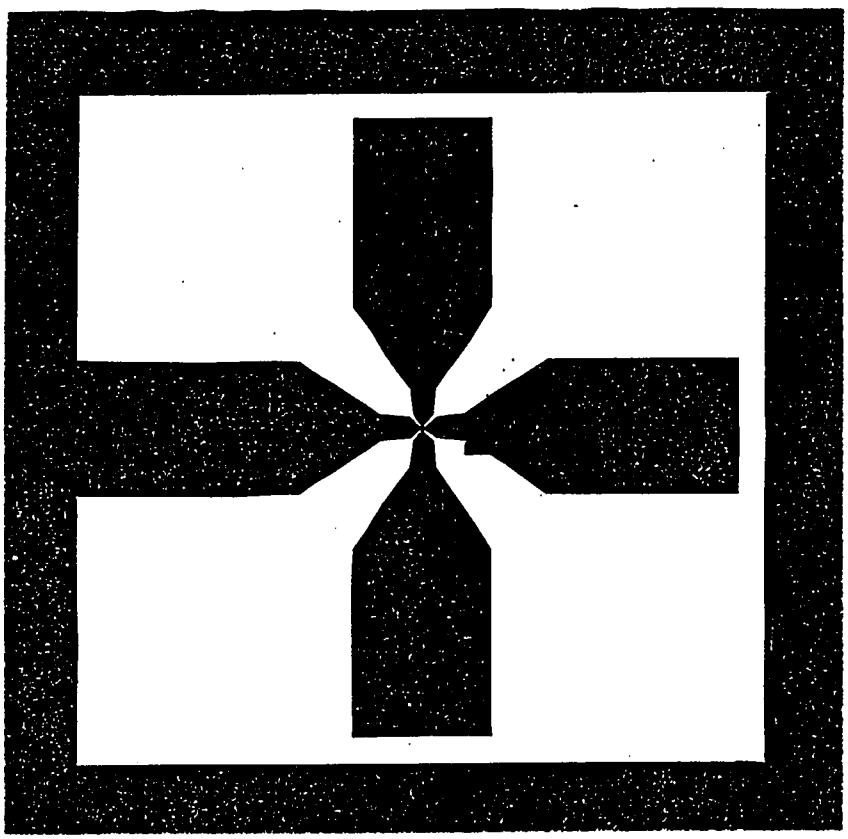

Fig. III-16. Pattern for electrical contact pads formed by DUV lithography. The pattern measures 2.5x2.5 mm^2. The light areas are metal. The e-beam defined pattern is written in a 40x40 μm^2 area in the center of the DUV pattern. The pads are electrically shorted to prevent current from flowing through the sample until it is inserted in the measuring appparatus. Once in the apparatus, these shorting bars are scratched out.

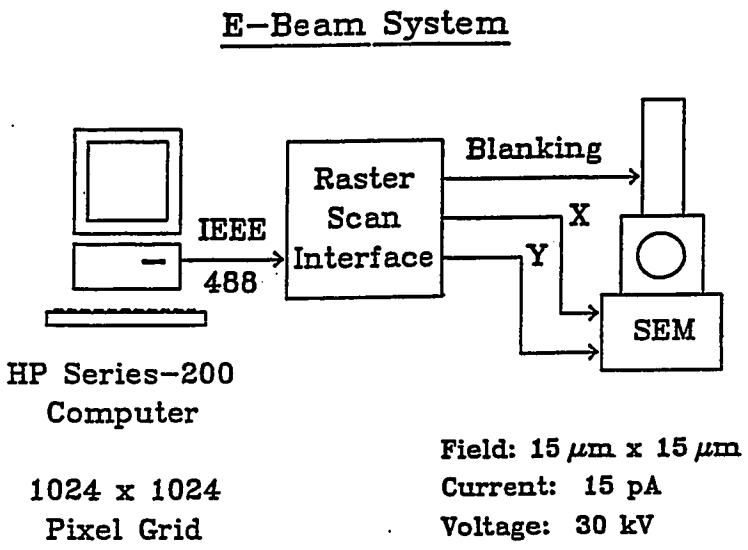

Fig. III-17. Electron-beam lithography system. A scanning electron microscope equipped with an electrostatic beam blanker receives an X-Y scan signal from a custom raster-scan interface. Blanking signals are sent through the interface from a Hewlett-Packard Series-200 computer. (From [Rooks, 1987].)

1024 x 1024 pixels. As the beam is rastered across the substrate, the computer "blanks" the beam for those parts of the pattern that are to be left unexposed. The typical writing field is 15 μm x 15 μm. The patterns for this work were written at a beam energy of 30 keV with beam current ~ 10 -15 pA. Alignment of the pattern relative to the DUV-exposed contact pad pattern is done by using the e-beam system in a SEM viewing mode at low beam currents. The edges of the DUV pattern are used for focusing and alignment. After the e-beam exposure has been completed, the PMMA resist is developed following the same procedure used after x-ray exposure. Metallization and liftoff are also the same. Figs. III-18 and III-19 show a typical narrow wire and ring fabricated by e-beam lithography. These structures and others like them were used in quantum transport studies.

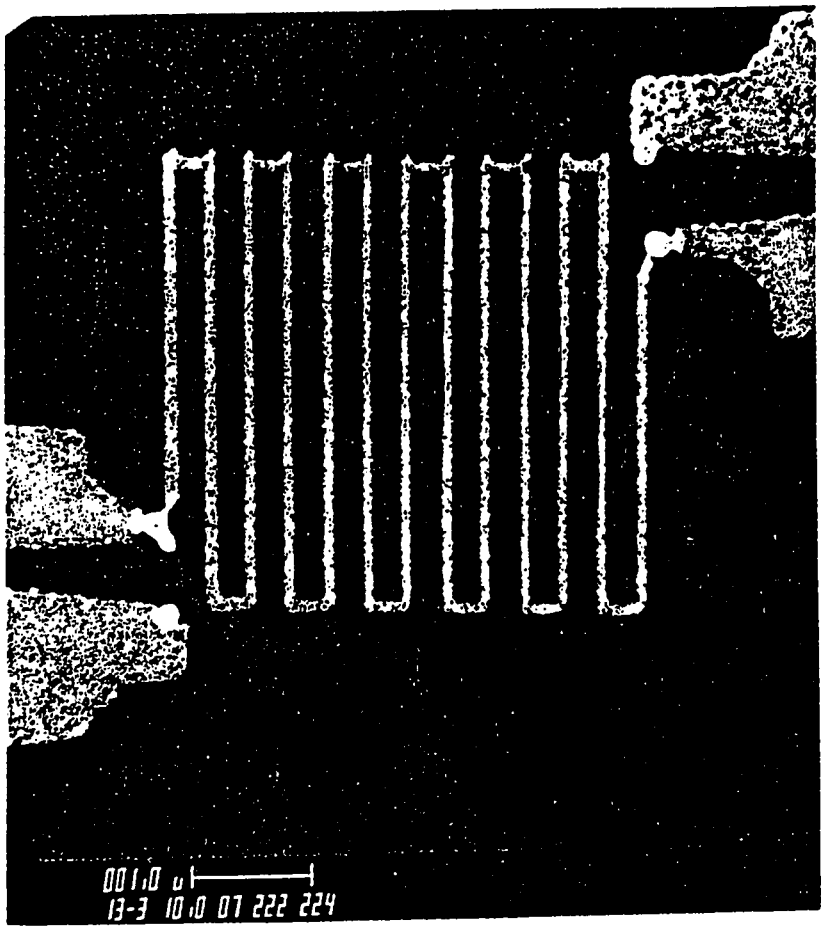

Fig. III-18. Narrow wire defined by electron-beam lithography. Wire width is 1000 Å. (Size bar at bottom shows 1 μm.) Wires as narrow as 350 Å have been fabricated in this work. This wire was accidentally destroyed by electrostatic discharge following low temperature measurement (causing the breaks between current leads and voltage probes).

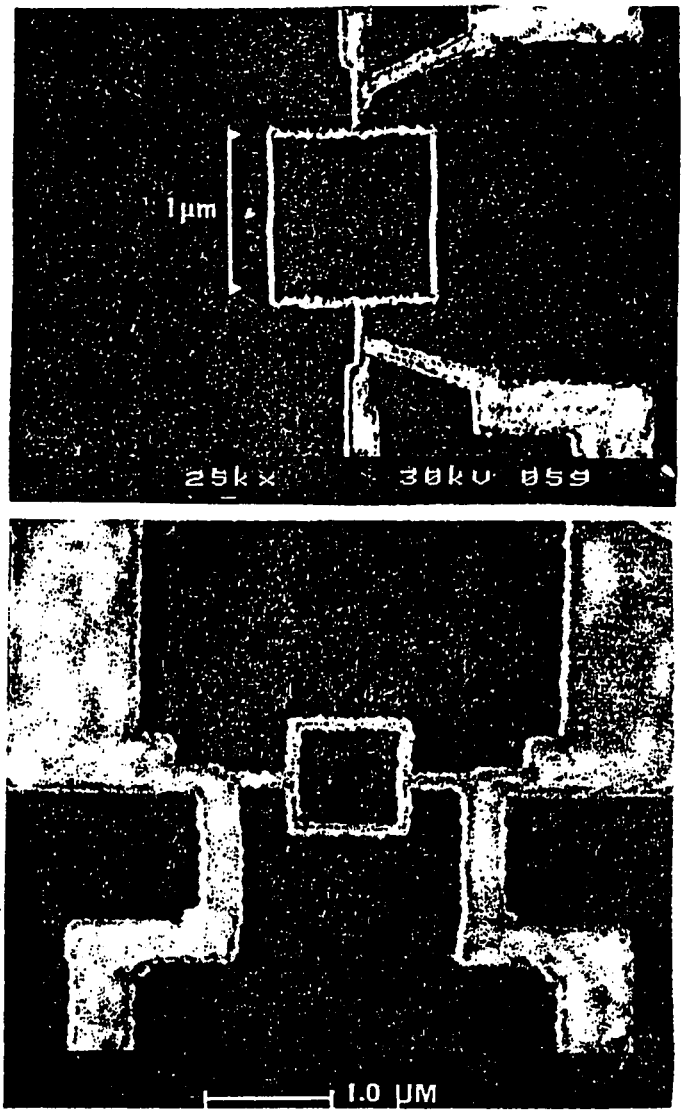

Fig. III-19. Electron-beam fabricated rings used for Aharonov-Bohm experiments.

IV. Measurement Techniques

IV.A. Sample Preparation

By virtue of their small size, the samples studied in this work were extremely delicate. Special precautions had to be taken to protect the samples from electrostatic discharge. Beginning with liftoff and extending through the time that it is mounted in the low temperature measurement apparatus, each sample is electrically shorted by lithographically defined shorts between the contact pads (see Figs. III-8 and III-16). In addition, after the sample has been mounted in the cryostat, all electrical leads are shorted to the cryostat head (= electrical ground), except for the time that actual measurements are taking place.

In order to facilitate electrical measurement of a sample, leads must be attached to the contact pads. This is accomplished by soldering small spots of pure indium onto the contact pads. When the surface of the sample is fresh (i.e., within a few hours after deposition) mechanically secure low resistance contacts can be made in this way. Care is taken to use a relatively cool soldering iron, such that the indium has just barely melted, so as to protect the sample. Additional precautions, such as the use of an humidifier during sample mounting, disconnecting the soldering iron from the ac source and electrically grounding the person who is doing the mounting, have also been found helpful. In the case of the Ag samples, in order to prevent diffusion of indium into the Ag upon application of heat, silver paint is applied between the Ag pads and the indium spots. The sample is then connected to the measuring circuit by soldering #40 copper leads to the indium spots. After a sample has been mounted in the cryostat, all leads are electrically tested to ensure that low

resistance contact has been made. Once this is done, the lithographically defined shorts between the contact pads are carefully scratched out, and the sample is ready for measurement.

Despite all the precautions that were taken to protect the samples, several samples in this work were "blown out" - some during sample handling and mounting, and some - inexplicably - while in the measuring circuit. It does appear, however, that the primary mode of damage is electrostatic discharge, as more samples were blown out during the winter months, when the relative humidity is usually quite low.

IV.B. Low Temperature Apparatus

The low temperature apparatus used in this work is the same as the one used by Dalrymple [1983] and by Santhanam [1985]. The cryostat is a variable temperature copper bar housed in a copper vacuum can. It is equipped with a stub for holding the sample plus a germanium resistance thermometer[1] and a metal film resistance heater for temperature control. Copper wires are threaded through the top of the cryostat for connection to the external part of the measuring circuit. The cryostat is immersed in a liquid He^4 bath, whose temperature below 4.5 K can be controlled by pumping on the He. With small amounts of He transfer gas in the vacuum can, temperatures as low as 1.2 K are attained. Above 4.5 K no transfer gas is used. The temperature can be held stable to ~ 1 mK at low temperatures using the sample block heater. When better stability is needed (e.g., close to the superconducting transition of the smallest Al samples), a PID (proportional-integral-

[1]Model CR-1000, Cryocal, Inc., St. Paul, Minnesota.

differential) feedback circuit [Forgan, 1974] is employed.

A NbTi superconducting magnet placed inside the liquid He dewar is used for the magnetoresistance measurements. Although it could provide fields up to 80 kG, for the experiments in this work, fields up to ~ 2 kG (and in some cases 5 kG) are required. This is readily attainable by operating the magnetic with a 12 V, 1 A power supply.[1] The magnetic field can be swept continuously with a resolution of ~ 1 mG.

IV.C. Resistance Measurement

Two types of measuring circuits were employed for the low temperature resistance measurements in this work: 1) a three-terminal arrangement using a modified LR-110 ac resistance bridge[2] and 2) a four-terminal ac bridge in conjunction with a lock-in amplifier[3] built by V. Chandrasekhar. These are pictured schematically in Figs. IV-1 and IV-2. The three-terminal bridge was used for measuring the samples produced by x-ray lithography. All other samples were measured using the four-terminal arrangement. The three-terminal bridge requires that differences in the lead resistances not contribute to the measured differential resistance. This is easily satisfied by the x-ray-defined contact pads, which are so large compared to the small sample that their resistance contributes negligibly to the measured resistance (i.e., the number of squares of resistance of the contact pads is

---

[1]Model 6214A, Hewlett Packard, Cupertino, California.

[2]Linear Research, Inc., San Diego, California.

[3]Model 126, Princeton Applied Research, Princeton, New Jersey.

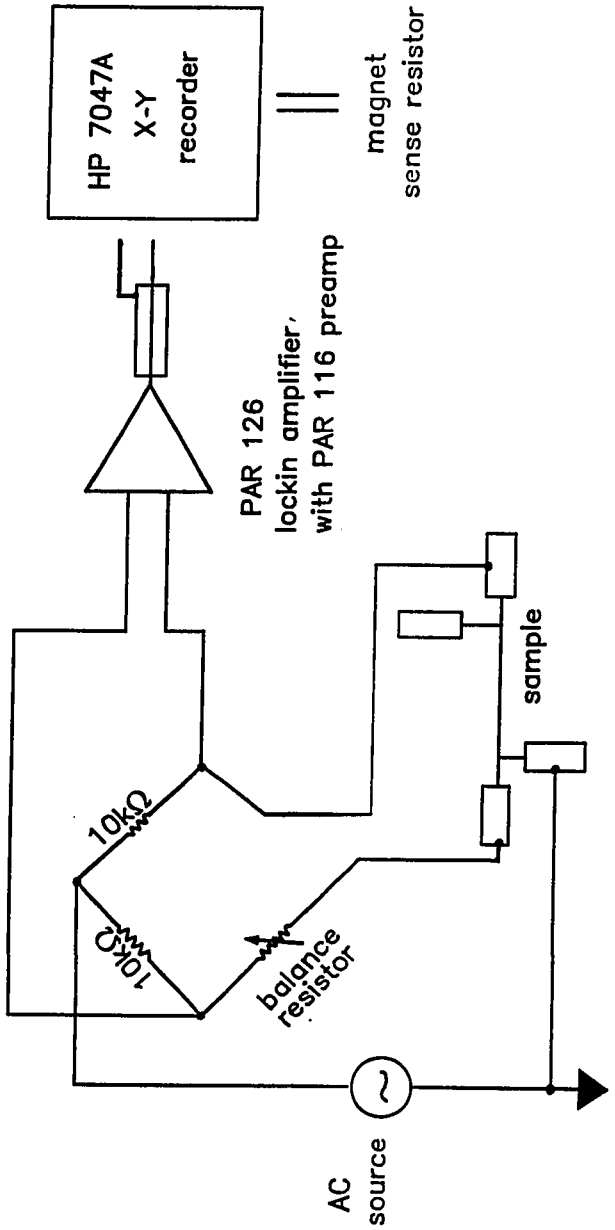

Fig. IV-1. Schematic diagram of the three-terminal resistance measuring apparatus. The difference in resistance between the sample leads must not contribute to the measured resistance.

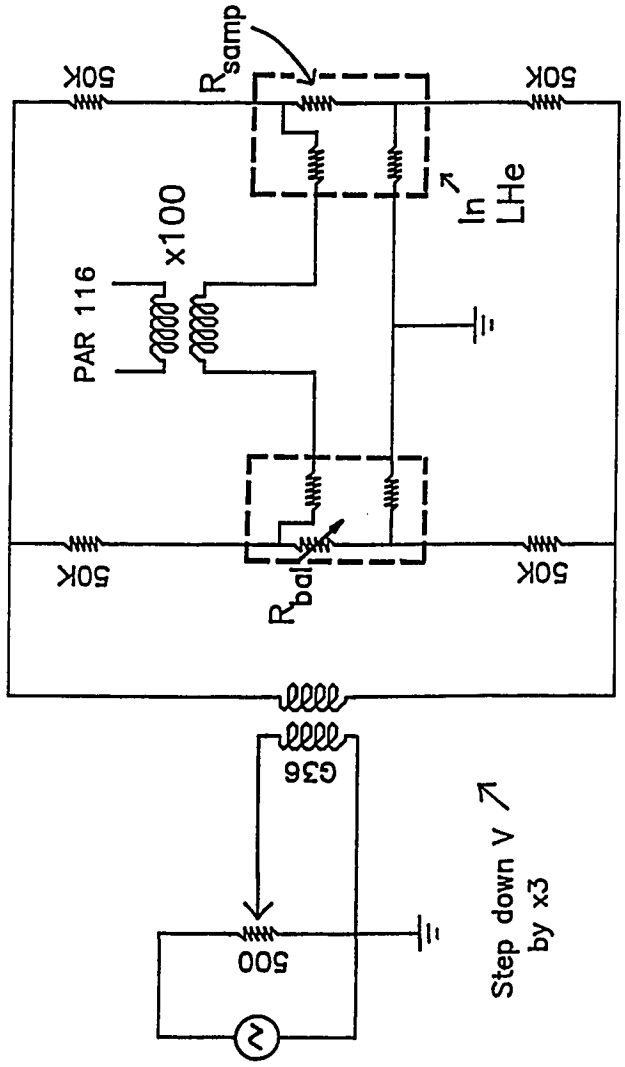

Fig. IV-2. Four-terminal AC bridge. The balance resistor is at room temperature.

negligible compared to that of the narrow wire). In the case of the three-terminal measurements, the magnetic field is swept manually and the bridge output is recorded on an X-Y chart recorder.[1] For the four-terminal circuit, V. Chandrasekhar has implemented a computer controlled[2] program which automatically sweeps the field and averages the bridge output, which is recorded on a floppy disc.

In all cases, the resolution is determined by the Johnson noise of the room temperature balance resistors in the bridge (~ 1 nV peak to peak in a bandwidth of < 1 Hz). For most of the small samples measured in this work, care had to be exercised to avoid heating the samples with excessive measuring currents. This limited the current to ~ 1 μA at the lowest temperatures. Even so, with typical measuring currents $\lesssim$ 1 μA (at 500 Hz) for narrow wires of resistance ~ 1 kΩ, a resolution of better than 1 part in 10^6 is attained, which is more than adequate for observing quantum interference phenomena in these samples.

It was found in measuring the narrowest Al wires (width ~ 500 Å) that close to the superconducting transition temperature (~ 1.3 K) the samples became extremely sensitive to external mechanical motion. In addition, even at the smallest attainable measuring currents, the samples would not go completely superconducting. We believe that this was due to inadequate shielding of the measuring circuit which may allow external RF fields to heat the samples slightly. Further improvements in the measurement configuration are expected to eliminate this problem.

---

[1]Model 7047A, Hewlett Packard, Cupertino, California.

[2]Model 9816, Hewlett Packard, Cupertino, California.

V. Experimental Results

V.A. Sample Properties

In order to be able to properly interpret the results of the experiments in this work, certain material and electrical properties of the samples must be known. An examination of some of the theoretical predictions in Chapter II should give an indication of the essential properties. These include the physical dimensions of the sample, its low temperature resistivity, the diffusion constant and for the case of Al, the superconducting transition temperature. The following discussion contains a survey of these properties and will describe how they were determined for the samples in this work.

Sample dimensions - By virtue of their small size, all the samples studied in this work had to be examined in a scanning electron microscope in order to determine their precise length and width. This was always done after all electrical measurements had been completed. Samples of width $\gtrsim$ 1000 Å were examined in the ISI SS-60 SEM[1] in the Yale University Center for Microelectronics. Narrower samples required the superior resolution of the JEOL 100CX STEM,[2] located in the Yale University School of Medicine. Electrical measurements were also used to confirm the dimensions determined in the SEM, so that an accuracy of better than 10% could be obtained. The sample thickness was determined during the sample

---

[1]International Scientific Instruments, Inc., Santa Clara, California.

[2]JEOL USA, Inc., Peabody, Massachusetts.

deposition by a quartz crystal thickness monitor[1] located inside the evaporation chamber. This has been calibrated and shown to be accurate to within 5%.

Sample resistivity - A measure of the sample resistance together with a knowledge of its physical dimensions will yield its resistivity (ρ = RWd/L). It is not necessary, however, to wait until the sample has been examined in a SEM to get an estimate of its resistivity. As mentioned in Sec. III.A.2, in most sample depositions, a 2D film was coevaporated along with the small sample. To the extent that the evaporant lands uniformly over all areas lying in the same plane, all samples that are evaporated together should have the same resistivity. In practice, this assumption was found to be approximately correct, with the measured resistivities of codeposited samples differing by 7% in the best case and 40% in the worst case. In all instances, the value of the resistivity measured for each sample was used in its analysis. The slight differences between 2D films and 1D wires and rings may be the result of the fact that for the ultrasmall samples, the material is deposited through a narrow slot in the resist.

The theoretical predictions in Chapter II are all expressed in a form containing the sheet resistance (or R per square), $R_\square$. $R_\square$ is directly related to ρ through the relation $R_\square = \rho/d$, where d is the sample thickness. Thus, all samples of the same resistivity and thickness have the same $R_\square$ regardless of their geometry.

An important quantity related to the resistivity is the residual resistivity ratio (RRR), which is the ratio of the room temperature resistivity to the low temperature

---

[1]R. D. Mathis Co., Long Beach, California.

resistivity, ρ_o. This gives a good indication of the relative purity of a given sample. Smaller values of this ratio are the result of a stronger contribution of impurity scattering to the overall resistivity of the sample. Samples having the same resistivity and the same residual resistivity ratio could be assumed to have the same impurity-determined resistivity. For the samples in this work, this was found to be the case for most coevaporated samples.

Samples of higher resistivity, and thus higher impurity concentration, will have a shorter elastic mean free path, ℓ. A precise relationship between ℓ and ρ_o can be obtained from the Drude formula for the conductivity, $\sigma = ne^2\tau/m^*$ (with m^* the effective mass replacing the free electron mass, m_o), so that

$$\rho_o \ell = \frac{m^* v_F}{ne^2} . \qquad (V\text{-}1)$$

For Al, this gives $\rho_o\ell = 3.6 \times 10^{-12}$ Ω-cm^2 for $m^* = 1.4m_o$ [Lawrence and Meador, 1978], $v_F = 1.3 \times 10^8$ cm/sec [Fawcett, 1960] and $n = 1.8 \times 10^{23}$ cm^{-3} [Ashcroft and Mermin, 1976]. For Ag, $\rho_o\ell = 5.36 \times 10^{-12}$ Ω-cm^2 may be used [Gershenzon et al., 1982]. Clearly, the $\rho_o\ell$ product should be constant, independent of the value of ρ_o, and one should be able to determine ℓ once ρ_o is known. Santhanam [1985] has found that this is apparently not so in the case of moderately disordered Al. Using values of ℓ determined from the slope of the superconducting upper critical field, he found that only for the cleanest samples ($\rho_o \sim 1$ - 10 μΩ-cm) does Eq. (V-1) hold to within a factor of 2. A similar situation was observed in the case of Cu films [van Haesendonck et al., 1985]. No explanation of this behavior is presently available.

Superconducting Transition Temperature - For superconducting samples, a

knowledge of T_c is important for determining the magnitude of the contribution of superconducting fluctuations to the low temperature magnetoresistance (see Sec. II.C.3). It can also be used in determining the diffusion constant, as will be explained below. For the samples in this work, where a broad superconducting transition was common, T_c was taken as the temperature at which the sample resistance reached half its normal state residual resistance. Typically, the width of the transition became broader with narrower samples. This may have been due to one-dimensional fluctuations close to the transition or to inhomogeneities in the sample. For the wires narrower than 1000 Å, a complete transition could not be observed down to the lowest measured temperature ~ 1.2 K. The transitions for these wires were also extremely "noisy". As mentioned previously, this may have been a result of pickup of small externally generated currents due to inadequate shielding of the measuring circuit. These currents together with the measuring current may easily have exceeded the critical current for parts of the wires. Since it had been found in the case of the wider wires (W > 1000 Å) that the coevaporated 1D wires and 2D films had the same transition temperature to within 20 mK, we deemed it reasonable to use the measured T_c value of the film for its codeposited wires. Even if the actual T_c differed by as much as 0.1 K, the ultimate difference in the inferred phase breaking rates (Sec.V.C) would be no more than 15% at the lowest measured temperatures.

Diffusion constant - $D = v_F\ell/3$ is an important quantity for a variety of purposes. As mentioned in Chap. II, for diffusive transport, the electron scattering length and scattering time for various scattering mechanisms are related according to $\ell_x = (D\tau_x)^{1/2}$, where the subscript x here may be substituted for by the appropriate symbol (e.g., ee for electron-electron scattering, or N for the scattering of electrons

by electromagnetic fluctuations). In most experimental situations, it is the phase coherence length which is determined from the magnetoresistance (see Sec. II.C), so that a knowledge of the diffusion constant is essential if the phase breaking time or rate is to be known. Also, the diffusion constant is an important parameter in determining the one-dimensional quasielastic electron-electron scattering rate (Eq. II-56), as well as the electron thermal diffusion length, $\ell_T = (\hbar D/k_B T)^{1/2}$.

There are several ways in which the diffusion constant can be estimated for different samples. In most instances, D can be found from the value of ℓ inferred from the $\rho_o \ell$ product, discussed above. However, as mentioned above, in the case of Al, the book value for $\rho_o \ell$ is reliable only for relatively clean samples. For superconducting samples, D can be determined from the slope of the superconducting critical field, dH_{c2}/dT, for fields perpendicular to the plane of the wire [Santhanam, 1985]:

$$\frac{dH_{c2}}{dT} = - \left[\frac{6\Phi_0^2 k_B}{\pi^3 W^2 \hbar D} \right]^{1/2} (T - T_c)^{-1/2} , \qquad (V\text{-}2)$$

with Φ_o = hc/2e, the superconducting flux quantum, and W the wire width. This formula applies when the wire width is less than the superconducting coherence length, $\xi(T)$ at $T \simeq T_c$. A similar formula for 2D films [Tinkham, 1975] has been found successful in determining D [Santhanam and Prober, 1984]. For those narrow wires mentioned above for which T_c could not be measured directly, D was estimated from the $\rho_o \ell$ product for the particular value of ρ_o of each sample, as established by the dH_{c2}/dT measurements on other Al samples [Santhanam, 1985].

The relevant sample properties are listed in Tables V-I and V-II for the wires

Table V-1

Sample Parameters for Narrow Wires

Sample	W (Å)	$R_\square$ (Ω)	ρ_o (10^{-6} Ω-cm)	ℓ (Å)	D (cm^2/sec)	T_c (K)	ℓ_{so} (μm)
Al1a	350	1.8	3.60	111	39	1.44	0.45
Al1b	460	1.8	3.60	111	39	1.44	0.45
Al2a	400	1.4	2.80	113	49	1.36	0.54
Al2b	600	1.4	2.80	113	49	1.36	0.54
Al2c	620	1.4	2.80	113	49	1.36	0.54
Al2Film	—	1.3	2.60	122	53	1.36	0.54
Al3	1100	1.1	2.20	145	63	1.32	0.56
Al4	2000	0.9	2.20	104	45	1.35	0.48
Al4Film	—	1.4	3.48	105	45	1.37	0.56
Al5	2400	1.2	2.78	84	37	1.34	0.57
Al6	6000	2.8	4.20	69	30	1.45	0.32
Al7	4000	4.5	6.72	74	32	1.49	0.30
Al7Film	—	5.6	8.48	60	26	1.51	0.24
Ag1	600	2.6	3.20	104	48	—	0.32
Ag2	1000	1.5	2.92	184	85	—	0.52

Samples are listed so that codeposited samples are grouped together.

Wires Al4, Al5, Al6 and Al7 correspond to samples A, B, C and D, respectively, of [Santhanam et al., 1984b].

Sample thickness was 200 Å for all samples except Al4 - Al7. Sample thickness for samples Al4 and Al5 was 250 Å and 240 Å, respectively, and 150 Å for both samples Al6 and Al7.

ℓ_s was 1.80 μm for sample Ag1 and 1.19 μm for sample Ag2.

Table V-2

Sample Parameters for Rings

Sample	Film	$R_\square$ (Ω)	Diameter (μm)	W (Å)	ℓ_ϕ (μm)	h/e effect
R1	Al	1.1	2.3	1900	1.7	—
R2	Al	1.6	2.3	2300	2.0	—
R3	Al	3.0	1.1	1900	1.0	unclear
R4	Ag	2.5	1.0	1400	0.9	yes
R5	Ag	1.6	1.0	1400	0.7	yes

The Al samples were 250 Å thick; the Ag samples were 150 Å thick. T_c = 1.2 - 1.3 K for the Al samples. ℓ_ϕ is taken at 1.7 K, except for sample R5, for which ℓ_ϕ is taken at 4.5 K. $\ell_{so} \sim 0.5$ μm for all samples. h/e oscillations were not investigated in samples R1 and R2.

and rings, respectively.

V.B. Magnetoresistance of Narrow Wires

The total magnetoresistance at a given temperature is given by

$$\frac{\delta R}{R}(T,H) = \frac{\Delta R}{R}(T,H) - \frac{\Delta R}{R}(T,H=0), \qquad \text{(V-3)}$$

where $\Delta R/R$ is the fractional change in resistance defined in Sec. II.C for the various contributions.

Fig. V-1 shows the normalized magnetoresistance, defined by Eq. (V-3), of sample Al4, a 2000 Å wide wire, at three representative temperatures. The solid lines in the figure are fits of a theoretical expression for the magnetoresistance comprised of contributions due to one-dimensional weak localization, including spin-orbit scattering, Eq. (II-26), and one-dimensional Maki-Thompson superconducting fluctuations, Eq. (II-36). The fitting was done manually. (A two-parameter least squares fit was attempted; it yielded inferior fits). The fitting involved varying ℓ_ϕ and ℓ_{so} at each temperature until optimal visual agreement between the theoretical curve and the experimental points was reached. In practice, the low field magnetoresistance at temperatures below ~ 5 K is less sensitive to the value of ℓ_{so} than at higher temperatures, so that at low temperatures, ℓ_ϕ can be varied in what is essentially a one-parameter fit. At higher temperatures, both ℓ_ϕ and ℓ_{so} are varied to obtain a good fit. Spin-orbit scattering is expected to be independent of temperature for simple metals (see, e.g., [Santhanam et al., 1984a]), and when ℓ_{so} is treated as a free parameter, this is indeed found to be the case; the

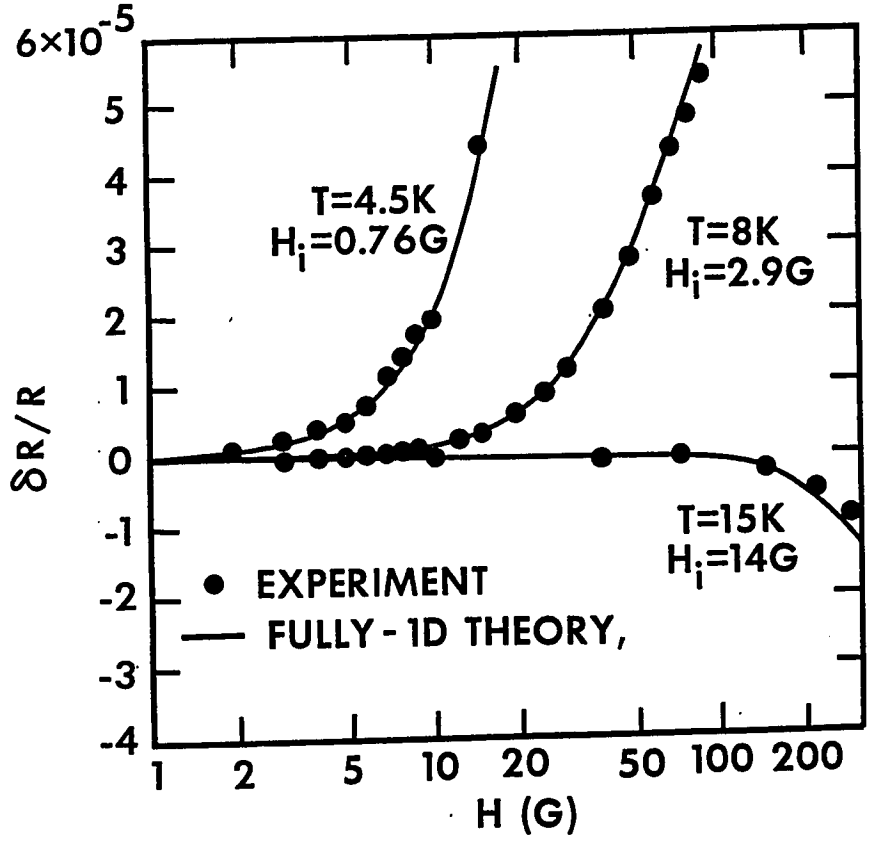

Fig. V-1. Normalized magnetoresistance for sample Al4, of width 2000 Å. ℓ_ϕ = 1.47 μm, 0.75 μm and 0.34 μm at 4.5 K, 8 K and 15 K, respectively, from the theoretical fits. ℓ_{so} = 0.49 μm.

magnetoresistance can almost always be fit satisfactorily with the same value of ℓ_{so} at all temperatures. The estimated accuracy of the fitting procedure is better than 5% for both ℓ_ϕ and ℓ_{so} based on the sensitivity of the fits to changes in the value of these parameters. For the Maki-Thompson contribution, the superconducting fluctuation parameter, $\beta(T/T_c)$, was calculated using a polynomial form [Santhanam, 1985] based on the tabulations of Larkin [1980], so that $\beta(T/T_c)$ was not a free parameter. In all cases, the fitting was done at magnetic fields low enough so that the theoretical expressions given in Chap. II are valid (i.e., $H < 3\hbar c/\pi eW^2$), for the localization contribution, and $H < ck_BTln(T/T_c)/4eD$, for the Maki-Thompson contribution). This still allowed sufficient field range to uniquely determine ℓ_ϕ and ℓ_{so} at all temperatures. The inferred values of ℓ_ϕ and ℓ_{so} will be discussed in Secs. V.D.1 and V.D.2.

Similar results were realized for other wires as well. Fig. V-2 shows the normalized magnetoresistance of sample Al2a, of width 400 Å. The fitting was done precisely as described above. In the case of this sample, as well as in the case of the other Al wires narrower than 1000 Å, it was found that at temperatures approaching the superconducting transition, satisfactory fits could not be obtained at fields higher than ~ 200 G, as shown in Fig. V-3. Initially, it was believed that this discrepancy was due to the contribution from Aslamazov-Larkin fluctuations (Sec. II.C.3a). However, an estimate of this contribution for the wires in this work, Eq. (II-35), found that it is not sufficiently large to account for the discrepancy. In any case, this discrepancy is larger for narrower wires, and it increases as T approaches T_c. It should be noted that the applicability of the perturbation calculation for the 1D Maki-Thompson contribution [Santhanam et al., 1984a] is limited to magnetic fields $H << (ck_BT/4De)ln(T/T_c) \sim 200$ G at 3 K for the samples in this work. An

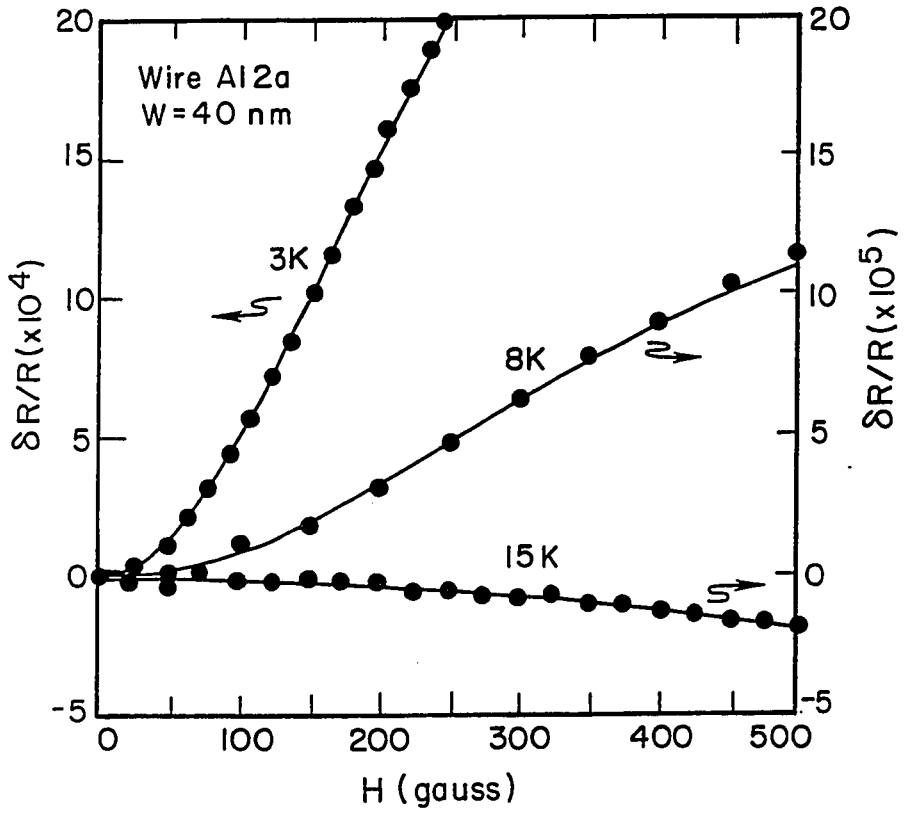

Fig. V-2. Normalized magnetoresistance for sample Al2a. Fitting parameters for the 1D theory are ℓ_ϕ = 1.19 μm, 0.52 μm and 0.24 μm at 3 K, 8 K and 15 K, respectively, and ℓ_{so} = 0.57 μm.

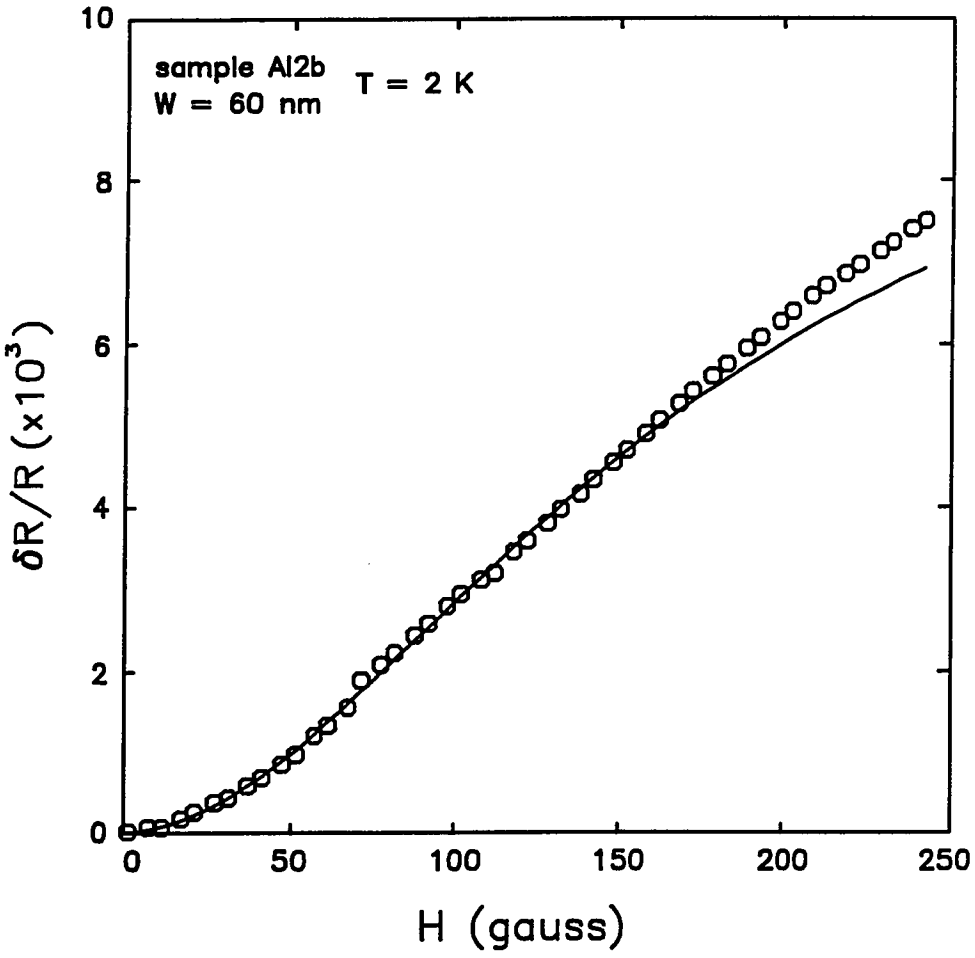

Fig. V-3. Normalized magnetoresistance for sample Al2b at 2 K showing the deviation of the data from the 1D theory at fields $\gtrsim$ 200 G.

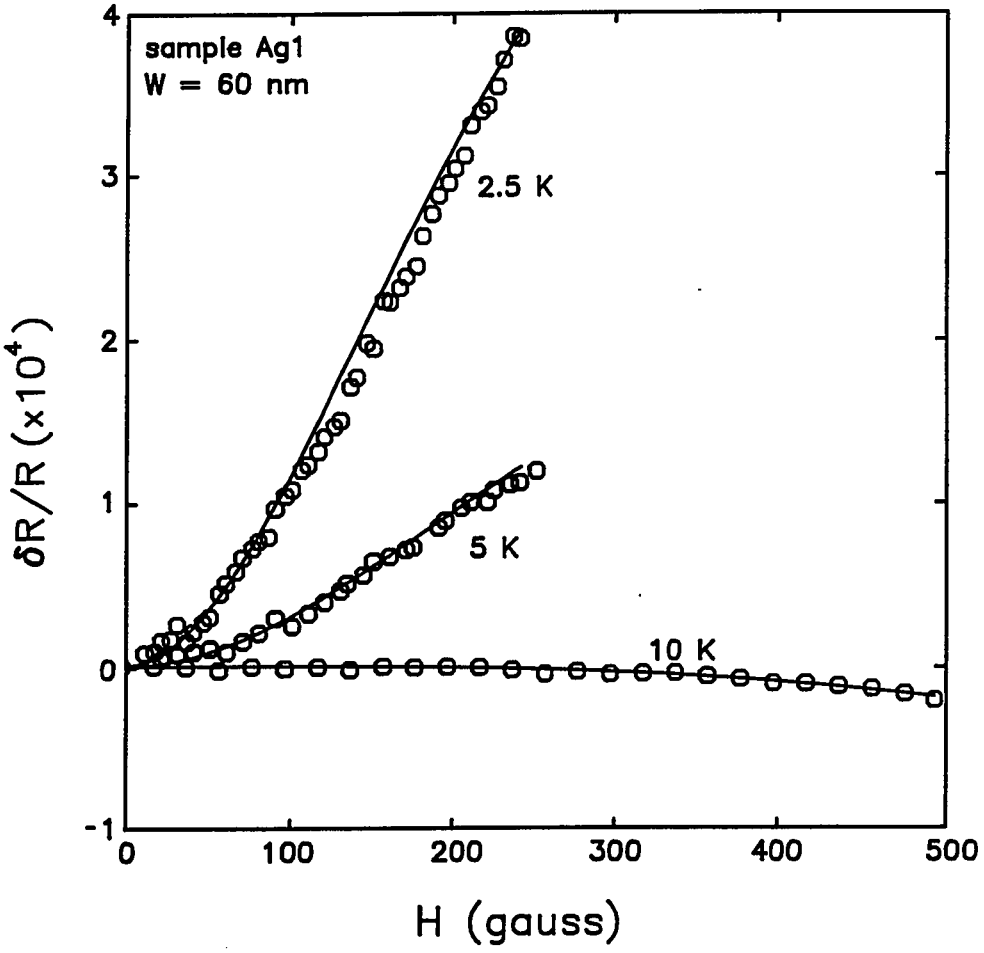

Fig. V-4. Normalized magnetoresistance for sample Ag1. ℓ_ϕ = 1.12 μm at 2.5 K, 0.63 μm at 5 K and 0.30 μm at 10 K. ℓ_{so} = 0.32 μm, and ℓ_s = 1.8 μm.

extension of the theory to higher fields [Gordon and Bindslev-Hansen, 1985] may eliminate the discrepancy. It should be emphasized that the observed discrepancy at fields higher than ~ 200 G had no effect on the inferred values of ℓ_ϕ, which were determined mainly from the low field portion of the magnetoresistance.

The normalized magnetoresistance for a silver wire, sample Ag1, of width 600 Å, is shown in Fig. V-4. Here, the theoretical curves fit to the experimental points consist only of the localization contribution with spin-orbit scattering. Initially, the fitting was done as described above, with ℓ_ϕ and ℓ_{so} used as fitting parameters. The inferred values of ℓ_ϕ from such a fit appeared to saturate at low temperatures. This was believed to be due to the presence of moderate magnetic scattering. Using the prescription given by Eq. (II-29) for the inclusion of magnetic scattering in the localization theory, the fitting was redone using ℓ_s as additional fitting parameter. Satisfactory fits were obtained with a constant value for ℓ_s at all temperatures. Not remarkably, this value was approximately twice the value at which ℓ_ϕ appeared to saturate when ℓ_s was not used as a fitting parameter, as might be expected from Eq. (II-29).

It is instructive to examine the relative magnitudes of the different contributions to the magnetoresistance. In Figs. V-5 - V-7, the theoretical fit to the experimentally determined magnetoresistance of sample Al2a at three different temperatures is decomposed into three parts: 1) the singlet term of the weak localization contribution, determined by ℓ_ϕ, 2) the triplet term, determined by $\ell_2 \simeq \ell_{so}$, and 3) the Maki-Thompson term, determined by ℓ_ϕ, but modified by the parameter $\beta(T/T_c)$. At temperatures not too far above T_c, as represented in Fig. V-5, the Maki-Thompson term makes the dominant contribution to the

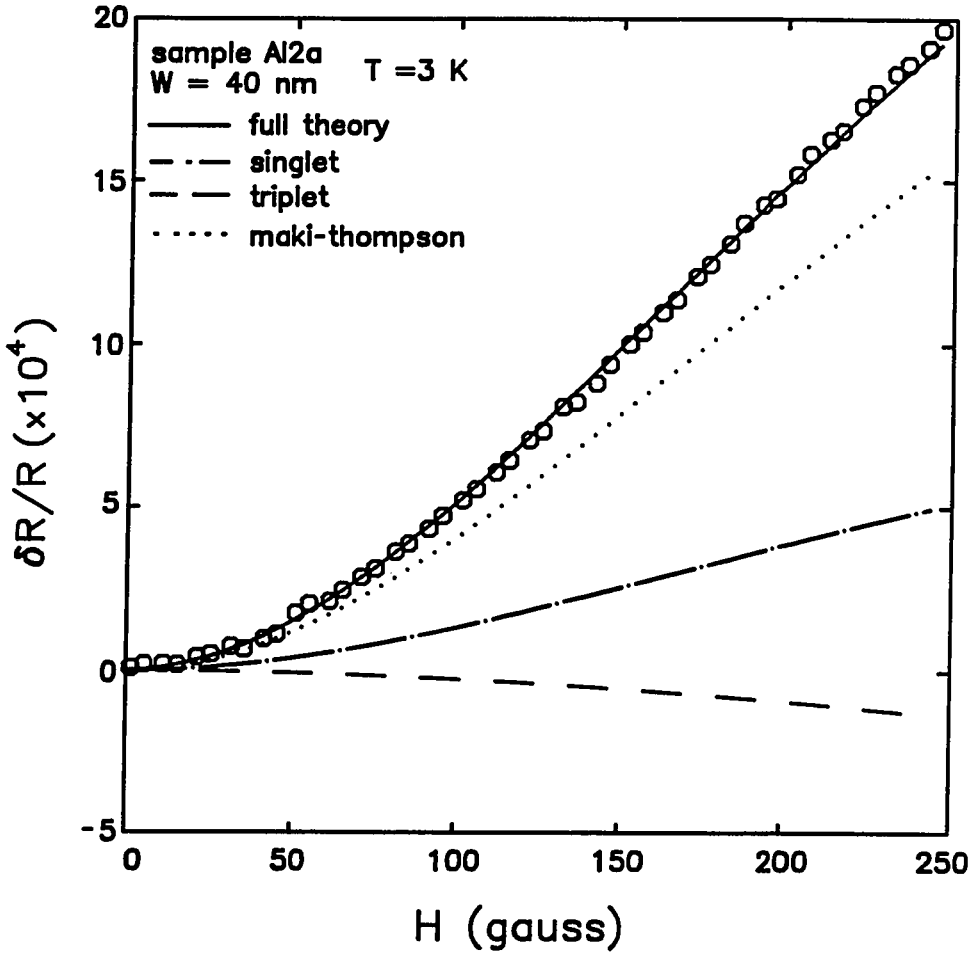

Fig. V-5. Normalized magnetoresistance for sample Al2a at 3 K. The theoretical fit is decomposed into separate contributions from the singlet term, the triplet term and Maki-Thompson fluctuations. Fiting parameters are the same as for Fig. V-2.

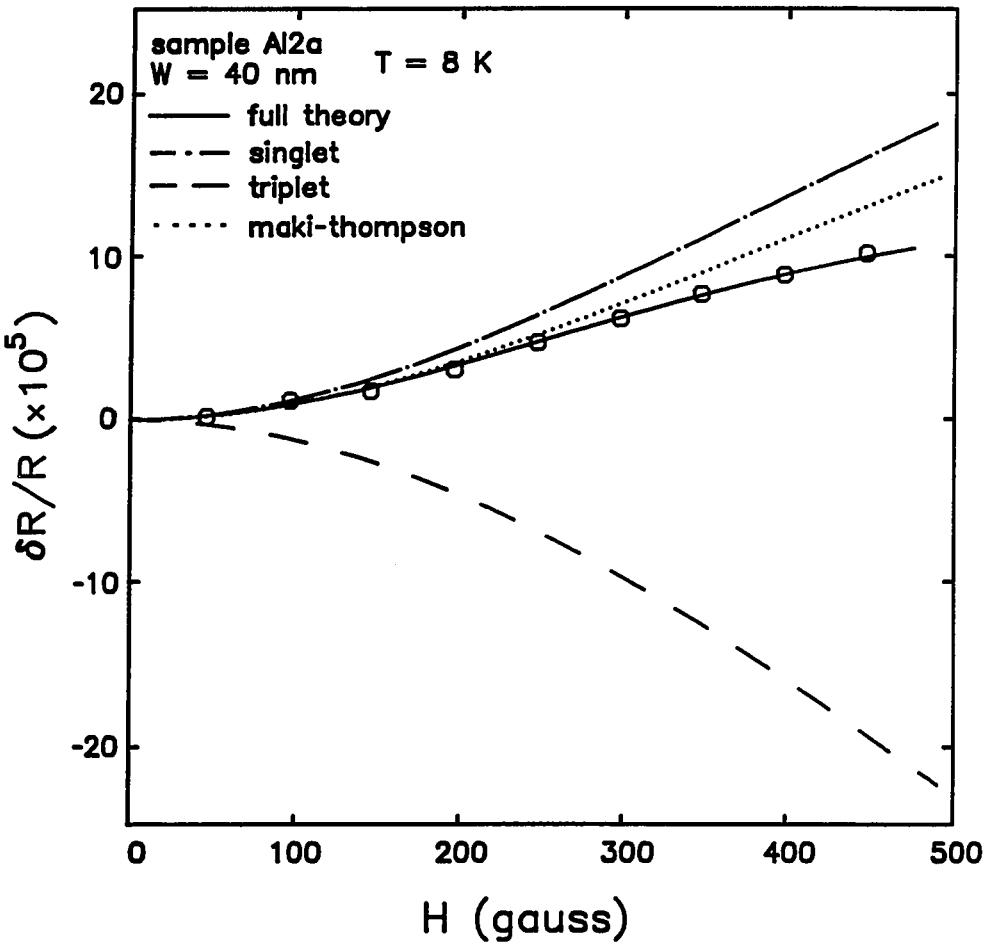

Fig. V-6. Normalized magnetoresistance for sample Al2a at 8 K, with the theoretical fit decomposed as in Fig. V-5.

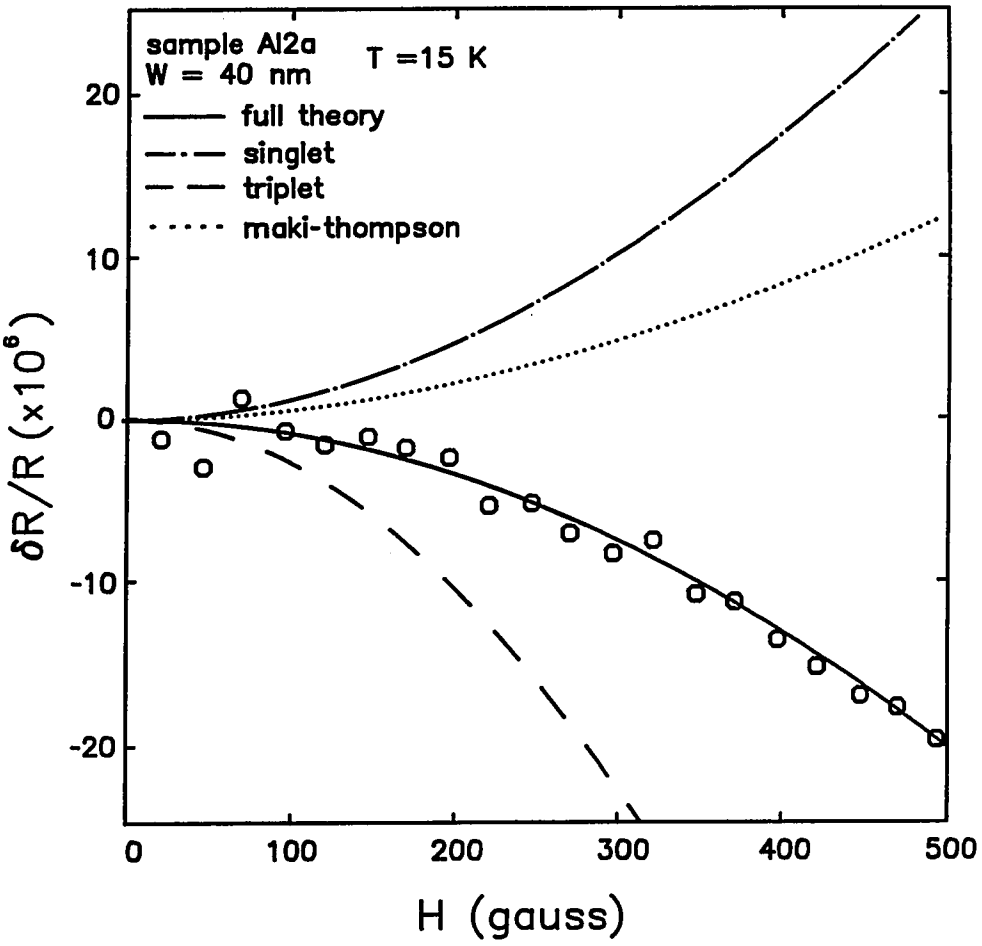

Fig. V-7. Normalized magnetoresistance for sample Al2a at 15 K, with the theoretical fit decomposed as in Fig. V-5.

magnetoresistance. Also, the singlet term is seen to be larger than the triplet. This is due to the fact that ℓ_ϕ (1.19 μm) is somewhat greater than $\ell_2 \propto \ell_{so}$ (0.57 μm). At intermediate temperatures (Fig. V-6), and at high temperatures (Fig. V-7), the triplet term is larger than the singlet, and it makes the dominant contribution to the magnetoresistance. Here, ℓ_ϕ and ℓ_{so} are of the same order of magnitude, and so the relative contributions of the singlet term and triplet term are determined by their prefactors [see Eq. (II-26)]. It is also noteworthy that the Maki-Thompson contribution is seen from Fig. V-7 to be significant even at 15 K, where β = 0.24.

We now turn our attention to a wider wire, sample Al7. The width of this sample was 4000 Å. Theoretical fits to the magnetoresistance at high temperatures (~ 15 - 20 K) using the two-dimensional localization theory (with 2D Maki-Thompson fluctuations) yielded reasonable values for ℓ_ϕ and ℓ_{so} that were both less than the wire width. At lower temperatures, where ℓ_ϕ is considerably longer, the data had to be analyzed using the mixed-dimensional theory, Eq. (II-28), since $\ell_2 < W < \ell_\phi$. As seen in Fig. V-8, the behavior of the sample at low temperatures is well-described by the mixed-dimensional theory, with the same value of ℓ_{so} as had been found at higher temperatures using the fully 2D theory. The fully one-dimensional theory did not provide as good a fit. At temperatures closer to T_c, both the mixed dimensional theory and the fully 1D theory yield satisfactory fits with the same values of ℓ_ϕ and ℓ_{so} because of the large contribution from 1D Maki-Thompson fluctuations. At intermediate temperatures, there was a range over which we were unable to fit the data with either the mixed-dimensional theory or the fully 2D theory, as seen in Fig. V-8. This range corresponds to the region of dimensional crossover from 1D behavior of the singlet term to 2D behavior when $\ell_\phi \sim W$. Experimentally, this range extended from ℓ_ϕ = 0.5 W to ℓ_ϕ = 1.3 W.

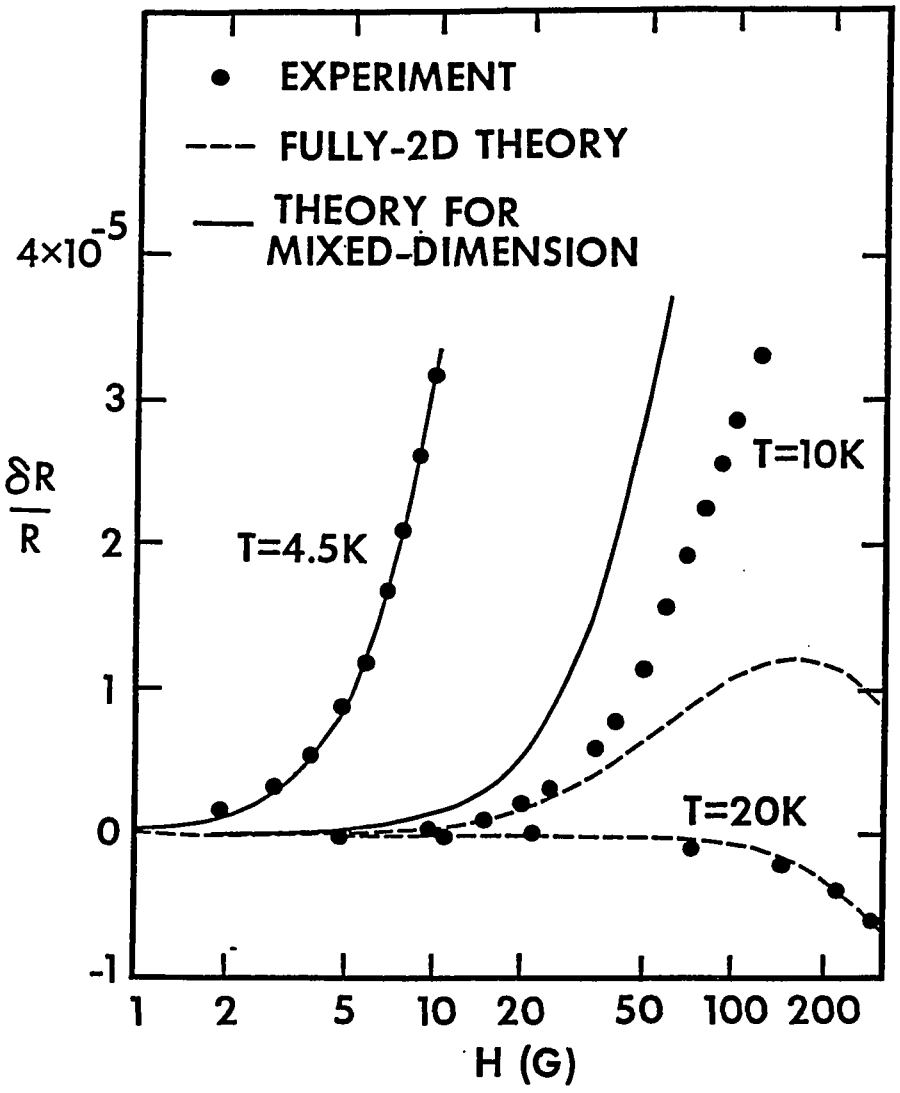

Fig. V-8. Normalized magnetoresistance for sample Al7, of width 4000 Å. At low temperatures, the experimental results are well described by the mixed-dimensional theory, with ℓ_ϕ = 0.78 μm at 4.5 K. At high temperatures, the 2D theory fits the data, with ℓ_ϕ = 0.17 μm at 20 K. At 10 K, neither the mixed-dimensional theory nor the 2D theory fit the data.

V.C. Magnetoresistance of Rings

The rings studied in this work were composed of either Al or Ag. They were of 1 or 2 μm diameter, with linewidths ranging between 1000 and 2300 Å and thicknesses ~ 200 Å. Essential sample properties are listed in Table V-2. The electrical measurements were performed using the four-terminal bridge arrangement described in Chap. III.

Fig. V-9 shows the magnetoresistance of sample R1, an Al ring 2.3 μm in diameter, at 1.7 K. Clear oscillations with a flux period of h/2e are seen. The magnetoresistance up to ~ 20 G can be fit using Eq. (II-30) from the theory of Altshuler et al. [1981c], with ℓ_ϕ = 1.7 μm. The inset in the figure shows the magnetoresistance of a similar Al ring, sample B, at high fields. Data for this ring are available at 4.5 K such that ℓ_ϕ can be determined by fitting either the low field oscillations or the high field envelope, where the oscillations are damped by the magnetic field. For this sample, $\ell_\phi \simeq 1.2$ μm at 4.5 K from the high field fit. The low field fits yield values of ℓ_ϕ that agree to within 20%. In general, values of ℓ_ϕ inferred from fitting Eq. (II-30) to the low field data are consistent with those obtained from measurements on 2D films and wider 1D wires in this work, since the linewidth of the rings was > ℓ_T.

h/2e oscillations in Al rings are observed up to ~ 8 K. At these temperatures, the contribution from superconducting fluctuations is minimal, so that these results are a clear confirmation of the predictions of Altshuler et al. [1984c] for normal metal rings.

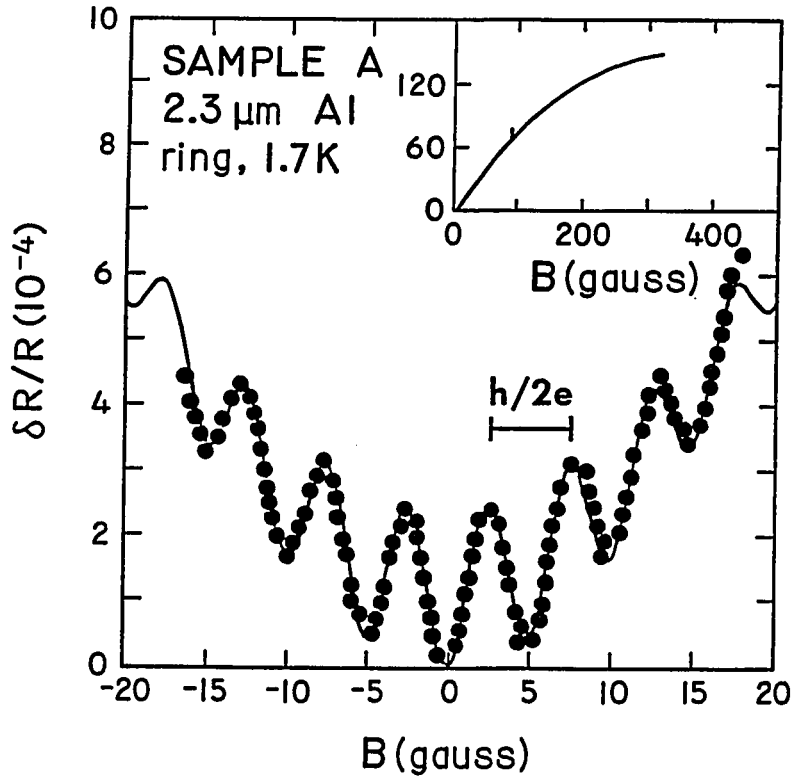

Fig. V-9. Magnetoresistance of sample R1, an Al ring of diameter 2.3 μm, at 1.7 K. The oscillations have a magnetic flux period of h/2e. The low field data is fit to the theory of Altshuler et al. The inset shows the data at higher fields, where the background magnetoresistance is determined by weak localization and Maki-Thompson superconducting fluctuations.

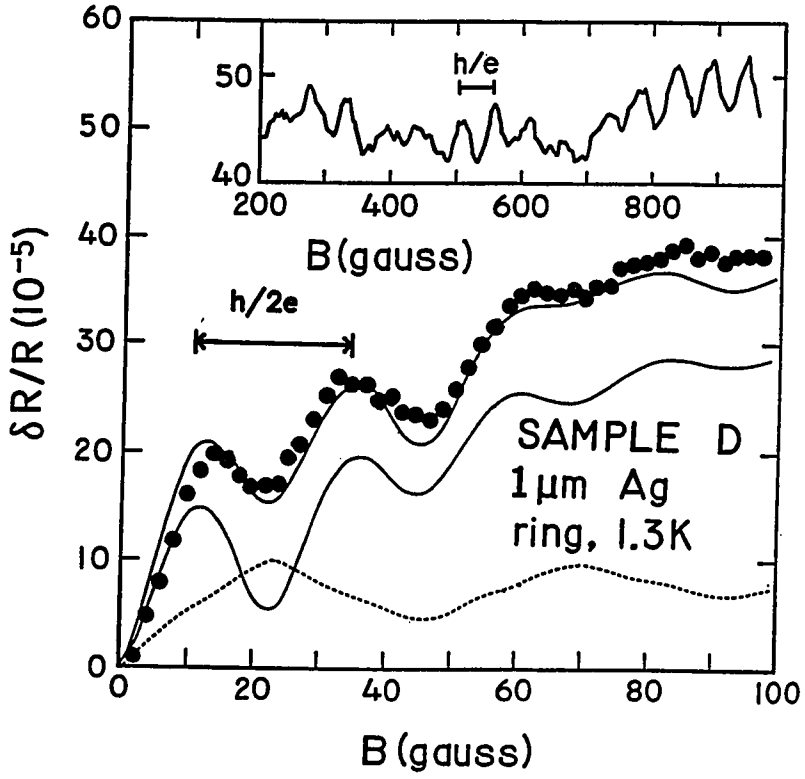

Fig. V-10. Magnetoresistance of sample R4, a 1 μm Ag ring. The low field magnetoresistance shows oscillations of period h/2e, while the oscillations at high fields have a period of h/e. The lower solid in the low field data is a fit to the theory of Altshuler et al. The dotted line is the h/e contribution, whose magnitude is estimated from the high field data. Combining these two lines gives the upper solid line.

We now turn our attention to the experiments on Ag rings. Fig. V-10 shows the magnetoresistance of sample R4, a 1 μm Ag ring at 1.3 K. Oscillations with a period of h/2e are clearly seen at low fields. At higher fields, oscillations with a period of h/e are observed, as shown in the inset. These oscillations persist to fields of at least 1 kG. The irregular structure at high fields is believed to be due to universal conductance fluctuations from the penetration of magnetic flux in the ring anulus [Lee and Stone, 1985]. The magnitudes of the h/e oscillations at high fields are about the same as the magnitude of the low field h/2e oscillations. The low field data cannot be satisfactorily fit with just the theory of Altshuler et al. However, by assuming that the h/e oscillations that are apparent at high magnetic fields are also present at low fields (shown by the dotted line in the figure), we are able to obtain a reasonable fit using Eq. (II-30). This, along with the data on Al rings, confirms the existence of the h/2e oscillations in individual rings, as predicted by Altshuler et al. The h/2e oscillations are observable in Ag rings up to 8 K, while the h/e oscillations can be seen up to 10 K.

The data in this work leave us with several unanswered questions. Perhaps the most puzzling issue is the apparent absence of h/e oscillations in the Al rings. Extensive careful measurements were made on a number of Al samples, and while a hint of h/e oscillations may be discerned with the use of some imagination, there is no clear evidence of their existence. In addition, the h/2e and h/e effects appear to have different dependences on magnetic field, as indicated by the results on the Ag rings, where the h/2e oscillations are damped by magnetic fields, while the h/e oscillations persist to very high fields. These results, together with the results of Webb et al. [1985], in which only h/e oscillations were observed in an individual Au ring, point to the need for a theoretical framework which incorporates both types of

oscillations and establishes the conditions for their observation. In the meantime, further experiments are being pursued at Yale [Chandrasekhar and Prober, 1987] which we hope will advance our understanding of these effects.

V.D. Electron Scattering Rates

The phase breaking rate, spin-orbit scattering rate and the magnetic scattering rate (for the Ag samples) can all be determined from the experimentally-inferred lengths via the relation $\tau_x^{-1} = D/\ell_x^2$, with x being substituted by the appropriate symbol, ϕ, so or s. This section will be devoted to an examination of these rates and the underlying mechanisms by which they are determined.

V.D.1. The Phase Breaking Rate

The rate associated with each electron scattering mechanism has its own signature in terms of magnitude, temperature dependence and $R_\square$ by which it may be identified, as was discussed in Sec. II.D. By a careful analysis of the behavior of τ_ϕ^{-1}, one should be able to determine the active scattering mechanisms in a given system.

Santhanam and Prober [1984] were the first to recognize for metal films that the total phase breaking rate may include contributions from several different mechanisms (Uren et al. [1981] found this to be the case for MOS systems). They found for their moderately clean ($R_\square \sim 1\ \Omega$) Al films that the phase breaking rate was best described by the following behavior:

$$\tau_\phi^{-1} = A_1 T + A_3 T^3 . \qquad \text{(V-4)}$$

A_1 and A_3 are fitting parameters used in a least squares fit of τ_ϕ^{-1} as a function of temperature. By comparing A_1 and A_3 with the theoretical predictions for the rates associated with different scattering mechanisms (Chap. II), Santhanam and Prober identified the rate in their films as being due to two-dimensional dirty limit electron-electron scattering and three-dimensional clean limit electron-phonon scattering, so that

$$\tau_\phi^{-1} = \tau_{ee}^{-1} + \tau_{ep}^{-1}.$$

Other investigators found similar results for thin films (see, e.g., [Santhanam et al., 1987; van Haesendonck et al., 1985; Altshuler and Aronov, 1985] for a more complete discussion). These results regarding the electron-electron contribution to the phase breaking rate are of particular interest, because they are, in fact, a confirmation of two different theoretical predictions. As discussed in Sec. II.D.1b, in two-dimensional disordered systems, the strongly inelastic electron-electron scattering rate, Eqs. (II-40) and (II-41), and the quasielastic rate, Eq. (II-55), have the same temperature dependence and approximately the same magnitude. The experimentally observed electron-electron rate may be ascribed to either mechanism or to a combination of both. In 1D samples, the quasielastic rate, Eq. (II-56), is predicted to be considerably larger than the strongly inelastic rate, Eq.(II-42). Thus, it is in 1D samples that the theoretical prediction for electron-electron scattering with small energy transfers can be most clearly tested.

The wires in this work fall into two regimes with respect to electron-electron scattering. Samples Al1 - Al3, Ag1 and Ag2 are all narrower than $\ell_T = (\hbar D/k_B T)^{1/2}$ at all temperatures where electron-electron scattering is dominant ($T \lesssim 6$ K).

Samples Al4 - Al7 are narrower than ℓ_ϕ at low temperatures but wider than ℓ_T.

Fig. V-11 shows the phase breaking rate as a function of temperature for several samples. The rates were determined from the phase coherence lengths inferred from fits to the magnetoresistance, as described in the previous section. The solid lines for the wires are fits[1] to the form

$$\tau_\phi^{-1} = A_{2/3}T^{2/3} + A_3T^3 , \qquad \text{(V-5)}$$

corresponding to a combination of one-dimensional electron-electron scattering with small energy transfers [Eq. (II-56)] and three-dimensional clean limit electron-phonon scattering [Eq. (II-58)]. (The rate predicted by Eq. (II-42) is two order of magnitude smaller than the measured rate.) The data for wire Ag2 from 2 to 4.5 K has been normalized to the $R_\square$ and D of the Al wires according to Eq. (II-56), to allow comparison with the results of the Al samples [i.e., the rate plotted for this wire is the measured rate times $(R_\square^{2/3}D^{1/3})_{Al}/(R_\square^{2/3}D^{1/3})_{Ag}$]. Included in the figure is the rate found in sample Al2F, a 2D film deposited along with the narrow wires. The data for this sample has been fit to the form $A_1T + A_3T^3$, and is consistent with the results on other 2D films (see above). As can be seen, all the fits are excellent. The fitting parameters are listed in Table V-3. The agreement between the fitting parameters and the theoretically predicted prefactor in Eq. (II-56) are also excellent. (Generally, in this field, when comparing measured and predicted rates, agreement to within a factor of 2 is considered satisfactory. The fact that the inferred values of $A_{2/3}$ in Table V-3 are closer to the theoretical values may not be of particular significance.) Also of great consequence is the fact that below ~ 6 K the magnitude

---

[1]The fitting was done using a Simplex algorithm [Caeci and Cacheris, 1984].

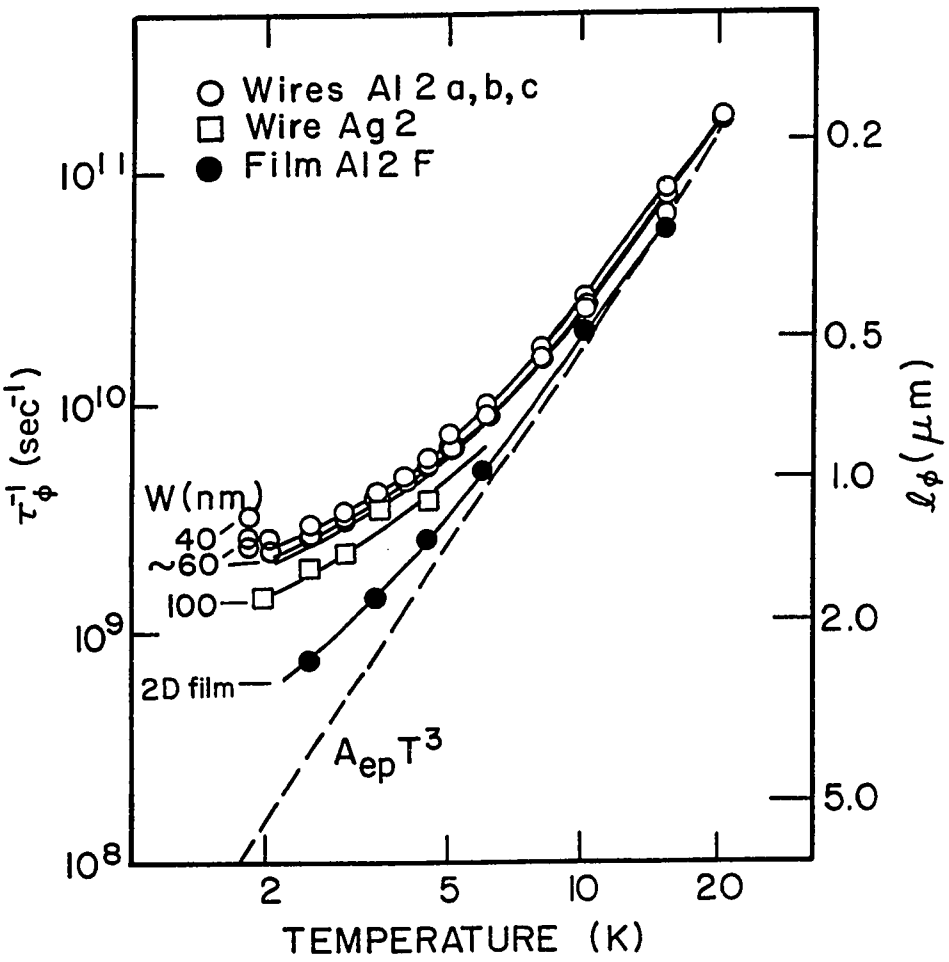

Fig. V-11. Phase breaking rate vs. temperature for wires of width < ℓ_T. The solid lines for the wires are fits by Eq. (V-5). The deviation of the Al data at T≤ 2 K is discussed in the text. The data for wire Ag2 (W = 1000 Å) from 2 to 4.5 K are normalized to the $R_\square$ and D of the Al samples according to Eq. (II-56) to allow comparison with results of the Al wires. The solid line for the 2D film is a fit by Eq. (V-4). The dashed line shows the electron-phonon scattering rate, $\propto T^3$. The scale for ℓ_ϕ applies for the Al samples only.

Table V-3

Fitting Parameters to Eq. (V-5) for Wires of Width < ℓ_T

Sample	$A_{2/3}^{Fit}$ ($10^9 K^{-2/3} sec^{-1}$)	$A_{2/3}^{Fit}/A_{2/3}^{Theory}$	A_3^{Fit} ($10^7 K^{-3} sec^{-1}$)	A_3^{Fit}/A_3^{Theory}
Al1a	1.79	1.02	1.98	2.20
Al1b	1.51	1.03	2.09	2.31
Al2a	1.36	0.94	2.39	2.64
Al2b	1.15	1.04	2.12	2.31
Al2c	1.43	1.32	2.13	2.34
Al3	0.74	1.11	1.99	2.20
Ag1	1.81	1.10	4.41	—
Ag2	1.03	1.06	2.24	—

$A_{2/3}^{Theory}$ refers to the coefficient of the temperature in Eq. (II-56). For the Al wires, $A_3^{Theory} = 0.91 \times 10^7\ K^{-3} sec^{-1}$, from Eq. (II-58). No such prediction currently exists for Ag.

of τ_ϕ^{-1} for the narrow wires is significantly greater than for the codeposited 2D film, with τ_ϕ^{-1} increasing as the wire width decreases.

At high temperatures, electron-phonon scattering dominates. It is essentially the same magnitude for the film and the wires. The coefficients A_3 determined from the fits are listed in Table V-3 as well. They agree reasonably well with the theoretically predicted coefficient in Eq. (II-58) and are consistent with previous studies [Santhanam and Prober, 1984; Gordon, 1984; Santhanam et al., 1984]. (It should be noted that Eq. (II-58) was calculated for the case of clean Al. No such calculation is available for Ag.) It should not be surprising that the electron-phonon scattering is three-dimensional in these wires, as the phonon wavelength, λ_p (see Sec. II.D.2), is less than both the film width and thickness at $T \gtrsim 6$ K, where electron-phonon scattering is significant.

An important further test of the 1D electron-electron theory is the width dependence at fixed temperature. This is shown in Fig. V-12 for three different temperatures. Here we have subtracted the electron-phonon scattering rate for each sample, $= A_3T^3$, and normalized the rate to the $R_\square$ and D of samples Al1, according to Eq. (II-56). All three groups of wires, Al1, Al2 and Al3, have similar material properties (Table V-1), so that such a comparison is sensible. The solid line corresponds to the theoretical magnitude and width dependence of the quasielastic scattering rate, τ_N^{-1}, taken directly from Eq. (II-56), with no adjustable parameters. The quantitative agreement is excellent. The predicted width dependence is seen clearly. These results are the first clear observation of the one-dimensional electron-electron scattering rate.

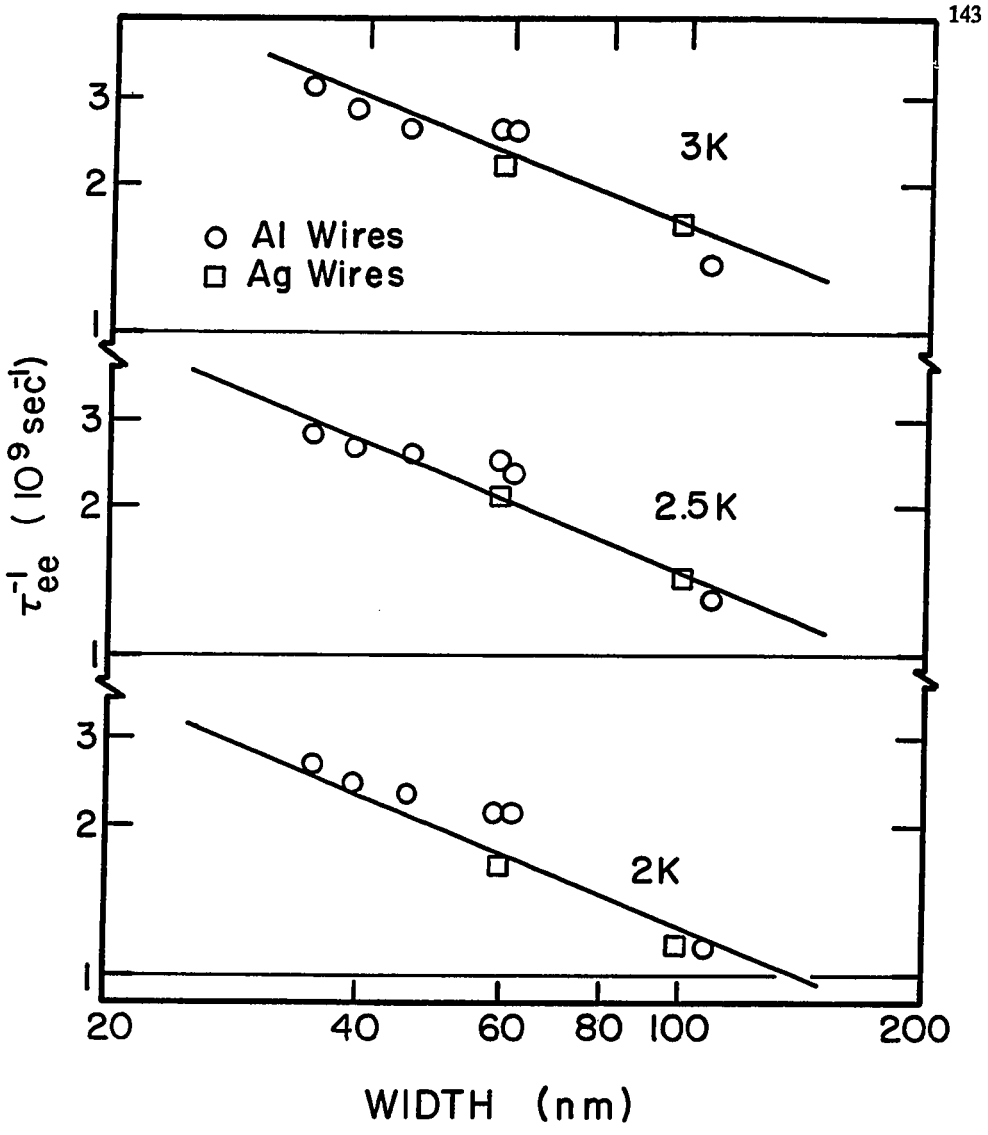

Fig. V-12. Electron-electron contribution to τ_ϕ^{-1} = [(total phase breaking rate) - (electron-phonon rate = $A_{ep}T^3$)] vs. wire width. The solid lines give the theoretical prediction of Eq. (II-56). The data are normalized to the $R_\square$ and D of samples Al2, according to Eq. (II-56).

There is an additional scattering mechanism which appears to be important for the Al wires at the lowest temperatures. It can be seen in Fig. V-11, that at ~ 2 K and below, τ_ϕ^{-1} increases slightly. This is apparently due to the scattering of electrons by superconducting fluctuations, τ_{ef}^{-1}, described in Sec. II.D.3. τ_{ef}^{-1} increases as T_c is approached from above. Unfortunately, the magnetoresistance measurements in this work did not extend sufficiently close to T_c to allow for a detailed study of this mechanism.

To contrast the results on the wires of width < 1000 Å, we turn our attention to the wider wires, samples Al4 - Al7. Fig. V-13 shows the inferred phase coherence length for wire Al4 (W = 2000 Å) as a function of temperature. Also shown in the figure is the length for the 2D film codeposited along with the narrow wire, indicated by the solid curve. As can be seen, the lengths for the wire and the film are nearly identical. The rates for these samples have been fit by Eq. (V-4). As seen from Table V-4, the fitting parameter A_1 agrees with the theoretical prediction for 2D electron-electron scattering as well as with the coefficients found for other 2D films. The electron-phonon scattering rate is also the same for the film and the wire. The reason for the close agreement of the phase breaking rate between the wire and its codeposited 2D film is that while the wire is one-dimensional with respect to localization (W < ℓ_ϕ), its width is still greater than ℓ_T, so that it is <u>two-dimensional</u> as far as electron-electron scattering is concerned. If somehow the wire were 1D regarding electron-electron scattering, then a clear difference would be seen between the rate in the wire and that in the film.

Recall from Sec. II.D.1 that in the theoretical derivation of the quasielastic

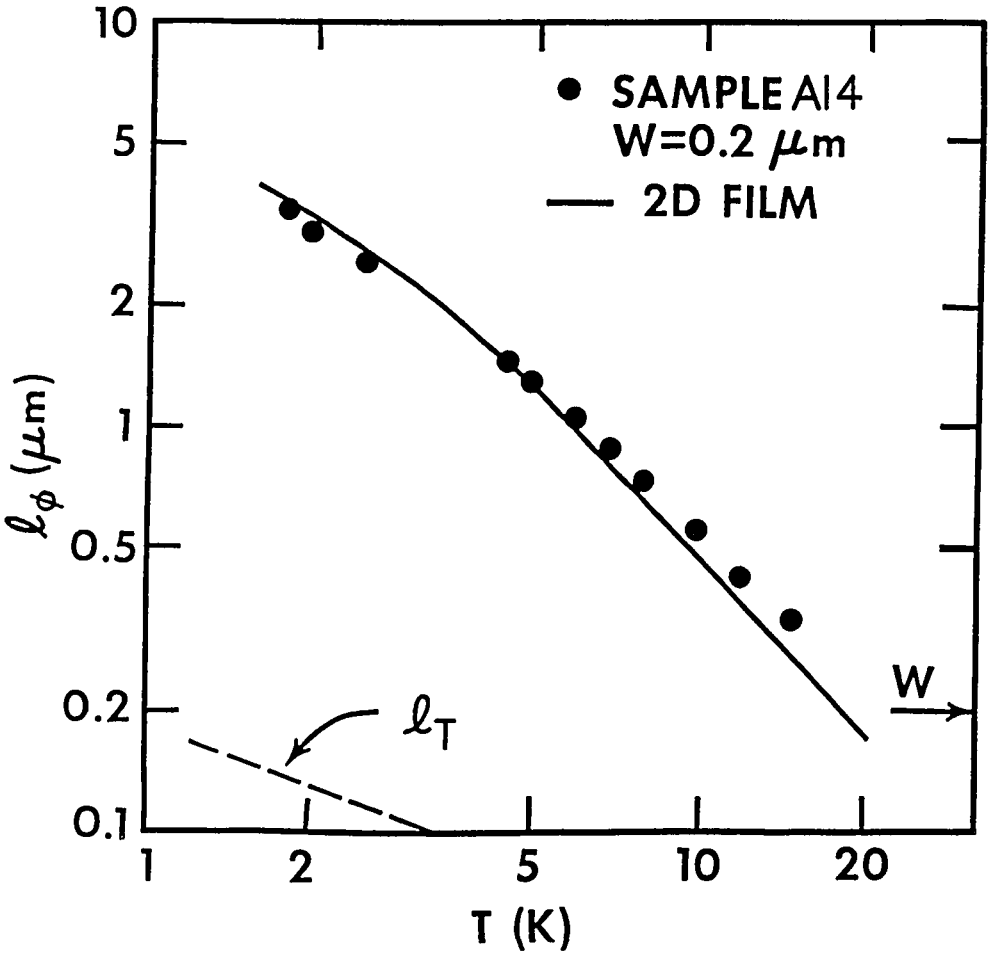

Fig. V-13. Phase coherence length vs. temperature for sample Al4. The solid line is ℓ_ϕ for the codeposited 2D film. The dashed line at the lower left shows ℓ_T as a function of temperature. W > ℓ_T throughout the measured temperature range.

Table V-4

Fitting Parameters to Eq. (V-4) for Wires of Width > ℓ_T

Sample	A_1^{Fit} ($10^8 K^{-1} sec^{-1}$)	A_1^{Fit}/A_1^{Theory}	A_3^{Fit} ($10^7 K^{-3} sec^{-1}$)	A_3^{Fit}/A_3^{Theory}
Al2Film	2.03	3.17	1.80	1.98
Al4	0.74	1.61	1.89	2.08
Al4Film	1.32	2.10	1.80	1.98
Al5	2.59	4.40	0.92	1.01
Al6	1.98	1.57	2.64	2.86
Al7	3.95	2.06	1.50	1.65
Al7Film	4.31	1.90	2.10	2.31

A_1^{Theory} refers to the coefficient of the temperature in Eq. (II-55). A_3^{Theory} = 0.91×10^7 $K^{-3} sec^{-1}$, from Eq. (II-58).

scattering rate [Altshuler et al., 1982a, and 1982b; Altshuler and Aronov, 1985] no explicit statement regarding the criteria for one-dimensionality is given. The results in this work, and in particular, a comparison of the rates in the wires of width less than ℓ_T with the rates of the wider wires clearly establishes that ℓ_T is apparently the correct dimensional length scale for quasielastic scattering as well as for all electron-electron processes.

V.D.2. The Spin-Orbit Scattering Rate

Values of the spin-orbit scattering length inferred from fits to the magnetoresistance data are listed in Table V-1. The spin-orbit scattering times in the Al samples can be compared to those obtained in other samples as well as to the theoretical model of Abrikosov and Gorkov [1962], which predicts that

$$\tau/\tau_{so} = (\alpha Z)^4, \qquad \text{(V-6)}$$

where τ is the elastic scattering time, α is the fine structure constant and Z is the atomic number of the metal. Eq. (V-6) predicts $\tau/\tau_{so} = 0.8 \times 10^{-4}$, using Z = 13 for Al. This behavior has been shown to be only qualitatively correct for moderately disordered Al films [Santhanam et al., 1987] when oxygen impurities (Z = 8) are taken as the primary source of elastic scattering. The results in this work are seen in Fig. V-14 to be consistent with this conclusion.

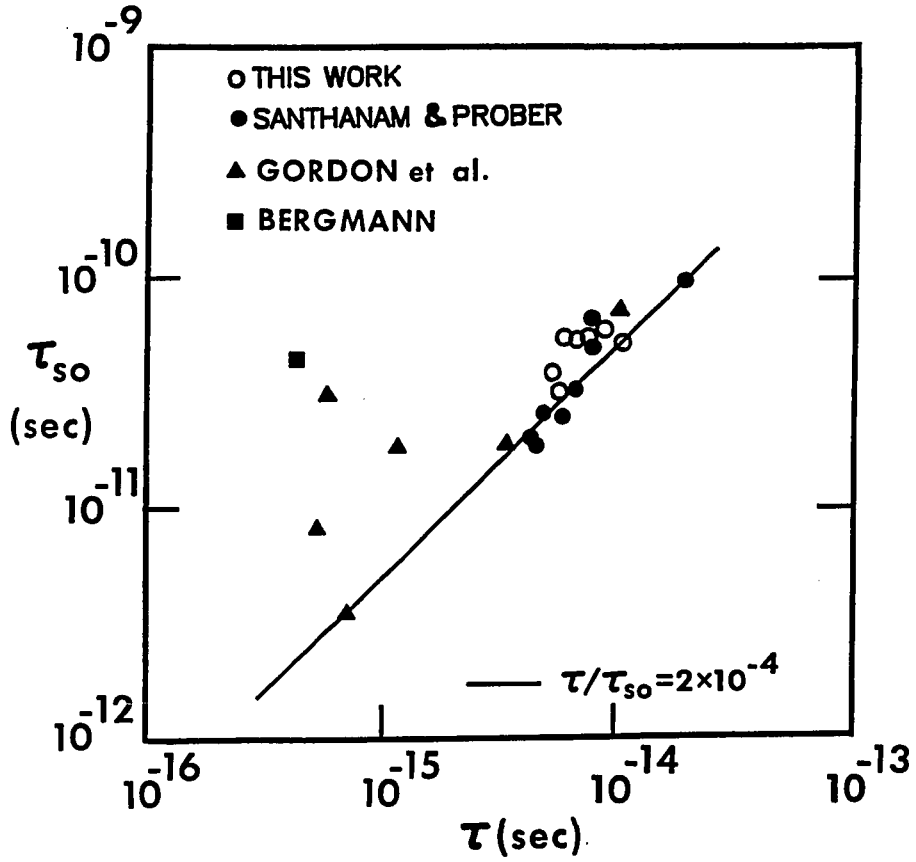

Fig. V-14. Spin-orbit scattering time in Al as a function of the elastic scattering time. The solid line corresponds to $\tau/\tau_{so} = 2 \times 10^{-4}$, in qualitative agreement with the theoretical prediction of Eq. (V-6).

VI. Comparison to Other Work

Soon after the initial prediction by Thouless [1977] that one-dimensional quantum interference effects coulds be observed in narrow metallic wires, experiments were undertaken to test that prediction. With further developments in the theory of quantum interference and electron-electron scattering (see Chap. II), experiments testing various aspects of these theories have continued to be pursued up until the present time. In this chapter, we will review the results on narrow wires obtained by other investigators. Attention will be given to studies of both quantum interference effects and electron scattering mechanisms.

VI.A. One-Dimensional Localization

The first experiments testing Thouless' theory were performed by Giordano et al. [1979]. They made narrow wires of Au-Pd with triangular cross sections using the edge defined technique described in Chap. III. Cross-sectional widths ranged from 300 Å to 2000 Å, and the samples had low temperature resistivities on the order of 100 $\mu\Omega$-cm. The wires displayed an increase in resistance as the temperature decreased. Also, the magnitude of the resistance rise was inversely proportional to the wire cross-sectional area, as would be expected for one-dimensional samples. This behavior was attributed to one-dimensional localization. However, as already mentioned in Secs. I.A and I.B, in order to explain the data in terms of Thouless' theory, very large electron phase breaking rates with a strange dependence on the sample resistivity ($\propto 1/\rho_o$) were required. No low field magnetoresistance measurements were made on these samples. However, the application of large fields [Giordano, 1980] did not significantly affect the resistance, and even the small

observed magnetoresistance did not depend on temperature.

In a similar study on e-beam defined W-Re wires of width 700 Å - 5000 Å and thickness ~ 50 Å [Chaudhari and Habermeier, 1980], the resistance rise with decreasing temperature was also interpreted in terms of localization theory. The inferred phase breaking rates appeared reasonable, agreeing with the rates determined from superconducting phase slip measurements on the same wires. They did observe a small magnetoresistance in both parallel and perpendicular fields, however, at the time of their experiments, no theory was available to account for magnetic field effects.

In a third study, White et al. [1982] fabricated clean (ρ_o ~ 1 $\mu\Omega$-cm) Cu wires on the edge of a step, with wire dimensions as small as 200 Å x 200 Å. They interpreted the resistance rise observed in their samples as being due mainly to electron-electron interaction effects [Altshuler et al., 1980], and not to localization. In addition, they reanalyzed the results of Giordano et al. and of Chaudhari and Habermeier in terms of the interaction theory and found good quantitative agreement.

As explained in Chap. II, a better theoretical understanding of the effects of spin-orbit scattering and magnetic scattering on quantum interference developed only after the initial experiments had been performed. This new understanding has helped shed light on those results, as we shall see below.

Measurements on 2D films of Au-Pd [McGinnes and Chaikin, 1985; Lin and Giordano, 1986], W-Re [Raffy et al., 1983] have indicated that these materials may exhibit large spin-orbit scattering rates as well as large magnetic scattering rates.

Results on Cu films [Abraham and Rosenbaum, 1983] show that large magnetic scattering effects may be present in Cu as well. The major contribution to the R(T) behavior of 2D films of these materials has been found to be due to interaction effects (see, e.g., [Kobayashi, 1985]). As far as the experiments on narrow wires mentioned above are concerned, with the large spin-orbit scattering rates in Au-Pd and W-Re, the wires studied were most likely in the mixed-dimensional regime with respect to localization effects, so that an interpretation of the data in terms of Thouless' theory was inappropriate. Strong magnetic scattering in those samples may have also reduced the overall magnitude of the localization effect, which was probably the case for the Cu wires of White et al. Thus, in all likelihood, the resistance rise with decreasing temperature observed in those experiments was due to electron-electron interaction effects, as suggested by White et al. Of course, this may not entirely explain all the experimental results. In the case of the Au-Pd wires, for example, the fractional resistance rise was proportional to ρ_o, while interaction theory [Altshuler et al., 1980] predicts a $\rho_o^{1/2}$ dependence. Further explanations may be required to account for all the results.

Two other studies attempting to observe localization effects in narrow wires apparently failed to do so. Sacharoff et al. [1984] measured drawn Pt wires of ~ 1000 Å diameter. They observed a very large resistance rise with decreasing temperature. The authors could not explain the data in terms of either 1D localization effects or electron-electron interactions. They did note that the samples showed a low-field magnetoresistance which was consistent with 3D localization theory, but this could not explain the zero-field results. The authors concluded that the observed effects were the result of the unusually large degree of disorder caused by the drawing process.

In another study, Overcash et al. [1980] observed a decrease in the resistance with decreasing temperature in single crystal Bi whiskers ~ 2000 Å in diameter formed by a stress accelerated growth technique. They concluded that there was no evidence of 1D localization. However, it may be that their experimental results may actually be an example of antilocalization, where the behavior is dominated by spin-orbit scattering, and a decrease in resistance with decreasing temperature is expected [Bergmann, 1984]. Low field magnetoresistance measurements could test this hypothesis.

There was one early study which did show clear evidence of one-dimensional localization effects. This was the work by Wheeler et al. [1982] on a 3000 Å wide wire formed in the inversion layer of a Si MOSFET. They observed a resistance rise with decreasing temperature which was consistent with a sum of interaction effects and 1D localization. In addition, the sample displayed a negative magnetoresistance which could succesfully be fit by the 1D localization theory without spin-orbit scattering. These results were confirmed by the behavior of a 2D sample fabricated along with the 1D wire. Skocpol et al. [1982 and 1983] observed effects consistent with the work of Wheeler et al.

Since the publication of the results of this work on one-dimensional localization [Santhanam et al., 1984b and 1985], there have been several studies which have confirmed certain aspects of the theory of quantum transport. Gordon [1984] and Gordon and Bindslev-Hansen [1985] performed magnetoresistance measurements on relatively clean Al wires of width ~ 0.5 μm. Their results were similar to our results on the wider wires (samples Al4 - Al7), however, they extended the measurements

closer to T_c, further testing the theory of superconducting fluctuations. In a novel study, Gordon and Goldman [1987] measured a Sierpinski gasket consisting of 0.3 μm wide Al wires. They adapted the localization and Maki-Thompson fluctuation theory to the framework of a fractal nework and found good agreement with their experimental results.

Licini et al. [1985] measured Li wires quenched condensed onto a liquid-He-cooled Si substrate. The wires were relatively clean ($\rho_o \sim 1$ $\mu\Omega$-cm) with widths ranging from $\sim$ 1 μm down to 300 Å. Their magnetoresistance showed clear agreement with the 1D weak localization theory with moderate spin-orbit and magnetic scattering. This, in fact, was the first 1D study to properly account for the effects of magnetic scattering and to confirm the generalizations of Eqs. (II-29a) and (II-29b). In another study on quench condensed Li wires, Bishop and Dolan [1986] demonstrated directly the dependence of the localization term on ℓ_ϕ by placing strips of Fe at set intervals along the Li wires. These Fe strips acted as strong magnetic scattering centers which caused the controlled dephasing of the electrons. Their results are a clear confirmation of the notions of Thouless [1977] regarding the length dependence of the 1D localization effect.

Lin and Giordano [1986] studied a Au-Pd wire fabricated by the step-edge technique. The authors analyzed the magnetoresistance data in terms of 1D localization theory up to 12 K, however, from the results of their analysis, it is not clear that their sample was actually in the 1D regime with respect to localization at all. The cross-sectional width of the wire was 460 Å, but the dimensional length scales for the singlet and triplet terms in Eq. (II-26) inferred from 1D fits to the data were only 300 Å and 100 Å, respectivley, at 5 K. Since these are less than the

wire width, it is an indication that perhaps the sample should be analyzed using the three-dimensional theory. In any case, we believe that the electron scattering rates inferred from the 1D fits to their data may not be reliable.

Other studies on one-dimensional localization effects in narrow wires include the works by Skocpol [1986] on Si MOSFET inversion layers, Choi et al. [1986] and Thornton et al. [1986] on wires formed in GaAs/AlGaAs heterostructures, and by Ishibashi et al. [1986] on a 400 Å wide Al wire. We will refer to these studies in the following section regarding their results on electron-electron scattering rates.

VI.B. Electron Scattering Rates

As mentioned in the previous section, the scattering rates found in the early 1D localization experiments could not be explained by any known theory of electron scattering. Of course, those rates are considered unreliable, as explained above, since they resulted from an analysis that did not include the complete 1D localization theory. However, those results did help to encourage further investigation into electron scattering mechanisms. They also established the standard that the scattering rates inferred from such quantum interference experiments should be understandable in terms of reasonable scattering mechanisms. In this section, we examine the results on scattering rates found by other investigators.

The scattering rates in Al wires studied by Gordon [1984] and Gordon and Goldman [1987] were found to agree most closely with the rates in this work. For wires wider than ℓ_T, the rates were determined by a combination of 2D dirty limit electron-electron scattering ($\propto$ T) and 3D clean limit electron-phonon scattering ($\propto$

T^3), with electron-fluctuation scattering becoming dominant at temperatures approaching T_c. In the fractal networks comprising wires of width less than ℓ_T, [Gordon et al., 1987] the 1D quasielastic electron-electron scattering rate ($\propto T^{2/3}$) was evident. The same 1D electron-electron rate was also reported for the 400 Å wide Al wire studied by Ishibashi et al. [1986]. The width dependence of the rate was not examined in these studies.

Measurements by Skocpol et al. [1983] and Skocpol [1986] on Si MOSFET inversion layers as narrow as 400 Å showed phase breaking rates which were proportional to T and which were in quantitative agreement with the 2D electron-electron scattering rates. This is reasonable, since for their devices, $W < \ell_T$ [Skocpol et al., 1986].

In the narrow GaAs/AlGaAs heterostructures (W = 0.2 μm and 0.3 μm) studied by Choi et al. [1986], the phase breaking rates were determined by a combination of 1D dirty limit electron-electron scattering with small energy transfers ($\propto T^{2/3}$) and large momentum transfer electron-electron scattering ($\propto T^2$), which was discussed in Sec. II.D.1. This rate is significant in these devices since they have a relatively low Fermi energy compared to metals. Although reasonable agreement with theory was observed for the 1D quasielastic rate in these samples, the magnitude of the coefficient of the T^2 rate ($\sim 8 \times 10^{10}$ $K^{-2}sec^{-1}$) was not consistent with the theory (1.3×10^{10} $K^{-2}sec^{-1}$) or with the 2D sample fabricated along with the wires (2×10^{10} $K^{-2}sec^{-1}$). Since this rate is not dependent on the degree of disorder in the sample, but rather on its bulk properties, such a discrepancy is rather surprising.

Thornton et al. [1986] measured a GaAs/AlGaAs heterostructure device to which

a "pinching voltage" was applied, which made the apparent width of the device (~ 500 Å) much less than the lithographically defined width. Although the phase breaking rate was not the main object of their study, they did note the observation of the 1D quasielastic electron-electron rate. We must point out, however, that the rate that they measured differed from the theoretically predicted rate by more than an order of magnitude.

Lin and Giordano [1986] claimed to have observed the 1D quasielastic electron-electron in the 460 Å wide Au-Pd wire. As discussed in the previous section, their extraction of the phase breaking rate using the 1D localization theory to analyze the data is somewhat questionable. We also point out that their sample showed very large magnetic scattering, which was the dominant contribution to the total phase breaking rate. In such circumstances, an unambiguous determination of the electron-electron portion of the phase breaking rate is tenuous [van Haesendonck et al., 1985]. In the case of this sample, a large difference in the inferred electron-electron scattering rate would have little effect on the total measured phase breaking rate. Furthermore, the wire width is greater than ℓ_T throughout the entire temperature range ($\ell_T \approx 180$ Å at 5 K), so that the wire was not clearly in the one-dimensional regime with respect to electron-electron scattering. We conclude that the study by Lin and Giordano does not unambiguously demonstrate the 1D electron-electron scattering rate.

In the work by Licini et al. [1985] on Li wires, a very strong scattering rate, $\tau_\phi^{-1} \sim 7 \times 10^9\ T^2$ was observed. This rate is considerably larger than could be accounted for by the large momentum transfer rate [Eq. (II-39)] for Li, as noted by the authors. It is also sufficiently large to prevent the observation of rates due to

other mechanisms such as clean limit electron-phonon scattering and dirty limit electron-electron scattering. It may be that the mechanism responsible for this rate is peculiar to the type of disorder present in quench condensed films. We note that a rate with a T^2 dependence and a similar magnitude was also observed in 2D quench condensed Al and Mg films by Bergmann [1984].

VII. Summary and Conclusions

VII.A. Quantum Interference Phenomena

Following Thouless' original prediction of the one-dimensional localization effect [Thouless, 1977], it appeared that the observation of this effect would be relatively straightforward, albeit experimentally demanding. A conceptually simple measurement of the resistance as a function of temperature would be all that is necessary to demonstrate this startling effect. Advances in the theory of quantum transport have shown that for most real metals, the situation is far more complex. Aside from the competing contribution to the resistance as a function of temperature from electron-electron interaction effects, spin-orbit scattering and magnetic scattering make the conditions for one-dimensionality with respect to localization more difficult to satisfy. It had been thought that a sample would show one-dimensional behavior if its lateral dimensions were less than ℓ_ϕ, the phase breaking length. We now know that ℓ_{so} and ℓ_s, the lengths for spin-orbit and magnetic scattering, also play a role as dimensional length scales. Although the early localization experiments did appear to verify Thouless' predictions, these experiments were testing an incomplete theory as far as their samples were concerned, and apparently did not fall in the 1D localization regime.

It took a number of years for the theory of weak localization to mature and to establish correct guidelines for experimentalists to observe one-dimensional effects. The important features of those guidelines include the predictions for the low field magnetoresistance, which allows localization effects to be isolated from interaction effects, and the inclusion of spin-orbit scattering and magnetic scattering in the

theory. These refinements of the theory should not be viewed as complications, since along with their explication came a better intuitive understanding of the physics of quantum interference (see, e.g., [Bergmann, 1984] or [Khmelnitskii, 1984]) in terms of time-reversed trajectories.

As part of this work, we have confirmed in detail the predictions of the complete theory of weak localization for one-dimensional metallic systems. We have also observed the existence of an intermediate size regime - the regime of mixed dimensionality - in which the singlet term in the localization contribution is one-dimensional while the triplet term (the term sensitive to spin-orbit scattering) is two-dimensional. We have also observed a dimensional crossover from two- to one-dimensional behavior. Aside from the good agreement between the experimental data and the 1D theory, the inferred scattering lengths confirmed self-consistently that the experiments were in the one-dimensional regime of the theory. When the inferred phase coherence length and spin-orbit scattering length are less than the sample width, the fully 1D theory gives a good description of the data. When $\ell_{so} < W < \ell_{\phi}$, the mixed dimensional theory is seen to be most appropriate. For the sample in which a dimensional crossover was observed, when $W \propto \ell_{\phi}$, neither the 1D (or mixed) theory nor the 2D theory could fit the data using any reasonable fitting parameters. We have also confirmed the theory regarding one-dimensional Maki-Thompson superconducting fluctuations and found that ℓ_{ϕ} is indeed the dimensional length scale deciding dimensionality for this effect.

The phase breaking rates determined from the experiments on narrow wires also served as a central focus of this work. We found that for the wires of width greater than ℓ_T, the phase breaking rate is determined by a combination of two-

dimensional dirty limit electron-electron scattering and three-dimensional clean limit electron-phonon scattering. The phase breaking rate in the wires studied of width $\gtrsim$ 0.2 μm is identical to the rate found in the codeposited two-dimensional films. For the electron-electron scattering rate, it is impossible from the data to distinguish between the strongly inelastic scattering rate predicted by Abrahams et al. [1981] and the rate due to the scattering of electron by electromagnetic fluctuations (quasielastic scattering). For the wires which are narrower than ℓ_T, the electron-electron portion of the phase breaking rate is clearly due to one-dimensional scattering with small energy transfers (quasielastic scattering). We have confirmed the theoretical predictions for this rate with respect to its magnitude, temperature dependence and width dependence. We have also established experimentally that ℓ_T is the dimensional length scale for this scattering mechanism. This work is the first to make a clear identification of this rate in narrow wires.

Another aspect of quantum interference addressed in this work is the Aharonov-Bohm effect in small metal rings. We have observed oscillations with a period of h/2e in Al and Ag rings at low magnetic fields. These confirm the theory of Altshuler et al. [1981c] for the interference due to time-reversed paths. Oscillations with a period of h/e were observed in Ag rings, as predicted by Buttiker et al. [1985], but were apparently absent in the Al rings. A theoretical framework is needed which will account for both types of oscillations and will determine clearly the length scales for each.

Very recent experimental work by Chandrasekhar and Prober [1987] has addressed some of these issues. They have analyzed the high field magnetoresistance data of a 1 μm Al ring. The autocorrelation function over a magnetic field range of

a few hundred gauss reveals the presence of oscillations of period h/e. These oscillations cannot easily be discerned directly from the magnetoresistance, or from the Fourier transform of the magnetoresistance, since their amplitude is not much larger than the noise in the data. The autocorrelation function essentially filters out the aperiodic noise, so that the h/e oscillations can be seen clearly. The amplitude of these oscillations, as determined from the Fourier transform power spectrum, agrees with the value predicted by Stone and Imry [1986].

Further experiments by Chandrasekhar and Prober on Ag rings have also revealed a fundamental difference between the h/2e oscillations and the h/e oscillations. They found that a controlled amount of magnetic impurities on the ring"s surface destroyed the h/2e oscillations, while it did not affect the h/e oscillations. This indicates that there may be different characteristic length scales for these two effects.

VII.B. Microlithography

The samples studied in this work were fabricated using either x-ray or electron-beam lithography. The x-ray masks were patterned using a novel three-dimensional technique, in which the gold x-ray absorber was deposited at an angle across a step in the polyimide x-ray mask membrane. The limit on the resolution of this technique appears to be set by the stretching of the polyimide membrane. The e-beam and x-ray lithography schemes used in this work employed a thin bilayer e-beam resist. This resist system was found to offer high resolution with good exposure latitude and good control over the linewidth. The liftoff properties of this bilayer were also found to be excellent, which was particularly important for the

samples studied in our work. The wires fabricated for this work were among the smallest produced by "conventional" lithography techniques, using only modest equipment.

VII.C. Reflections on Future Work

While the experiments reported in this work have verified some of the important features of the theory of quantum interference and transport, they do point to some issues which should be addressed in the future. The most obvious issue involves the Aharonov-Bohm effect in rings. An understanding of both the h/e and the h/2e effects must be reached within a unified theoretical framework. Also, we look for an explanation for the absence of h/e oscillations in Al rings and the absence of h/2e oscillations in the Au ring studied by Webb et al. [1985].

The localization studies on narrow wires also leave some interesting topics for future research. We have found that the spin-orbit scattering rates in our Al wires are consistent with those found in other Al samples. They agree qualitatively with a theoretical model of spin-orbit scattering due to the presence of impurities [Abrikosov and Gorkov, 1962], however, the quantitative agreement is unsatisfactory. Investigation of the precise mechanisms which are responsible for spin-orbit scattering is warranted. Similarly, magnetic scattering is not well understood at present. Recent experiments on two-dimensional films [Bergmann, 1986] studying the screening of magnetic impurities incorporated into the film versus those deposited on the film surface may offer some interesting insight. Also, weak localization measurements on Kondo systems [Gijs et al., 1986] may shed light on the nature of magnetic scattering, as well as improve our understanding of those types of systems.

The experiments in this work as well as similar experiments up until the present time have dealt with electrons very close to the Fermi level at low temperatures. Recently, some new devices have received some attention in which the electron energies are far above the Fermi level. An example of such devices is the hot electron transistor [Heiblum et al., 1985]. It would be desirable to bridge the gap between the two energy and temperature regimes, so that the techniques used to study the types of samples in this work may be applied to new devices and structures.

Appendix A

Preparation of X-ray Masks

The process for preparing x-ray masks involves the following steps:

1- Cleaning of the glass substrate

2- Preparation of the polyimide mask membrane film

3- Preparation of the photoresist for the formation of the chromium etch mask

4- Exposure and development of the photoresist

5- Deposition of the chromium etch mask and liftoff

6- Formation of steps in the polyimide film by reactive ion etching

7- Angle deposition of the gold x-ray absorber

8- Removal of the glass substrate

9- Bonding of the polyimide membrane to the Vespel mask support ring

10- Deposition of aluminum for electrostatic holddown

Details of these steps are given in this appendix:

A-1 Cleaning of the Glass Substrate

Corning #$1^1/_2$ coverglass slides (18 mm x 18 mm x 0.2 mm) are used as substrates to support the x-ray mask membrane until after patterning is completed. The coverslips are cleaned according to the following procedure:

(a) Ultrasonic agitation in acetone for 2 minutes.

(b) Rinse in acetone from spray bottle.

(c) Ultrasonic agitation in isopropyl alcohol for 2 minutes.

(d) Rinse in isopropyl alcohol from spray bottle.

(e) Blow dry with high purity nitrogen gas.

A-2 Preparation of the Polyimide Film

The polyimide is prepared from a 1:1 or 3:2 filtered solution of polyamic acid (DuPont product PI2550) in N-Methyl-pyrollidone (polyimide thinner). It may be stored for long term use in a freezer. Its shelf life is not known.

(a) The cover glass is centered on the vacuum chuck of a standard photoresist spinner.

(b) The polyamic solution is dropped from a glass pipette onto the center of the cover slip until it runs out to the edges. It should be allowed to sit for ~ 60 seconds before spinning to prevent the formation of bubbles in the film.

(c) Typical spin speeds are 3000 rpm for 120 seconds with the 1:1 solution for a thickness of ~ 1 μm and 2500 rpm for 120 seconds with the 3:2 solution for a thickness of ~ 1.5 μm.

(d) Following spinning, the sample is baked at 300 °C for 60 minutes on a hot plate.

A-3 Preparation of the Photoresist for Mask Patterning

(a) Following the curing of the polyimide film, the sample is allowed to cool.

(b) The sample is centered on the vacuum chuck of the photoresist spinner.

(c) The spinner is turned on and AZ-1350B photoresist (filtered down to 0.2 μm) is dropped onto the sample as it is spinning (dynamic flooding). Spinning proceeds for 45 seconds. Spin speed is 6000 rpm for a 5000 Å thick layer.

(d) The photoresist is baked on a hot plate at 90 °C for 20 minutes.

A-4 Exposure of the Photoresist Pattern

(a) Contact exposures are made using an unfiltered 100 Watt high pressure mercury

vapor arc lamp. Typical exposure time is 30 seconds. The mask is chromium on glass. Mask to substrate contact is ensured by vacuum chucking.

(b) Projection exposures are done in a Carl Zeiss photomicroscope. The mask consists of a triangle formed from the edges of razor blades. Two illumination sources are available. With a type II-C epi-illuminator using a 15 Watt tungsten lamp, exposures are done with the 40x Aufl Pol achromatic lens by projecting through the rear of the cover glass. A green low pass filter (Corning type CS2-60) is used for focusing and alignment. A blue filter with a transmittance peak at 4000 Å (Corning type CS5-58) is used during exposure. Typical exposure time with this source is 45 seconds. The second source is a 50 Watt Zeiss mercury vapor lamp. Exposures are done with the 40x Epiplan lens onto the front surface of the substrate. Exposure time is ~ 4 seconds.

(c) The photoresist is developed in Shipley AZ developer diluted 1:1 with deionized water. Developing time is 30 seconds at 21 °C.

(d) The sample is then rinsed in deionized water for 1 minute and blown dry with high purity nitrogen gas.

A-5 Deposition of the Chromium Etch Mask

(a) Chromium is deposited by thermal evaporation from a chromium-plated tungsten rod (R. D. Mathis Co.). Typically, ~ 100 Å are deposited at a rate of ~ 10 Å/sec at a pressure of ~ 1×10^{-6} torr.

(b) Following deposition, the sample is soaked in acetone for 30 seconds with ultrasonic agitation, and the unwanted chromium is lifted off.

(c) The sample is rinsed in acetone and blown dry with nitrogen gas.

A-6 Reactive Ion Etching (RIE) of the Polyimide

(a) Prior to the etching of the samples, the RIE chamber undergoes an O_2 preclean for 10 minutes to rid the system of any contaminants.

(b) Following the preclean, the samples are loaded into the RIE chamber. The chamber is flushed with nitrogen gas as it is exposed to atmosphere.

(c) The chamber is evacuated to a pressure of less than 1×10^{-5} torr before the etch gas is introduced into the chamber. Typical etch gas pressure is 3.5 millitorr with a flow rate of ~ 7 sccm.

(d) The samples are etched in 100% O_2 for 150 seconds. J head self bias is -450 V at 25 Watts.

A-7 Angle Deposition of the Gold Absorber

(a) Following RIE, thin strips of AZ1350B photoresist are painted onto the polyimide film between the chromium triangles with a fine artist's brush. This helps prevent the tearing of the gold absorber due to film stress in the gold absorber.

(b) A metal slot mask is placed against the sample and is aligned so that the 220 μm wide slot runs perpendicular to the edges of the etched triangles (see Fig. III-7). The mask is held down by set screws.

(c) The sample is mounted in the evaporation chamber at a given angle so that the gold is deposited across the etched steps.

(d) A tungsten rod wrapped with gold wire is aligned in the evaporator so that it lies directly beneath the sample and runs perpendicular to the slot in the metal mask. The chromium evaporation source is placed directly next to the gold source.

(e) 50 Å of chromium are deposited directly prior to the gold deposition.

(f) ~ 1000 Å of gold are deposited at a rate of ~ 5 Å/sec. Chamber pressure during deposition may range from 1×10^{-6} to 1×10^{-5}.

(g) Following the gold deposition, the metal slot mask is removed and the stress

relief gaps are formed by soaking the sample in acetone to dissolve the painted-on photoresist.

A-8 Removal of the Glass Substrate

(a) The polyimide side of the sample is bonded to a brass cylinder with Devcon 5-minute epoxy.

(b) Black sealing wax is applied around the edges of the cylinder to ensure that acid cannot seep through pinholes in the epoxy.

(c) The end of the cylinder bonded to the sample is placed in a 1:1 solution of concentrated hydrofluoric acid and deionized water. A small amount of isopropyl alcohol is poured into the cylinder to provide positive pressure. The etching is done in a vented fume hood.

(d) After etching for ~ 30 minutes, the sample is removed from the acid solution and is rinsed in deionized water followed by a rinse in isopropyl alcohol. It is then carefully blown dry with high purity nitrogen gas.

(e) To check that all the glass has been removed, a few drops of deionized water are dropped onto the sample. If the water beads up, the glass has been completely etched away. If the water runs on the surface of the sample, the sample must be immersed in the acid solution until the etching is complete.

A-9 Bonding to the Vespel Ring

At this point, the polyimide film is stretched across the end of the cylinder. Extreme care must be taken not to puncture the ~ 1 μm thick membrane.

(a) Tracon 2555 epoxy is applied to the beveled side of a Vespel ring.

(b) The ring is carefully placed on the polyimide membrane. Slight pressure may be applied to ensure good contact.

(c) The ring is covered with some glass microscope slides, and the epoxy is allowed

to cure for 18 hours.

(d) The mask is removed from the brass cylinder by carefully cutting the polyimide film with a scalpel outside the Vespel ring. The ring may be grasped on the outside with tweezers. Extreme care must be used, as the polyimide membrane is highly delicate.

A-10 Deposition of Aluminum for Electrostatic Holddown

(a) The mask is mounted in a special holder which has a hole in it to prevent physical contact with the polyimide surface.

(b) About 400 Å of aluminum are deposited by thermal evaporation onto the back surface of the mask.

(c) A small amount of silver paint may be dabbed onto the Vespel ring to aid electrical contact between the aluminum film and the metal clips on the copper flange which holds the mask during x-ray exposure (Fig. III-11).

Appendix B

Estimate of the One-Dimensional Aslamazov-Larkin Contribution to the Resistance in a Magnetic Field[1]

The increased conductivity due to the acceleration of fluctuation-paired electrons in an applied magnetic field is estimated to be [Tinkham, 1975]

$$\Delta\sigma_{AL} = \frac{(2e)^2}{m^*} \sum_q \frac{<|\psi_q|^2> \tau_q}{2} \quad , \tag{B-1}$$

with ψ the superconducting order parameter, and τ_q the decay time of the superconducting modes. Using Tinkham's Eqs. (7-27) and (7-48) for $<|\psi_q|>^2$ and τ_q:

$$<|\psi_q|^2> = \frac{2m^*\xi^2}{\hbar} \frac{k_B T}{(1 + \xi^2 q^2)} \tag{B-2a}$$

and

$$\tau_q = \frac{\tau_{GL}}{(1 + \xi^2 q^2)} = \frac{\pi\hbar}{16 k_B (T - T_c)} \frac{1}{(1 + \xi^2 q^2)} \, . \tag{B-2b}$$

with τ_{GL} the decay time of the q = 0 mode ξ the temperature dependent Ginsburg Landau coherence length, we have for the excess conductivity

$$\Delta\sigma_{AL} = \frac{\pi e^2 \, T\xi^2}{2\hbar \, (T - T_c)} \sum_q \frac{1}{(1 + \xi^2 q^2)} \, . \tag{B-3}$$

---

[1]The calculations in this Appendix are the result of work by Santhanam [private communication].

For a narrow wire of width and thickness << $\xi(T)$, this becomes

$$\Delta\sigma_{AL} = \frac{\pi e^2 T}{2\hbar (T - T_c)} \frac{L}{2\pi\xi^2} \int \frac{dq}{(q_x^2 + \xi^{-2})^2} , \qquad (B\text{-}4)$$

with L the sample length. The application of a magnetic field, H, is dealt with as in the case of the Cooperon (Sec. II.C.1), so that the denominator of the integrand becomes

$$q_x^2 + \left[\frac{2eH}{\hbar c} \right]^2 \frac{W^2}{12} + \frac{1}{\xi^2} . \qquad (B\text{-}5)$$

Then,

$$\frac{\Delta\sigma_{AL}}{L} = \frac{e^2 T}{4\hbar (T - T_c) \xi^2} \int \frac{dq_x}{[q_x^2 + (2eH/\hbar c)^2 + \xi^{-2}]} . \qquad (B\text{-}6)$$

Evaluation of the integral yields for the conductivity per unit length

$$\Delta\sigma_{AL} = \frac{\pi e^2 T}{16\hbar (T - T_c)\xi^2} \left[\frac{1}{\xi^2} + \left[\frac{2eH}{\hbar c} \right]^2 \frac{W^2}{12} \right]^{-3/2} . \qquad (B\text{-}7)$$

The fractional change in resistance is related to the conductivity per unit length as in Eq. (II-23a), so that

$$\frac{\Delta R}{R} = -\frac{\Delta\sigma_{AL}}{L}\frac{R}{}$$

$$= -\frac{\pi R_{\square}\, T}{16(\hbar/e^2)W\,(T - T_c)\,\xi^2}\left[\frac{1}{\xi^2} + \left[\frac{2eH}{\hbar c}\right]^2\frac{W^2}{12}\right]^{-3/2} . \qquad \text{(B-8)}$$

This result should be valid only for small magnetic fields, $H << (ck_BT/4De)\ln(T/T_c)$. When $T >> T_c$, but $W << \xi(T) = [\xi^2(0)/\ln(T/T_c)]^{1/2}$, Eq. (B-8) becomes

$$\frac{\Delta R}{R} = -\frac{\pi R_{\square}}{16W(\hbar/e^2)}\frac{1}{\ln(T/T_c)}\frac{1}{\xi^2}\left[\frac{1}{\xi^2} + \left[\frac{2eH}{\hbar c}\right]^2\frac{W^2}{12}\right]^{-3/2} . \qquad \text{(B-9)}$$

References

Abraham, D., and R. Rosenbaum, Phys. Rev. B 27, 1413 (1983).

Abrahams, E., P. W. Anderson, D. C. Licciardello and T. V. Ramakrishnan, Phys. Rev. Lett. 42, 673 (1979).

Abrahams, E., P. W. Anderson, P. A. Lee and T. V. Ramakrishnan, Phys. Rev. B 24, 6783 (1981).

Abrikosov, A., and L. P. Gorkov, Zh. Eksp. Teor. Fiz. 42, 1088 (1962) [Sov. Phys. - JETP 15, 752 (1962)].

Aharonov, Y. and D. Bohm, Phys. Rev. 115, 485 (1959).

Altshuler, B. L., and A. G. Aronov, Zh. Eksp. Teor. Fiz. 75, 1610 (1978) [Sov. Phys. JETP 48, 812 (1978)].

Altshuler, B. L., and A. G. Aronov, Pis'ma Zh. Eksp. Teor. Fiz. 30, 514 (1979) [JETP Lett. 30, 482 (1979)].

Altshuler, B. L., and A. G. Aronov, Pis'ma Zh. Eksp. Teor. Fiz. 33, 515 (1981a) [JETP Lett. 33, 499 (1981a)].

Altshuler, B. L., and A. G. Aronov, Solid State Commun. 38, 11 (1981b).

Altshuler, B. L., and A. G. Aronov, in Electron-Electron Interactions in Disordered Systems, edited by A. L. Efros and M. Pollak (Elsevier, Amsterdam, 1985).

Altshuler, B. L., A. G. Aronov and P. A. Lee, Phys. Rev. Lett. 44, 1288 (1980).

Altshuler, B. L., A. G. Aronov and D. E. Khmelnitskii, Sol. State Comm. 39, 619 (1981a).

Altshuler, B. L., A. G. Aronov, A. I. Larkin and D. E. Khmelnitskii, Zh. Eksp. Teor. Fiz. 81, 768 (1981b) [Sov. Phys. JETP 54, 411 (1981b).

Altshuler, B. L., A. G. Aronov and B. Z. Spivak, Pis'ma Zh. Eksp. Teor. Fiz. 33, 101 (1981c); Sov. Phys. JETP Lett. 33, 94 (1981c).

Altshuler, B. L., A. G. Aronov, D. E. Khmelnitskii and A. I. Larkin, in Quantum Theory of Solids, Chap. 3, edited by I. M. Lifshitz (Mir, Moscow, 1982a).

Altshuler, B. L., A. G. Aronov and D. E. Khmelnitskii, J. Phys. C 15, 7367 (1982b).

Anderson, P. W., Phys. Rev. 109, 1492 (1958).

Anderson, P. W., D. J. Thouless, E. Abrahams and D. E. Fisher, Phys. Rev. B 22,

3519 (1980).

Ashcroft, N. W., and N. D. Mermin, Solid State Physics, (Holt, Rinehart and Winston, New York, 1976).

Aslamazov, L. G., and A. I. Larkin, Fiz. Tverdogo Tela 10, 1104 (1968) [Soviet Physics - Solid State 10, 875 (1968).

Bassous, E., R. Feder, E. Spiller and J. Topalian, Solid State Technol. 19, 55 (1976).

Beaumont, S. P., P. G. Bower, T. Tamamura and C. D. W. Wilkinson, Appl. Phys. Lett. 38, 436 (1981).

Beaumont, S. P., G. Bower, B. Singh, T. Tamamura and C. D. W. Wilkinson, Microcircuit Engineering 81, A. Oosenbrug, editor (Swiss Federal Institute of Technology, Lausanne, Switzerland, 1981).

Bergmann, G., Z. Phys. 225, 430 (1969).

Bergmann, G., Phys. Rev. B 3, 3797 (1971).

Bergmann, G., Z. Phys. 48, 5 (1982).

Bergmann, G., Phys. Rev. B 28, 2914 (1983).

Bergmann, G., Phys. Rep. 107, 1 (1984).

Bergmann, G., Phys. Rev. Lett. 57, 1460 (1986).

Bethe, H. A., and E. E. Salpeter, Quantum Mechanics of One- and Two-Electron Atoms (Springer-Verlag, Berlin, 1957).

Binnig, G., and H. Rhorer, Helv. Phys. Acta 55, 726 (1982).

Bishop, D. J., G. J. Dolan, Phys. Rev. Lett. 55, 2911 (1986).

Black, J. L., B. L. Gyorffy and J. Jackle, Philos. Mag. B 40, 331 (1979).

Blonder, G. Bull. Am. Phys. Soc. 29, 535 (1984).

Brenig, W., M. -C. Chang, E. Abrahams and P. Wolfle, Phys. Rev. B 31, 7001 (1985).

Brodie, I., and J. J. Muray, The Physics of Microfabrication, (Plenum Press, New York, 1982).

Buttiker, M., Y. Imry, R. Landauer and S. Pinhas, Phys. Rev. B 31, 6207 (1985).

Caeci, M. S., and W. P. Cacheris, BYTE Magazine, Vol. 9, No. 5, p. 341 (1984).

Chandrasekhar, V., M. J. Rooks, S. Wind and D. E. Prober, Phys. Rev. Lett. 55, 1610, (1985).

Chandrasekhar, V., and D. E. Prober, Bull. Am. Phys. Soc. 32, 767 (1987).

Chang, T. H. P., J. Vac. Sci. Technol. 15, 1271 (1975).

Chaudhari, P., and H. -U. Habermeier, Phys. Rev. Lett. 44, 40 (1980).

Choi, K. K., D. C. Tsui and K. Alavi, Bull. Am. Phys. Soc. 31, 606 (1986), and to be published.

Dalrymple, B. J., Ph.D. Thesis, Yale University, 1983.

Dana, S. S., and J. R. Maldonado, J. Vac. Sci. Technol. B 4, 235 (1986).

Doezema, R. E., and J. F. Koch, Phys. Kondens. Mater. 19, 17 (1975).

Doezema, R. E., and T. Wegehaupt, Sol. St. Commun. 17, 631 (1975).

Face, D. W., Ph.D. Thesis, Yale University (1987).

Fawcett, E., in Fermi Surfaces, edited by W. Harrison and M. B. Webb (Wiley, New York, 1960).

Feuer, M. D., and D. E. Prober, IEEE Trans. on Electron Devices ED-28,1375 (1981).

Flanders, D. C., Ph.D. Thesis, MIT (1978). Reprinted as MIT Lincoln Laboratory Tech. Rep. No. 533 (1978).

Flanders, D. C., Microcircuit Engineering 81, A. Oosenbrug, editor (Swiss Federal Institute of Technology, Lausanne, Switzerland, 1981).

Flanders, D. C., and H. I. Smith, J. Vac. Sci. Technol. 15, 995 (1978).

Forgan, E. M., Cryogenics 14, 207 (1974).

Fukuyama, H., J. Phys. Soc. Jpn. 53, 3299 (1984).

Gasparov, V. A., and M. H. Hartunian, Sol. St. Commun. 19, 189 (1976).

Gefen, Y., Y. Imry and M. Ya. Azbel, Phys. Rev. Lett. 52, 129 (1984).

Gershenzon, M. E., V. N. Gubankov and Yu. E. Zhuravlev, Pis'ma Zh. Eksp. Teor. Fiz. 35, 467 (1982) [Sov. Phys. JETP Lett. 35, 576 (1982)].

Giordano, N., Phys. Rev. B 22, 5635 (1980).

Giordano, N., W. Gilson and D. E. Prober, Phys. Rev. Lett., 43, 725 (1979).

Goldstein, J. I., D. E. Newbury, P. Echlin, D. C. Joy, C. Fiori and E. Lifshin, Scanning Electron Microscopy and X-Ray Microanalysis (Plenum, New York,

1981).

Gordon, J. M., Phys. Rev. B 30, 6770 (1984).

Gordon, J. M., and A. M. Goldman, Phys. Rev. B 35, 4909 (1987).

Gordon, J. M., and J. Bindslev-Hansen, Phys. Rev. B 32, 6039 (1985).

Gor'kov, L. P., A. I. Larkin and D. E. Khmelnitskii, Pis'ma Zh. Eksp. Teor. Fiz. 30, 248 (1979) [Sov. Phys. JETP Lett. 30, 228 (1979)].

Greeneich, J. S., IEEE Trans. Electron Devices ED-22, 434 (1975).

Grobman, W. D., 1980 IEDM Technical Digest, pg. 415. IEEE Publ. 80 CH1616-2 (1980).

Hawryluk, A. M., Ph.D. Thesis, MIT (1981).

Heiblum, M., D. C. Thomas, C. M. Knoedler and M. I. Nathan, Appl. Phys. Lett. 47, 1105 (1985).

Henke, B. L., and E. S. Ebisu, in Advances in X-ray Analysis, Vol. 17, p. 150, (Plenum Press, New York, 1974).

Hikami, S., A. I Larkin and Y. Nagaoka, Prog. Theor. Phys. 63, 707 (1980).

Howard, R. E., and D. E. Prober, "Nanometer Scale Fabrication Techniques", in VLSI Electronics: Microstructure Science, vol. 5, (Academic Press, New York, 1982).

Ishibashi, K., K. Gamo, S. Namba, S. Ishida and K. Murase, Sol. St. Commun. 58, 743 (1986).

Jensen, H. H., H. Smith and J. W. Wilkins, Phys. Rev. 185, 323 (1969).

Kaplan, S. B., J. Low Temp. Phys. 37, 343 (1979).

Kaplan, S. B., C. C. Chi, D. N. Langenberg, J. J. Chang, S. Jafarey and D. J. Scalapino, Phys. Rev. B 14, 4854 (1976).

Kaveh, M., and N. Wiser, Adv. in Phys. 33, 257 (1984).

Keck, B., and A. Schmid, J. Low Temp. Phys. 24, 611 (1976).

Keller, J., and V. Korenmann, Phys. Rev. B 5, 4367 (1972).

Khmelnitskii, D. E., Physica 126B, 235 (1984).

Kobayashi, S., in Localization, Interaction and Transport Phenomena in Impure Metals, edited by B. Kramer, G. Bergmann and Y. Bruynseraede (Springer-Verlag, Berlin, 1985).

Landauer, R., Philos. Mag. 21, 863 (1970).

Larkin, A. I., Pis'ma Zh. Eksp. Teor. Fiz. 31, 239 (1980) [JETP Lett. 31, 219 (1980).

Lawrence, W. E., and A. B. Meador, Phys. Rev. B 18, 1154 (1978).

Lee, P. A., and A. D. Stone, Phys. Rev. Lett. 55, 1622 (1985).

Licini, J. C., G. J. Dolan and D. J. Bishop, Phys. Rev. Lett. 54, 1585 (1985).

Lin, B. J., J. Vac. Sci. Technol. 12, 1317 (1975).

Lin, J. J., and N. Giordano, Phys. Rev. B 33, 1519 (1986).

Lopes dos Santos, J. M. B., Phys. Rev. B 28, 1189 (1983).

Lopes dos Santos, J. M. B., and E. Abrahams, Phys. Rev. B 31, 172 (1985).

Ma, T. P., Appl. Phys. Lett., 27, 615 (1975).

Mackie, S., and S. P. Beaumont, Solid State Technol. 28, No. 8, 117 (1985).

Maki, K., Prog. Theor. Phys. 39, 897 (1968).

Mankiewich, P. M., R. E. Howard, L. D. Jackel, W. J. Skocpol and D. M. Tenant, J. Vac. Sci. Technol. B 4, 380 (1986).

McGinnes, W. C., and P. M. Chaikin, Phys. Rev. B 32, 6319 (1985).

Molzen, W. W., A. N. Broers, J. J. Cuomo, J. M. E. Harper and R. B. Laibowitz, J. Vac. Sci. Technol. 16, 269 (1979).

Morecroft, J. H., Electron Tubes and Their Application, (Wiley, New York, 1933).

Nagel, D. J., in: Advances in X-Ray Analysis, Vol. 18, p. 1, edited by W. L. Pickles, C. S. Barrett, J. B. Newkirk and C. O. Ruud (Plenum Press, New York, 1975).

Nelson, D. A. Jr., and A. L. Ruoff, J. Appl. Phys. 49, 5365 (1978).

Ono, T., and A. Ozawa, J. Vac. Sci. Technol. B 2, 68 (1984).

Overcash, D. R., B. A. Ratnam, M. J. Skove and E. P. Stillwell, Phys. Rev. Lett. 44, 1348 (1980).

Patton, B. R., Phys. Rev. Lett. 27, 1273 (1971).

Prober, D. E., M. D. Feuer and N. Giordano, Appl. Phys. Lett., 37, 94 (1980).

Raffy, H., R. B. Laibowitz, P. Chaudhari and S. Maekawa, Phys. Rev. B 28, 6607 (1983).

Rammer, J., and A. Schmid, Phys. Rev. B 34, 1352 (1986).

Reif, F., Fundamentals of Statistical and Thermal Physics (McGraw Hill, New York, 1965).

Rooks, M. J., Ph.D. Thesis, Yale University (1987).

Rooks, M. J., S. Wind, P. L. McEuen and D. E. Prober, J. Vac. Sci. Technol. B 5, 318 (1987).

Sacharoff, A. C., R. M. Westervelt and J. Bevk, Phys. Rev. B 29, 1647 (1984).

Santhanam, P., Ph.D. Thesis, Yale University (1985).

Santhanam, P., private communication, 1986.

Santhanam, P., and D. E. Prober, Phys. Rev. B 29, 3733 (1984).

Santhanam, P., S. Wind and D. E. Prober, in Proceedings of the Seventeenth International Conference on Low Temperature Physics, Karlsruhe, Federal Republic of Germany, Part I, p. 495 (North Holland, Amsterdam, 1984a).

Santhanam, P., S. Wind and D. E. Prober, Phys. Rev. Lett. 53, 1179 (1984b).

Santhanam, P., S. Wind and D. E. Prober, in Localization, Interaction and Transport Phenomena in Impure Metals, edited by B. Kramer, G. Bergmann and Y. Bruynseraede (Springer-Verlag, Berlin, 1985).

Santhanam, P., S. Wind and D. E. Prober, Phys. Rev. B 35, 3188 (1987).

Shankar, R., Principles of Quantum Mechanics (Plenum, New York, 1980).

Schmid, A., Z. Phys. 259, 421 (1973).

Schmid, A., in Localization, Interaction and Transport Phenomena in Impure Metals, edited by B. Kramer, G. Bergmann and Y. Bruynseraede (Springer-Verlag, Berlin, 1985).

Shimkunis, A. R., Solid State Technol., 27, No. 9, 192 (1984).

Skocpol, W. J., in Proceedings of the Winter School on Physics and Fabrication of Microstructures, Les Houches, France, 24 March - 6 April, 1986, edited by M. J. Kelly and C. Weissbuch (Springer-Verlag, Berlin, 1986).

Skocpol, W. J., L. D. Jackel, E. L. Hu, R. E. Howard and L. A. Fetter, Phys. Rev. Lett. 49, 951 (1982).

Skocpol, W. J., L. D. Jackel, R. E. Howard, E. L. Hu and L. A. Fetter, Physica 117B & 118B, 667 (1983).

Skocpol, W. J., L. D. Jackel, R. E. Howard, P. M. Mankiewich, R. E. Berhringer, L. A. Fetter and D. M. Tennant, in Proceedings of the International Conference on Localization, Interaction and Transport Phenomena in Impure Metals, Suppl. (PTB, Braunschweig, 1984).

Skocpol, W. J., P. M. Mankiewich, R. E. Howard, L. D. Jackel, D. M. Tennant and A. D. Stone, Phys. Rev. Lett. 56, 2865 (1986).

Smith, H. I., D. L. Spears and S. E. Bernacki, J. Vac. Sci. Technol. 10, 913 (1973).

Spears, D. L., and H. I. Smith, Electron Lett. 8, 102 (1972).

Stone, A. D., Ph.D. Thesis, Massachussetts Insitute of Technology (1983).

Stone, A. D., Phys. Rev. Lett. 54, 2692 (1985).

Stone, A. D., and Y. Imry, Phys. Rev. Lett. 56, 189 (1986).

Takayama, H., Z. Phys. 263, 329 (1973).

Thompson, R. S., Phys. Rev. B 1, 327 (1970).

Thornton, T. J. M. Pepper, H. Ahmed, D. Andrews and G. J. Davies, Phys. Rev. Lett. 56, 1198 (1986).

Thouless, D. J., Phys. Rev. Lett. 39, 1167 (1977).

Tinkham, M., Introduction to Superconductivity (McGraw-Hill, New York, 1975).

Umbach, C. P., S. Washburn, R. B. Laibowitz and R. A. Webb, Phys. Rev. B 30, 4048 (1984).

Uren, M. J., R. A. Davies, M. Kaveh and M. J. Pepper, J. Phys. C 14, L395 (1981).

Usadel, K. D., Z. Phys. 227, 260 (1969).

van Haesendonk, C., M. Gijs and Y. Bruynsereade, in Localization, Interaction and Transport Phenomena, edited by B. Kramer, G. Bergmann and Y. Bruynseraede (Springer-Verlag, Berlin, 1985).

Vranken, J., C. van Haesendonck and Y. Bruynseraede, preprint (1986).

Webb, R. A., S. Washburn, C. P. Umbach and R. B. Laibowitz, Phys. Rev. Lett. 54, 2696 (1985).

Wegehaupt, T., and R. E. Doezema, Phys. Rev. B 18, 742 (1978).

Wheeler, R. G., K. K. Choi, A. Goel, R. Wisnieff and D. E. Prober, Phys. Rev. Lett. 49, 1674 (1982).

White, A. E., M. Tinkham, W. J. Skocpol and D. C. Flanders, Phys. Rev. Lett. 48,

1752 (1982).

Wilson, A. D., Solid State Technol., 29, No. 5, 249 (1986).

Wind, S., M. J. Rooks, V. Chandrasekhar and D. E. Prober, Phys. Rev. Lett. 57, 633 (1986).

Wiser, N., Contemp. Phys. 25, 211 (1984).

Wisnieff, R. L., Ph.D. Thesis, Yale University (1987).